BRNO UNIVERSITY OF TECHNOLOGY

VYSOKÉ UČENÍ TECHNICKÉ V BRNĚ

CENTRAL EUROPEAN INSTITUTE OF TECHNOLOGY BUT

STŘEDOEVROPSKÝ TECHNOLOGICKÝ INSTITUT VUT

ELECTRON MICROSCOPY AND SPECTROSCOPY IN PLASMONICS

ELEKTRONOVÁ MIKROSKOPIE A SPEKTROSKOPIE V PLAZMONICE

DOCTORAL THESIS
DIZERTAČNÍ PRÁCE

AUTHOR Ing. Michal Horák
AUTOR PRÁCE

SUPERVISOR prof. RNDr. Tomáš Šikola, CSc.
ŠKOLITEL

BRNO 2019

Abstract

This thesis deals with electron and ion beam techniques for fabrication and characterization of plasmonic nanostructures. Analytical electron microscopy focusing on applications in the field of plasmonics is discussed. The emphasis is given to electron energy loss spectroscopy (EELS) and cathodoluminescence. Further, fabrication of plasmonic samples for transmission electron microscopy is introduced while the aim is put at focused ion beam lithography and at sample preparation using chemically synthesized particles in water solution. The main research results are divided into four parts.

The first part covers a comparative study of plasmonic antennas fabricated by electron beam and focused ion beam lithography. While both techniques are suitable for the fabrication of plasmonic antennas, electron beam lithography shall be prioritized over focused ion beam lithography due to better quality of the resulting antennas and considerably stronger plasmonic response in EELS. Antennas fabricated by focused ion beam lithography have slightly dull edges, exhibit pronounced thickness fluctuation, and they are also strongly contaminated not only by organic contaminants, but also by residues of FIB milling including implanted milling ions and atoms of a titanium adhesion layer.

In the second part, Babinet's principle of complementarity for plasmonic nanostructures is investigated on a set of gold disc-shaped antennas and complementary apertures in a gold layer with various diameters. The complementarity is confirmed for fundamental plasmon properties such as resonance energies, but differences rising from the limited validity of Babinet's principle are found, for example, for the spatial distribution of the near-field of plasmon polaritons.

The third part summarizes a study of nanostructures with functional properties related to the local enhancement of electric and magnetic field. Bow-tie and diabolo plasmonic antennas, both in the form of particles and in the form of apertures, exhibit particularly strong local field enhancement. Our study identifies several modes of localized surface plasmons in these antennas and characterizes their properties including mode energy, near field electric and magnetic field distribution, and the qualitative distribution of charge nodes and current associated with electron gas oscillations. Next, we have studied mode energy tunability in near infrared and visible spectral regions and focused on Babinet's complementarity between direct and inverted antennas.

The last part is focused on silver amalgam, which is a novel and very prospective plasmonic material. By changing the size of silver amalgam nanostructures their plasmon resonance can be tuned from ultraviolet through the whole visible to infrared region. As silver amalgam is well investigated in the field of electrochemistry, silver amalgam nanoparticles opens a possibility to combine plasmonics and electrochemistry together.

Key words

Plasmonic antennas, localized surface plasmons, electron microscopy, EELS, cathodoluminescence, Babinet's principle.

HORÁK, Michal. *Electron microscopy and spectroscopy in plasmonics.* Brno, 2019. Available online: https://www.vutbr.cz/en/students/final-thesis/detail/122351. Doctoral thesis. Brno University of Technology, CEITEC BUT. Supervisor of the doctoral thesis prof. RNDr. Tomáš Šikola, CSc.

Abstrakt

Tato práce se zabývá mikroskopickými technikami využívajícími elektronový a iontový svazek pro přípravu a charakterizaci plazmonických nanostruktur. Analytická elektronová mikroskopie je představena se zaměřením na aplikace v oblasti plazmoniky. Důraz je kladen na spektroskopii energiových ztrát elektronů (EELS) a katodoluminiscenci. Dále je diskutována výroba plazmonických vzorků pro transmisní elektronovou mikroskopii, přičemž je kladen důraz na litografii iontovým svazkem a na přípravu vzorků za použití chemicky syntetizovaných částic ve vodném roztoku. Hlavní výzkumné výsledky práce jsou rozděleny do čtyř částí.

První část se věnuje komparativní studii plazmonických antén vyrobených elektronovou a iontovou litografií. Přestože obě techniky jsou vhodné pro výrobu plazmonických antén, elektronová litografie by měla být upřednostňována před iontovou litografií díky lepší kvalitě výsledných antén a jejich silnější plazmonické odezvě. Antény vyrobené iontovou litografií mají neostré okraje, vykazují výrazné kolísání tloušťky a jsou také silně kontaminovány nejen organickými kontaminanty, ale také rezidui po iontové litografii včetně implantovaných iontů z iontového svazku a atomů titanové adhezivní vrstvy.

Ve druhé části je zkoumán Babinetův princip komplementarity pro plazmonické nanostruktury na sérii zlatých diskových antén a komplementárních apertur ve zlaté vrstvě s různými průměry. Komplementarita je potvrzena pro základní plazmonické vlastnosti jako rezonanční energie, ale rozdíly způsobené omezenou platností Babinetova principu jsou patrné například pro prostorové rozložení blízkého pole plazmonových polaritonů.

Třetí část shrnuje studii nanostruktur s funkčními vlastnostmi souvisejícími s lokálním zesílením elektrického a magnetického pole. Obzvlášť silné lokální zesílení pole vykazují plazmonické antény tvaru bowtie a diabolo, a to jak ve formě částic, tak ve formě apertur. Naše studie umožnila identifikovat několik módů lokalizovaných povrchových plazmonů v těchto anténách a charakterizovat jejich vlastnosti včetně energie módu, rozložení elektrické a magnetické složky blízkého pole módu, a kvalitativní rozložení uzlů náboje a proudu souvisejících oscilací elektronového plynu. Dále jsme studovali laditelnost energií módů v blízké infračervené a viditelné spektrální oblasti a zaměřili jsme se na Babinetovskou komplementaritu mezi přímými a invertovanými anténami.

Poslední část je zaměřena na stříbrný amalgám, nový a velmi perspektivní plazmonický materiál. Změnou velikosti stříbrných amalgámových nanostruktur může být jejich plazmonová rezonance laděna od oblasti ultrafialového záření přes celou viditelnou až po infračervenou oblast. Jelikož stříbrný amalgám je dobře prozkoumán v oblasti elektrochemie, stříbrné amalgámové nanočástice otevírají možnost kombinovat plazmoniku a elektrochemii dohromady.

Klíčová slova

Plazmonické antény, lokalizované povrchové plazmony, elektronová mikroskopie, EELS, katodoluminiscence, Babinetův princip.

HORÁK, Michal. *Elektronová mikroskopie a spektroskopie v plazmonice.* Brno, 2019. Dostupné také z: https://www.vutbr.cz/studenti/zav-prace/detail/122351. Dizertační práce. Vysoké učení technické v Brně, Středoevropský technologický institut VUT. Vedoucí práce Tomáš Šikola.

Prohlašuji, že jsem dizertační práci *Elektronová mikroskopie a spektroskopie v plasmonice* vypracoval samostatně pod odborným vedením prof. RNDr. Tomáše Šikoly, CSc. a Mgr. Vlastimila Křápka, Ph.D. s použitím materiálů uvedených v seznamu literatury.

V Brně dne 10. 10. 2019

Ing. Michal Horák

Acknowledgement

The author kindly acknowledge prof. Tomáš Šikola for supervising this thesis and Vlastimil Křápek for co-supervising this thesis and fruitful scientific discussions. EELS measurements were arranged following helpful discussions with Anna Carlson (Thermo Fisher Scientific) and Ai Leen Koh (Stanford University). Cathodoluminescence investigations were performed with help of Michael-Stöger Pollach (USTEM TU Wien) and Aleš Paták (ISI CAS). Fabrication processes were consulted with Tomáš Šamořil and Lukáš Břínek. Simulations were discussed with Martin Hrtoň and Vlastimil Křápek. Service technician Lukáš Macek (Thermo Fisher Scientific) and operators of FEI microscopes at CEITEC Nano Research Infrastructure Jan Michalička and Ondřej Man are acknowledged for keeping microscopes in good conditions for experiments.

Part of the work was carried out with the support of CEITEC Nano Research Infrastructure (ID LM2015041, MEYS CR, 2016–2019), CEITEC Brno University of Technology. Cathodoluminescence investigation was done in the Laboratory of Electron Microscopy, Institute of Scientific Instruments of the Czech Academy of Sciences (LEM ISI CAS) and University service center for transmission electron microscopy, Vienna University of technology (USTEM TU Wien). Some steps during the sample preparation were performed in the laboratory of the Institute of Physical Engineering, Faculty of Mechanical Engineering, Brno University of Technology.

The research has been co-financed by Czech Science Foundation (the project no. 17-25799S) and Brno University of Technology (the projects no. FSI/STI-J-17-4623, FSI/STI-J-18-5225, and CEITEC VUT-J-19-5945).

The final acknowledgement goes to Czechoslovak Microscopy Society (CSMS) for financial support via travel scholarships to MCM in Rovinj (2017) and IMC in Sydney (2018), for honoring me by ThermoFisher Scientific and CSMS scholarship 2019, and for giving me the opportunity to present my research results as a poster at the annual CSMS conference Microscopy 2016 and as a talk at the annual CSMS conferences Microscopy 2017, 2018, and 2019.

Contents

1 Introduction

Interactions of electromagnetic field and free electrons in metals at the metal-dielectric interface are studied in the field of nanophotonics called plasmonics [1]. Plasmonics deals with the generation, manipulation, guiding and transportation of electromagnetic waves in metals based on the interaction between electromagnetic field and collective oscillations of free electrons in metals called plasmons. At the metal-dielectric interface surface plasmon polaritons (SPP) associated with the local electromagnetic field are formed. They were predicted by R. H. Ritchie [2] and experimentally verified by C. J. Powell and J. B. Swan [3] in 1950s and theoretically explained and characterized by A. Otto [4], A. A. Lucas and M. Šunjić [5], and E. Kröger [6, 7] 10 years later. In metallic nanostructures, collective oscillations of free electrons strongly couple to the electromagnetic field forming the excitations called localized surface plasmons (LSP) [8]. The clear mathematical foundation for LSP oscillations was established by G. Mie in 1908 [9]. The first characterization of LSP by electron energy loss spectroscopy was presented by P. Batson in 1982 [10].

A characteristic feature of LSP is a strong enhancement of electromagnetic field within the surrounding dielectric together with its confinement on the subwavelength scale, which can be utilized to control various optical processes in a wide spectral region even below the free space diffraction limit [11]. Significance of this feature is further increased by easy tunability of the optical properties of nanostructures via engineering their size, shape, or dielectric environment [12]. This design flexibility allows creating a large amount of optical functions. Therefore, plasmonic antennas have a wide field of applications [13, 14], for example, in optoelectronics [15], telecommunications [16], photonics [17], microscopy [18], spectroscopy [19], energy harvesting [20], sensing elements [21], and medicine [22]. New discoveries with high application potential are often connected to implementation of new concepts into the field of plasmonics, such as a plasmoelectric effect [23], plasmonic lasing [24], generalized laws of reflection [25], spin-orbit coupling [26], chirality [27], and the Babinet principle of complementarity, which describes the correspondence between optical response of apertures and their complementary particles [28, 29].

Metallic nanostructures supporting LSP resonances can be fabricated using different techniques, such as chemical synthesis [30], optical lithography [31], electron beam lithography [32, 33], focused ion beam milling [34, 35], or 3D nanoprinting [36, 37]. Such nanostructures are often called plasmonic antennas. In most cases, silver or gold is used. Nevertheless, a very prospective material in the ultraviolet and visible range is, for example, aluminum [38, 39, 40]. The quality of prepared plasmonic antennas influences the LSP resonances. These resonances might be affected and degraded by any deviation from an ideal dielectric environment and an ideal shape, for example, by adding an adhesion layer below the antenna [41, 42], by polycrystallinity of the antenna [43, 44], or by surface roughness of the antenna [45, 46].

LSP resonances in plasmonic antennas can be detected using many different techniques, for instance, by dark field optical microscopy [47, 48] or near field optical microscopy [49, 50]. Mapping of LSP resonances with high spatial and good energy resolution is necessary to understand their origin and properties. The best spatial, energy, and time resolution is achieved by electron beam spectroscopy [51, 52], which covers electron energy loss spectroscopy (EELS) [53, 54, 55], energy filtered transmission electron microscopy (EFTEM) [56], cathodoluminescence (CL) [57, 58], photoemission electron microscopy [59], photo-induced near-field electron microscopy [60], and electron energy gain spectroscopy [61]. However, electron beam spectroscopy in a transmission electron microscope requires placing the plasmonic antenna onto a very thin substrates like silicon nitride or silicon oxide membranes with the thickness below 50 nm. A very recent study introduces usage of a monolayer or a thin layer of hexagonal boron nitride [62].

Research in the field of plasmonics has a large tradition at the Insitute of Physical Engineering and CEITEC Brno University of Technology [63], mostly in the field of metasurfaces [64, 65], scanning near-field optical microscopy [66, 67, 68], quantitative phase imaging [64, 69], EELS [70, 71], fabrication [72, 73, 74, 75], and development of theory [76]. This work, focused on fabrication and characterization of plasmonics antennas by electron microscopy, freely follows previous investigations of plasmonic antennas by electron energy loss spectroscopy [70] and cathodoluminescence [77] and contributes to the publication of several manuscripts [71, 75, 78, 79, 80].

2 Aims of the Thesis

This Thesis has five main aims proposed in the Thesis topic [81] (i) to introduce analytical electron microscopy and its prospect for plasmonics and to give a brief overview of fabrication of plasmonic antennas for electron beam spectroscopy investigations concentrated on focused ion beam lithoghraphy, (ii) to investigate elementary gold plasmonic antennas with focus on Babinet's principle of complementarity, (iii) to study nanostructures with functional properties related to the local enhancement of electric and magnetic field, (iv) to explore the possibility of fabricating plasmonic antennas using any less frequently used material, and (v) to study coupled structures.

The first aim is to introduce electron beam spectroscopic techniques and discuss their application in the field of plasmonics. These techniques are introduced in Chapter 3. Interaction of an electron beam with a sample is summarized in Section 3.1. Basics of elastic scattering are discussed in Section 3.2. Transmission electron microscopy is introduced in Section 3.3. The emphasis is given to EELS (Section 3.4) and CL (Section 3.5), which are both directly accessible techniques for me at CEITEC Nano research infrastructure (EELS in a transmission electron microscope), at the Laboratory of Electron Microscopy of the Institute of Scientific Instruments of The Czech Academy of Sciences (LEM ISI CAS, CL in a scanning electron microscope), and at the University Service Center for Transmission Electron Microscopy at Vienna University of Technology (USTEM TU Wien, CL in a transmission electron microscope). Basics of material analysis by energy dispersive X-ray spectroscopy are introduced in Section 3.6. Chapter 4 introduces the electron beam spectroscopy and briefly the theory behind in the field of plasmonics starting with surface plasmon polaritons (SPP) at metal-dielectric interfaces (Section 4.1) followed by localized surface plasmons (LSP) in metallic nanoparticles (Section 4.2). The final part of Chapter 4, Section 4.3, reviews electron beam spectroscopy investigations in the field of plasmonics published in literature.

Chapter 5 gives an overview of different techniques for fabrication of plasmonic antennas and their characterization by electron beam spectroscopy. As I am not working in the field of electron beam lithography myself, the emphasis is given to sample preparation using chemically synthesized nanoparticles (Section 5.1) and plasmonic antennas fabrication by focused ion beam lithography (Section 5.2) where several practical tips for the fabrication process are presented. Section 5.3 deals with CL measurements of possible substrates for plasmonic antennas. Section 5.4 deals with a gold disc-shaped nanoparticle, the first measurement of LSP by EELS at CEITEC, and silver amalgam nanoparticle with silver satellite nanoparticles proving experimentally the energy resolution of our system. Section 5.5 introduces CL measurement of LSP resonances in a gold diabolo antenna. Section 5.6 discusses the material and the size dependency of LSP resonances in metallic nanospheres, which is necessary to have a good overview to design more advanced experiments. Section 5.7 summarizes the study of gold sphere-like and triangular particles. The results measured on gold nanospheres and nanotriangles were published in Fine Mechanics and Optics [78].

Chapter 6 focuses on a comparative study of plasmonic antennas fabricated by electron beam and focused ion beam lithoghraphy published in Scientific Reports [75]. The choice of preferred fabrication technique is rather important. My results show that the plasmonic response of the antennas characterized by EELS is considerably stronger and slightly better localized for the antennas fabricated by electron beam lithography than for the antennas fabricated by focused ion beam lithoghraphy. Therefore, while both techniques are suitable for the fabrication of plasmonic antennas, electron beam lithography shall be prioritized over focused ion beam lithography due to better quality of the resulting antennas.

The second aim is to investigate elementary gold plasmonic antennas. Chapter 7 focuses on Babinet's principle of complementarity for gold disc-shaped plasmonic antennas. The emphasis is given on experimental study using spatially-resolved electron energy loss spectroscopy and cathodoluminescence to investigate electromagnetic response of elementary plasmonic antennas: gold discs and complementary disc-shaped apertures in a gold layer. The results were together with additional calculations covering their plasmonic response under the plane wave illumination published in Scientific Reports [71].

The third aim is to study nanostructures with functional properties related to the local enhancement of electric and magnetic field. Such plasmonic antennas were studied theoretically using a combination of two types of electric-magnetic complementarity to increase the degree of freedom for the design of the antennas: bow-tie and diabolo duality and Babinet's principle [82]. Plasmonic modes in nanoparticle dimers with conductive (diabolo or inverted bow-tie antennas) or insulating (bow-tie or inverted diabolo antennas) junction were revisited in our study combining EELS, optical spectroscopy, and numerical simulations, which will be published [80]. The results from this paper related to electron microscopy are summarized in Chapter 8 together with additional results related to plasmonic antennas of such a type.

The fourth aim is to explore the possibility to apply plasmonic structures of any less frequently used or nonstandard material. Chapter 9 deals with rather unique plasmonics on silver amalgam nanoparticles. It was experimentally proved that by changing the size of nanostructures the dipole LSP resonance can be tuned through the whole visible and infrared region. Therefore, nanostructured silver amalgam is proposed to be a prospective material for combination of electrochemistry and plasmonics. My results together with additional optical measurements were published in Journal of Physical Chemistry C [79].

The last aim proposed in the Thesis topic [81] is to study coupled structures. Plasmon coupling is observed between structures made of the same metal [83], structures made from different material [84], or between a plasmonic structure on an absorbing substrate, possibly exhibiting strong coupling of the plasmonic mode to the excitation in the substrate, for example, plasmon-phonon or plasmon-exciton coupling [85, 86]. Plasmon-exciton coupling has been recently studied by high resolution EELS in the visible region on silver nanoparticles supported by ZnO nanowires [87], on silver bow-tie antennas and quantum dots [88], on silver nanowires supported by hexagonal boron nitride [89], and on silver nanoparticles supported by tungsten disulfide [90]. Plasmon coupling between structures made of the same metal is studied in Chapter 8 where nanoparticle dimers with conductive or insulating junction are investigated. As the strong coupling phenomena with the substrate is observed by optical spectroscopy in infrared range [91], which is generally difficult to access by electron beam spectroscopy, the strong coupling phenomena is not discussed at all in this Thesis. For example, preliminary numerical simulations show that the splitting of the plasmon peak in gold antennas due to absorption in a silicon dioxide membrane is expected in the energy range between 0.1 eV and 0.2 eV while the splitting is around 30 meV. Nevertheless, the strong coupling phenomena with the substrate is one of possible topics for further research.

Beyond this Thesis, I have been during my PhD study active in the field of charged particle optics developing an accurate 3D interpolation method [92, 93] and calculating the deflecting properties of a charged particle diverter for the ATHENA mission [94], low energy EELS of semiconductors [95], high resolution imaging and EELS of graphene quantum dots [96], cathodoluminescence of semiconductors [97], and focused ion beam fabrication of holographic masks for electron vortex beam generation [98].

3 Analytical electron microscopy

Analytical electron microscopy is a powerful tool which offers a wide range of applications in imaging and spectroscopy. This chapter briefly introduces the theory for techniques used in the experiments in this Thesis. Section 3.1 summarizes the interaction of an electron beam with a sample. The following sections introduce elastic scattering (Section 3.2), transmission electron microscopy (Section 3.3), electron energy loss spectroscopy (Section 3.4), cathodoluminescence (Section 3.5), and basics of material analysis by energy dispersive X-ray spectroscopy (Section 3.6).

3.1 Electron beam – sample interaction

When an electron beam interacts with a sample, many different scattering and emission events may happen. Electrons from the primary electron beam may therefore produce different signals covering emitted electrons (secondary electrons and Auger electrons), backscattered electrons, emitted photons (X-rays and light), electron beam induced current, knocked-out ions, and in the case of a thin sample transmitted electrons (unscattered, elastically scattered, and inelastically scattered), which is illustrated in Figure 3.1.

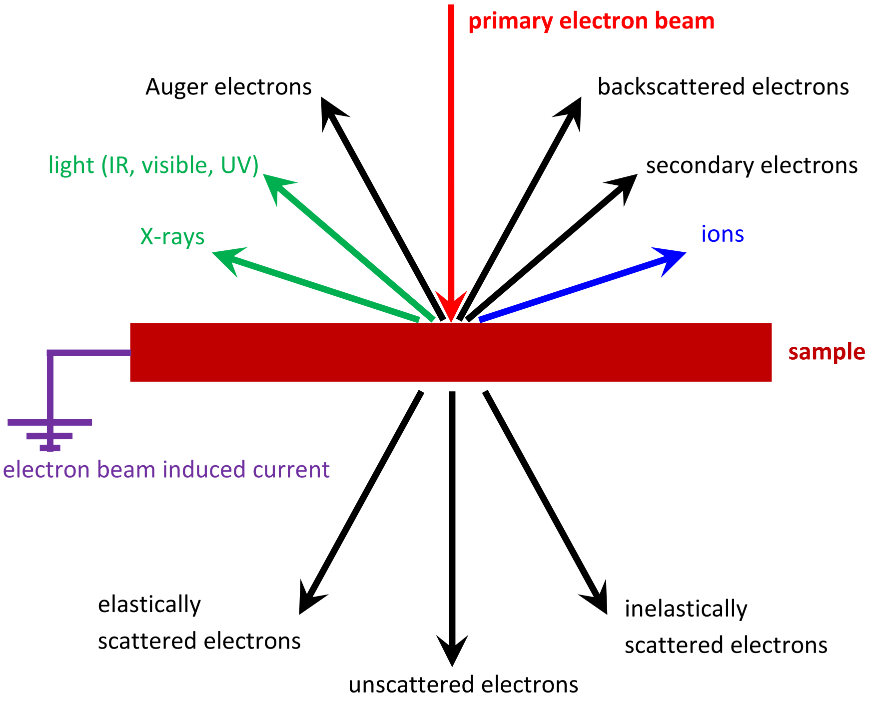

Figure 3.1: Interaction of an electron beam with a sample.

All of these signals might be used to record an image of the sample. Secondary and backscattered electrons are used for imaging in scanning electron microscopes (SEMs). Transmitted electrons are used for imaging in transmission electron microscopes (TEMs), where electrons scattered elastically creates the signal in a dark field image and electrons which are not scattered elastically creates the signal in a bright field image. Inelastically scattered electrons brings the information about excitation in the sample and allows to analyze optical and chemical properties by electron energy loss spectroscopy (EELS). Auger electrons studied by Auger electron spectroscopy (AES) brings the information about chemical composition of the sample. Similar information is contained in emitted photons: infrared, visible, and ultraviolet light detected by a cathodoluminescence (CL) and X-rays measured with energy dispersive X-ray spectroscopy (EDS). Finally, electron beam (and also ion beam) can modify or remove the material, which is used in electron beam lithography (EBL) and focused ion beam (FIB) lithography. As the result, electron microscopy including both SEMs and TEMs offers many different techniques with high application potential in the field of plasmonics. In the fabrication process, SEMs with lithographic tools and dual beam systems are widely used. High resolution imaging of plasmonic nanostructures is performed in the SEM or in the TEM. Basic chemical analysis is done by EDS. Advanced chemical analysis, thickness mapping, and measurement of all kinds of plasmon resonances is done by EELS. A monochromator is sometimes needed to achieve a sufficient energy resolution of TEM-EELS. Any excitation in the ultraviolet, visible, and near-infrared spectral range can be imaged by CL.

3.2 Elastic scattering

The fundamental principle in electron microscopy is electron scattering. The target is the sample consisting of atoms. These atoms can be either arranged randomly, or they can form a well ordered system – crystal lattice. If an electron in the electron beam and the target (the sample) have no change in their energy during the scattering event, the scattering is elastic. If the energy is transferred from the electron to the target, the scattering is inelastic. In such a case an electron loses some energy and creates an excitation in the sample, for example, a phonon or a plasmon.

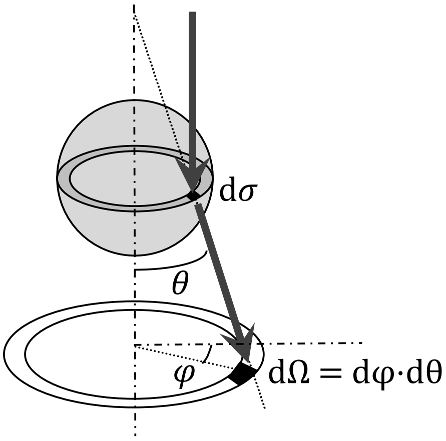

Figure 3.2: Geometric representation of the differential scattering cross section $\partial^2\sigma/\partial\Omega$.

The scattering event can be described mathematically using a quantity called the scattering cross section σ. Its differential, the differential scattering cross section $\partial^2\sigma/\partial\Omega = \partial^2\sigma/(\partial\varphi\partial\theta)$ describes the angular distribution of scattering from the target. As it is schematically shown in Figure 3.2, electrons are scattered through an angle θ into a solid angle $\mathrm{d}\Omega = \mathrm{d}\varphi\mathrm{d}\theta$. The average length λ_{MFP} which an electron travels between two scattering events is called the mean free path.

Number of scattering events N_{S} from N atoms into a given solid angle $\Delta\Omega$ can be expressed as

$$N_{\mathrm{S}}(\Omega) = I_{\mathrm{tot}} \frac{\partial^2\sigma}{\partial\Omega} \Delta\Omega \cdot N, \tag{3.1}$$

where I_{tot} denotes the total intensity (note that in microscopy community the term intensity has the meaning of the detected number of electrons by any detector), or considering intensity I_{S} detected on a detector with the area of $R^2\Delta\Omega$ as

$$N_{\mathrm{S}}(\Omega) = I_{\mathrm{S}}(\Omega) R^2 \Delta\Omega. \tag{3.2}$$

This allows to retrieve the differential scattering cross section experimentally as

$$\frac{\partial^2\sigma}{\partial\Omega} = \frac{I_{\mathrm{S}}(\Omega)}{I_{\mathrm{tot}}} \frac{R^2}{N}. \tag{3.3}$$

The scattering probability P to a certain solid angle Ω is expressed as

$$\frac{\partial^2 P}{\partial\Omega} = \frac{\partial^2\sigma}{\partial\Omega} \cdot n \cdot t, \tag{3.4}$$

where n is the density (i.e. the number of atoms per m^3), and t the thickness of the sample. Integrating Equation (3.4) we obtain

$$P = \sigma n t. \tag{3.5}$$

Equation (3.5) can be rewritten using the relation for the mean free path $\lambda_{\mathrm{MFP}} = 1/(\sigma n)$ as

$$P = \frac{t}{\lambda_{\mathrm{MFP}}}. \tag{3.6}$$

The scattering event follows the Poisson statistics, therefore the probability P_n of n-fold scattering can be expressed as

$$P_n = \left(\frac{t}{\lambda_{\mathrm{MFP}}}\right)^n \frac{\mathrm{e}^{-\frac{t}{\lambda_{\mathrm{MFP}}}}}{n!}. \tag{3.7}$$

The probability of no scattering is

$$P_0 = \mathrm{e}^{-\frac{t}{\lambda_{\mathrm{MFP}}}} = \frac{I_0(t)}{I_{\mathrm{tot}}}, \tag{3.8}$$

where $I_0(t)$ is the intensity of electrons unscattered by the sample with the thickness t, therefore the thickness t can be evaluated as

$$t = -\lambda_{\mathrm{MFP}} \ln \frac{I_0(t)}{I_{\mathrm{tot}}}. \tag{3.9}$$

This means, that the thickness t is proportional to the logarithm of the intensity of electrons unscattered by the sample $I_0(t)$ as in the case of homogeneous sample λ_{MFP} is constant and the total intensity I_{tot} depends just on the microscope settings and remains constant during the experiment, too. Therefore, the thickness can be determined via the intensity of electrons unscattered by the sample $I_0(t)$ (detected as the bright field signal in a STEM) or alternatively the intensity of electrons scattered by the sample $I_{\mathrm{tot}} - I_0(t)$ (detected as the dark field signal in a STEM).

The simplest case of electron scattering is scattering on a point like particle of charge Z corresponding to an atomic nucleus. Considering the quantum physics, the cross section is the modulus squared of the scattering amplitude $|f(\Omega)|^2$ and is related to the Fourier transform of the scattering potential V as

$$\frac{\partial^2\sigma}{\partial\Omega} = |f(\Omega)|^2 = \frac{m^2e^2}{4\pi^2\hbar^4}|\mathrm{FT}\left\{V\right\}|^2, \tag{3.10}$$

with m being the electron mass, e the elementary charge, and $\hbar$ the reduced Planck constant.

If we consider the Coulomb potential

$$V_{\mathrm{C}}(r) = -\frac{Ze}{4\pi\epsilon_0}\frac{1}{r} \tag{3.11}$$

and insert its Fourier transform

$$\mathrm{FT}\left\{V_{\mathrm{C}}(r)\right\} = -\frac{Ze}{4\pi\epsilon_0}\frac{4\pi}{q^2} \tag{3.12}$$

into Equation (3.10), we get

$$\frac{\partial^2\sigma}{\partial\Omega} = \frac{m^2e^2}{4\pi^2\hbar^4}\left(\frac{Ze}{4\pi\epsilon_0}\frac{4\pi}{q^2}\right)^2 = \frac{m^2e^4}{4\pi^2\hbar^4\epsilon_0^2}\frac{Z^2}{q^4} = \frac{4Z^2}{a_0^2}\frac{1}{q^4}, \tag{3.13}$$

where $a_0 = \frac{4\pi\epsilon_0\hbar^2}{me^2}$ is the Bohr radius, ϵ_0 the vacuum permittivity, and q the momentum transfer between the electron and the target [99, 100].

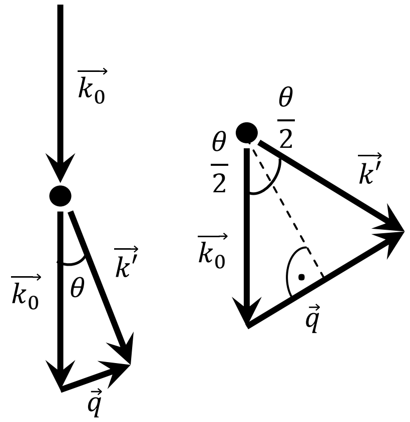

Figure 3.3: Schematic sketch of a scattering geometry with a momentum transfer $\vec{q}$ from the sample to a fast electron. As we consider the scattering as elastic, $k_0 = k'$. The momentum transfer is $q = k_0 \sin\theta \approx k_0\theta$ for small θ (left) or $q = 2k_0\sin(\theta/2)$ for any θ (right).

Considering the scattering geometry with the momentum transfer $\vec{q}$ (Figure 3.3) we get $q = 2k_0\sin(\theta/2)$, so Equation (3.13) can be expressed as

$$\frac{\partial^2\sigma}{\partial\Omega} = \frac{4Z^2}{a_0^2k_0^4}\frac{1}{16\sin^4(\theta/2)} = \frac{Z^2}{4a_0^2k_0^4}\frac{1}{\sin^4(\theta/2)} \approx \frac{4Z^2}{a_0^2k_0^4}\frac{1}{\theta^4}. \tag{3.14}$$

Equation (3.14) corresponds to the Rutherford cross section [99, 100].

Using the screened Coulomb potential (the Yukawa potential)

$$V_{\mathrm{Y}}(r) = -\frac{Ze}{4\pi\epsilon_0}\frac{1}{r}\mathrm{e}^{-r/a_Z}, \tag{3.15}$$

where $a_Z = a_0 Z^{-1/3}$ is the screening length, we obtain the Wentzel scattering cross section

$$\frac{\partial^2\sigma}{\partial\Omega} = \frac{4Z^2a_Z^2}{a_0^2k_0^4}\frac{1}{(\theta^2+\theta_0^2)^2} = \frac{4Z^{4/3}}{k_0^4}\frac{1}{(\theta^2+\theta_0^2)^2} \tag{3.16}$$

with $\theta_0 = 1/(k_0 a_Z)$ being the characteristic scattering angle [99, 100].

A crystal is a periodic arrangement of atoms at positions $\vec{R}_i$, therefore the potential of a crystal can be expressed using the screened Coulomb potential convolved with the delta function describing the atomic positions as

$$V(\vec{r}) = \sum_i \delta^3(\vec{r}-\vec{R}_i) \star V_{\mathrm{Y}}(\vec{r}). \tag{3.17}$$

The Fourier transform of this potential is

$$\mathrm{FT}\left\{V(\vec{r})\right\} = \sum_i \delta^3(\vec{q}-\vec{G}_i)\mathrm{FT}\left\{V_{\mathrm{Y}}(\vec{r})\right\} \tag{3.18}$$

and we get the elastic cross section

$$\frac{\partial^2\sigma}{\partial\Omega} = \sum_i \delta^3(\vec{q}-\vec{G}_i)\frac{4Z^{4/3}}{k_0^4}\frac{1}{(\theta^2+\theta_0^2)^2}, \tag{3.19}$$

which is the Wentzel cross section distributed in the reciprocal space to singular peaks at $\vec{G}_i$ corresponding to Bragg diffraction maxima positions. For more detailed discussion about elastic cross sections I refer, for example, to Chapter 3 of the textbook by D. B. Williams and C. B. Carter [99] or to Section 3.1 of the book by R. F. Egerton [100] and references therein.

3.3 Transmission electron microscopy

Elastic scattering of electrons is the major source of contrast in the transmission electron microscope. It is operated either in a transmission mode (TEM), where the sample is illuminated by a parallel electron beam (plane wave illumination), or in a scanning mode (STEM), where the sample is illuminated by a focused electron beam scanned pixel by pixel (point-like convergent beam illumination).

In the case of TEM, we have three possibilities of imaging. The first option is to use all transmitted electrons to create the image. This is the simplest technique which can be used also for high resolution TEM as there is no restriction of transfer of high spatial frequencies which are necessary for atomic resolution. A little disadvantage of this technique is low contrast. Contrast might be enhanced by inserting an objective aperture to filter out all elastically scattered electrons and capture a bright field image. Another possibility is to insert the objective aperture to select electrons scattered elastically with a defined momentum transfer and capture a dark field image. An illustrative sketch of the transmission electron microscope in TEM mode is shown in Figure 3.4.

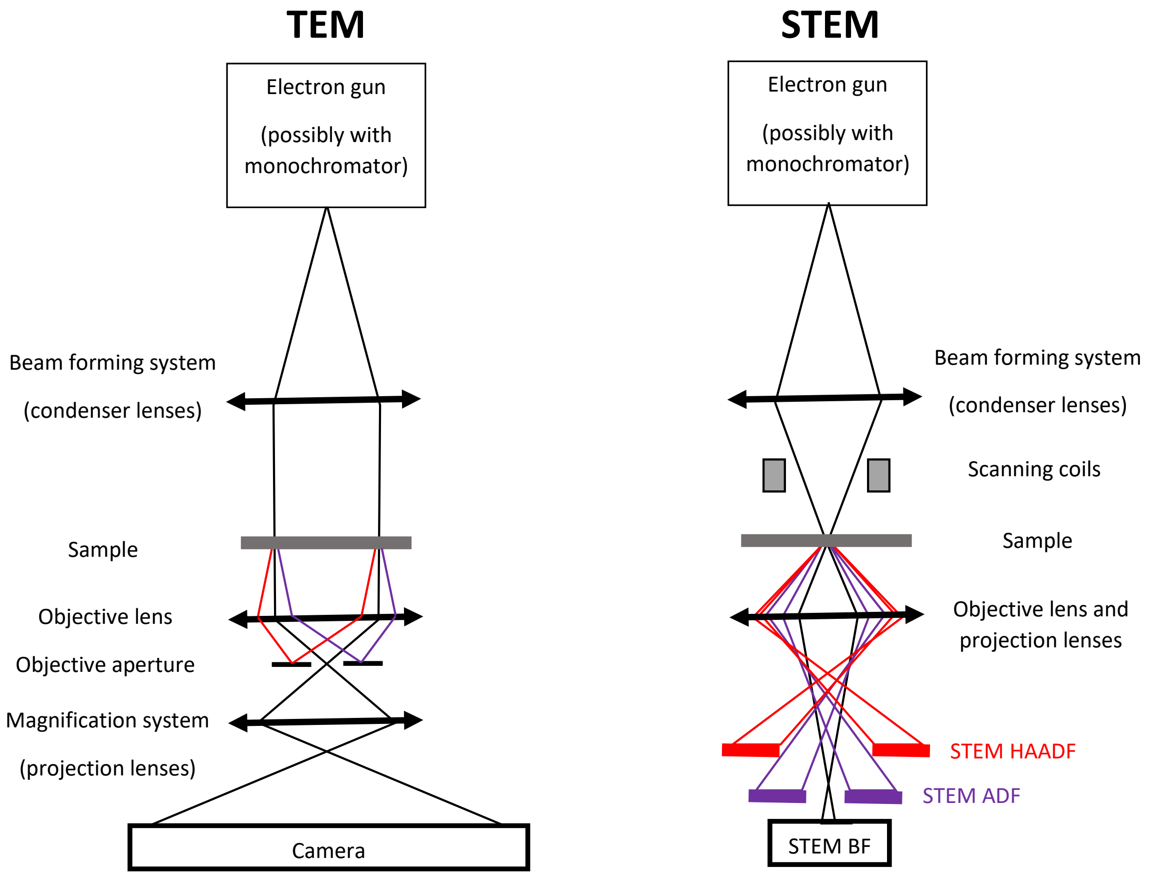

Figure 3.4: Schematic sketch of the transmission electron microscope in TEM and STEM mode. Electrons beam is created in an electron gun, formed by condenser lenses, and scattered by a sample. In the case of TEM, the sample is illuminated by a parallel beam. Elastically scattered electrons can be filtered out by the objective aperture and bright field image of the sample is magnified to a camera. In the case of STEM, the sample is illuminated point by point by a focused electron beam. Collection angles are defined by setting the projection lenses after the objective lens. Note that this schematic is simplified to get just the basic idea about TEM and STEM imaging.

In the case of STEM, we have usually several different STEM detectors. Bright field STEM detector collects transmitted electrons which were not scattered elastically (or the momentum transfer was small). An annular dark field (ADF) STEM detector collects transmitted electrons which are scattered elastically. High-angle annular dark field (HAADF) STEM detector collects transmitted electrons which are scattered elastically while the momentum transfer is large and the contrast is proportional to the atomic number Z. The contrast recorded with every STEM detector depends on the collection angle defined by the size and position of the STEM detector and settings of the projection system of the microscope defined by the parameter called the camera length. An illustrative sketch of the transmission electron microscope in STEM mode is shown in Figure 3.4.

Note that Figure 3.4 is simplified to get just the basic idea about TEM and STEM imaging. For more detailed discussion about TEM and STEM imaging I refer, for example, to Part 3 of the textbook by D. B. Williams and C. B. Carter [99] and references therein.

3.4 Inelastic scattering and electron energy loss spectroscopy

In electron energy loss spectroscopy (EELS), the distribution of energies lost by electrons transmitted through the sample is measured. The first EEL spectrum was measured by G. Leithäuser in 1904. He studied electrons (with the primary energy between 12 keV and 17 keV) transmitted through a 1 µm to 2 µm thick aluminum foil with a small pinhole, which were further dispersed in energy in a magnetic field [101]. EELS is used to characterize materials composition and properties in TEM since 1944 [102] and in SEM since 2016 [103]. Nowadays, EELS is a widely used technique and have many applications in both TEM [100] and SEM [104]. The EEL spectrum has two characteristic parts, the low loss part and the core loss part, which are rather different in the physical background.

In the low loss part, volume plasmons, surface plasmons, interband and intraband transitions, relativistic effects like Čerenkov radiation, localised surface plasmon modes, and even phonons might be detected. Thickness of the sample can be determined and the dielectric function can be retrieved utilizing Kramers-Kronig analysis [51, 100, 105, 106]. Plasmon spectroscopy of alloys allows to identify different phases by monitoring the shift of volume plasmon peak and fitting measured volume plasmon peak using standards [107]. We study the interaction between electron beam and valence electrons. All excitations in the low loss part have a collective behavior and are correctly described by the electrodynamic theory based on Maxwell equations.

In the core loss part, the absorption edges of elements are measured (not only the edge energy, but also the fine structure of the edge) and exact chemical composition and the density of unoccupied states can be determined [99, 100]. We study the interaction between electron beam and electrons from inner shells of atoms and the quantum mechanical approach to the theory of cross sections is ready to use.

Thickness measurement

Similarly to elastic scattering, the inelastic scattering follows the Poisson statistics, too. Consequently, the probability P_n of n-fold inelastic scattering can be expressed as

$$P_n = \left(\frac{t}{\lambda_{\mathrm{IMFP}}}\right)^n \frac{\mathrm{e}^{-\frac{t}{\lambda_{\mathrm{IMFP}}}}}{n!}, \tag{3.20}$$

where λ_{IMFP} is the inelastic mean free path. The probability of no inelastic scattering event is

$$P_0 = \mathrm{e}^{-\frac{t}{\lambda_{\mathrm{IMFP}}}} = \frac{I_{\mathrm{zlp}}}{I_{\mathrm{tot}}}, \tag{3.21}$$

where I_{zlp} is the intensity of electrons, which are not inelastically scattered by a sample with the thickness t and which did not lose any energy. Such electrons form the so-called zero-loss peak (ZLP) in the EEL spectrum at the zero loss energy. Consequently, the relative thickness $t/\lambda_{\mathrm{IMFP}}$ of the sample can be evaluated as

$$\frac{t}{\lambda_{\mathrm{IMFP}}} = \ln \frac{I_{\mathrm{tot}}}{I_{\mathrm{zlp}}}. \tag{3.22}$$

If the inelastic mean free path λ_{IMFP} is known, the absolute thickness t of the sample is determined as

$$t = \lambda_{\mathrm{IMFP}} \ln \frac{I_{\mathrm{tot}}}{I_{\mathrm{zlp}}}. \tag{3.23}$$

Both intensities I_{zlp} and I_{tot} can be easily measured. Therefore, the inelastic mean free path λ_{IMFP} is a relatively well investigated quantity, which can be either measured experimentally on the sample with known thickness, found in literature, or approximately calculated [100, 106].

Low loss EELS

The interaction of a transmitted electron with the sample can be described in terms of a dielectric response function $\epsilon(q, \omega)$. Additionally, the same response function describes the interaction between photons and a solid sample, therefore this formalism allows to compare EELS with optical measurements. R. H. Ritchie in 1950s derived an expression for the electron scattering power of an infinite medium [2]. The transmitted electron is represented as a point charge generating a spatially- and time-dependent electrostatic potential. Using the Fourier transforms, he found the transition probability per the unit path length in the medium. The most important result is that the loss probability $P_{\|}$ due to longitudinal modes corresponding to volume plasmon excitation is proportional to the imaginary part of the dielectric function ϵ as

$$\frac{\partial^3 P_{\|}}{\partial E \partial \Omega} = \frac{e^2}{\pi^2 \hbar^2 v^2} \frac{1}{\theta^2 + \theta_E^2} \Im \left\{ -\frac{1}{\epsilon} \right\}, \tag{3.24}$$

where v is the electron speed, $\theta_E = \frac{E}{2E_0}$ is the characteristic angle for a certain energy loss E (using a nonrelativistic approximation), E_0 is the energy of primary electron beam, and $\Im \left\{ -\frac{1}{\epsilon} \right\}$ is often called the loss function [100].

The Kramers–Kronig analysis (KKA) is important for a proper treatment of optical data. KKA directly follows the theory and equations introduced by R. H. Ritchie [2] for the electron scattering probability in an infinite medium. To apply KKA on measured EEL spectrum, we need to prepare the quantity $I_{\mathrm{SSD}}(E)$ called single volume scattering distribution. It means that surface losses are neglected and the recorded EEL spectrum is postprocessed by ZLP and multiple scattering deconvolution using the Fourier-log method. The single volume scattering distribution is expressed as [105, 108]

$$I_{\mathrm{SSD}}(E) = \frac{2\pi e^2 I_0 t}{\pi^2 \hbar^2 v^2} \Im \left\{ -\frac{1}{\epsilon} \right\} \ln \left(1 + \frac{\beta^2}{\theta_E^2} \right), \tag{3.25}$$

where I_0 is the incoming beam intensity, t the sample thickness, and β the collection semi-angle. The first part on the right side is the normalization factor dependent on the incoming intensity, the sample thickness, and electron speed v, which has to be determined before the Kramers–Kronig relations can be applied in order to obtain the optical properties. The second part is the loss function. The third part corresponds to the angular correction which has to be applied because of a non zero collection angle in the EELS experiment. For more details about the KKA I refer to Section 4.2 of the book by R. F. Egerton [100] and references therein or to manuscripts by M. Stöger-Pollach [105, 108].

R. H. Ritchie further described the transition probability for electrons passing through a thin foil [2]. The low loss EELS is well described by the Kröger theory [6, 7, 105]. For more details, see Appendix A.1 on page 120.

The loss probability can be expressed also in a different way as [51, 109]

$$\Gamma^{\mathrm{EELS}}(\vec{r_{\mathrm{e}}}(t), \omega) = \frac{e}{\pi \hbar \omega} \int \mathrm{d}t \Re \left\{ \mathrm{e}^{-i\omega t} \vec{v} \cdot \vec{E}_{\mathrm{el}}^{\mathrm{ind}}(\vec{r_{\mathrm{e}}}(t), \omega) \right\}, \tag{3.26}$$

where $\hbar\omega$ is the loss energy, $\vec{r_\mathrm{e}}(t)$ represents the electron trajectory, $\vec{v}$ is the electron velocity, and $\vec{E}_\mathrm{el}^\mathrm{ind}(\vec{r_\mathrm{e}}(t),\omega)$ denotes the induced parts of the electric field by the fast electron (for example, the field of LSP). It is calculated by removing the free-space solution of the electric field from the total computed electric field. Equation 3.26 is general and is used for localized surface plasmons, which will be discussed more in detail in Section 4.2.

Core loss EELS

The core loss part of the EEL spectrum comprises the absorption edges of the core electron levels specific to chemical elements – the material edges. In addition, there is a continuous plasmon-related background which approximately follows a power-law energy dependence and these edges are convoluted with the low loss part of the EEL spectra as the result of multiple scattering. The correct edge shape is therefore obtained applying the background subtraction and deconvolution of the low loss spectrum using the Fourier-ratio method [100]. There are, in principle, three main information coming from the core loss part of the EEL spectra. The presence of elemental edges allows a qualitative chemical analysis. The intensity of the edges allows a quantitative chemical analysis. And finally, the fine edge structure allows to study the chemical bonding and oxidation states of the elements. As the result, EELS offers a complete chemical analysis of the sample. The most important experimental parameters are the collection angle of the spectrometer β, which should be roughly corresponding to the characteristic angle θ_E, and the relative thickness of the sample, which should be in the interval $0.2 < t/\lambda_\mathrm{IMFP} < 0.7$. If the sample is thinner or the collection angle is smaller, the signal-to-noise ratio is getting worse. If the sample is thicker or the collection angle is larger, the signal-to-background ratio is getting worse.

The loss probability P, proportional to the inelastic scattering cross section σ, for an elemental edge can be expressed as

$$\frac{\partial^3 P}{\partial E \partial \Omega} = \frac{4\gamma^2}{a_0^2 q^4}\frac{k_\mathrm{f}}{k_\mathrm{i}} S(\vec{q}, E), \tag{3.27}$$

where $\gamma = 1/\sqrt{1 - v^2/c^2}$, k_i the initial wave number, k_f the final wave number, and $S(\vec{q}, E)$ the dynamic form factor

$$S(\vec{q}, E) = \sum_{\psi_\mathrm{f}} \left| \sum_{j=1}^{Z} \left\langle \psi_\mathrm{f} | \mathrm{e}^{i\vec{q}\cdot\vec{r_j}} | \psi_\mathrm{i} \right\rangle \right|^2 \delta(E_{\psi_\mathrm{i}} - E_{\psi_\mathrm{f}} + E), \tag{3.28}$$

which can be solved via the Schrödinger equation with ψ_i being the initial wave function with energy E_{ψ_i} and ψ_f the final wave function with energy E_{ψ_f}.

The quantitative chemical analysis by EELS is straightforward. The intensity of the elemental edge of element X at the energy interval $\mathrm{d}E$ with the collection angle β is

$$I_\mathrm{X}(\beta, \mathrm{d}E) = I_0 \sigma_\mathrm{X}(\beta, \mathrm{d}E) N_\mathrm{X} \mathrm{e}^{-t/\lambda_\mathrm{IMFP}}, \tag{3.29}$$

where N_X is the number of atoms of element X. Therefore, if the relative thickness of the sample t/λ_IMFP and the inelastic scattering cross section σ_X of element X is known, we can easily determine the number of atoms of element X as

$$N_\mathrm{X} = \frac{I_\mathrm{X}}{I_0 \sigma_\mathrm{X}} \mathrm{e}^{t/\lambda_\mathrm{IMFP}}. \tag{3.30}$$

The relative number of atoms for two elements X and Y can be determined without the knowledge of the thickness using the relation

$$\frac{N_\mathrm{X}}{N_\mathrm{Y}} = \frac{I_\mathrm{X}\sigma_\mathrm{Y}}{I_\mathrm{Y}\sigma_\mathrm{X}}. \tag{3.31}$$

For more details about the quantitative chemical analysis by EELS I refer to Section 4.5 of the book by R. F. Egerton [100] and references therein.

Energy filtered transmission electron microscopy

EELS allows to study optical, chemical, and physical properties of a specimen. A very high spatial (even atomic) resolution of the method can be achieved by two different approaches. The first approach is to use STEM, the scanning regime of a TEM, and scan point by point with a focused beam over the sample. This pixel by pixel acquisition can be in some cases time consuming. The second approach is to use energy filtered transmission electron microscopy (EFTEM) to record an energy filtered image created by electrons which have lost an exactly defined amount of energy.

Depending on the EEL spectral feature selected for imaging, images with the better image quality and/or distinct physical content can be generated. The two most widely used techniques in EFTEM are elastic imaging and elemental mapping. The elastic imaging enhances image resolution and contrast by extracting the zero-loss signal and eliminating the inelastic background, which can significantly improve the visibility of specimen structures. The elemental mapping, instead, invokes signals coming from element-specific inner-shell ionization edges, and is used to form two dimensional elemental distribution maps [99, 110]. Low-energy-loss EFTEM can be used, for example, for imaging nanoparticles [111] or as an alternative to STEM EELS for LSP mapping [112].

EELS spectrometers and image filters

EELS was established as a conventional spectroscopic technique in 1990s, when Gatan designed a post column filter [113, 114] allowing parallel spectroscopy (i.e. the whole energy interval of interest in an EEL spectrum is captured during one acquisition). The principle is simple. Electron beam is inelastically scattered by the sample and many electrons lose some energy. The polychromatic beam is dispersed with respect to the energy in a magnetic field generated by a magnetic prism. This magnetic prism creates two important planes – the plane with focused electron energy loss spectrum and the plane with focused image. In the case of spectroscopy (EELS), the electron energy loss spectrum is magnified by a multipole optics and captured on a CCD camera, as illustrated in Figure 3.5. In the case of imaging (EFTEM), the multipole optics is adjusted to image to the CCD an energy filtered image. The energy window is selected by inserting a slit into a plane where the electron energy loss spectrum is focused, as illustrated in Figure 3.6.

The resolution of EELS is determined by parameters of the TEM. Spatial resolution is limited by the probe size in the scanning regime, which can be below 1 nm. If the scanning regime is not used, the smallest area, from which the signal is collected, is approximately a circle with a diameter of 100 nm. Consequently, the scanning regime is crucial to achieve reasonable spatial resolution. Energy resolution depends on dispersion of the spectrometer and is limited by the energy dispersion of the primary electron beam. The energy dispersion is standardly evaluated as the full-width at half-maximum (FWHM)

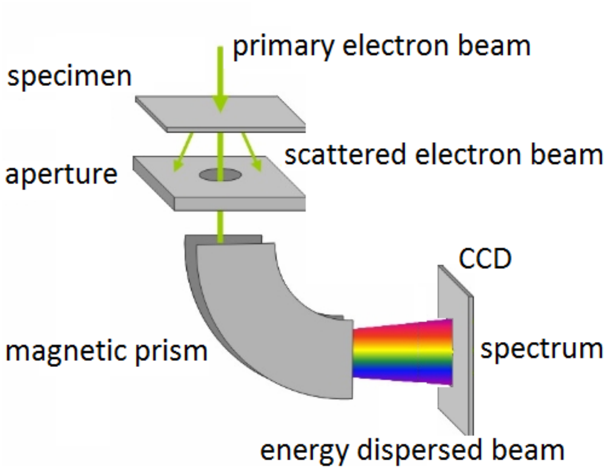

Figure 3.5: Principle of the image filter in the spectroscopy mode corresponding to electron energy loss spectroscopy (EELS).

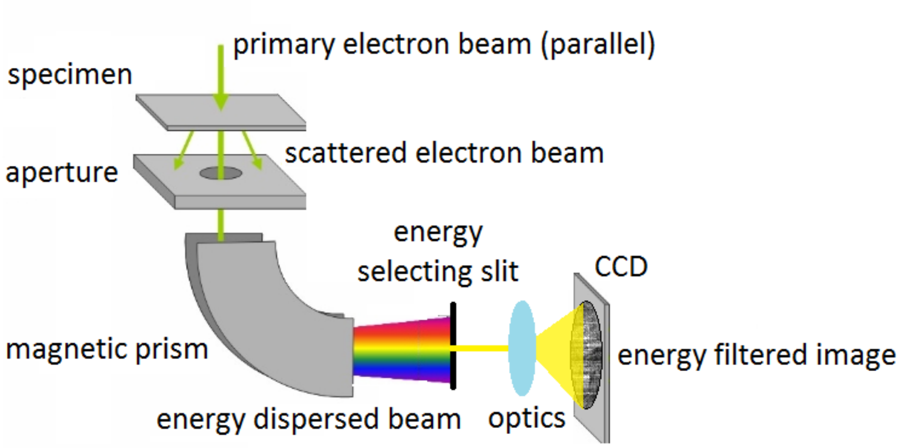

Figure 3.6: Principle of the image filter in the imaging mode corresponding to energy filtered transmission electron microscopy (EFTEM).

of the zero-loss peak (ZLP), which is usually around 1 eV for the microscope with a thermoemission gun, around 0.6 eV for the microscope with a Schottky gun, around 0.3 eV for the microscope with a cold field emission gun, and below 0.2 eV for the microscope equipped with a monochromator. The best spatial and energy resolution (FWHM ZLP 4.2 meV) has been achieved by the Nion microscope [115, 116], which is able to resolve phonons [117] and to perform atomic resolution spectroscopy [118].

In the case of EFTEM, the spatial resolution is determined by the microscope and can be in principle atomic. However, the energy resolution is determined by the energy selecting slit width and is typically around 1 eV. Both parameters are limited by the stability of the microscope during the acquisition and the spatial drift of the sample together with possible energy drift of the primary electron beam need to be considered.

However, the spatial resolution of EELS and EFTEM is further influenced by physical phenomenon called delocalization [119]. The delocalization means that the detected signal is not generated just in the exact point where the electron passes the sample, but can come from an area around. It is in range of units of nanometers for plasmons (energy losses around 10 eV) and in range of tens of nanometers for phonons (energy losses around

200 meV). In the case of higher energy losses, the delocalization is negligible. As a result, the EFTEM map recorded at a volume plasmon energy of the sample are much more blurred than the core loss map recorded at a certain elemantal edge. On the other hand, delocalization offers a possibility to measure easily the low loss spectra of beam-sensitive samples using aloof beam condition or leapfrog scanning [116, 119]. Aloof beam condition means that the focused electron beam is located next to the region of interest, typically in vacuum several nanometers far from the edge of the beam sensitive sample [120]. Leapfrog scanning is scanning with a very sharply focused electron beam with a large pixel size, for example, a subnanometer electron beam is used for spectrum image with a pixel size of 10 nm × 10 nm [119].

At CEITEC Nano, the TEM FEI Titan cubed equipped with a monochromator, an image corrector, and Gatan GIF Quantum spectrometer is available. The probe size (the spatial resolution of EELS) in the monochromated scanning regime is around 1 nm, because the probe corrector is not present. The monochromator is a double focusing Wien filter and achieves FWHM ZLP under 0.2 eV. For more details about monochromators see, for example, the review by K. Tsuno [121]. The GIF Quantum spectrometer [122] has the highest dispersion of 0.01 eV per pixel.

3.5 Cathodoluminescence

Luminescence is a common phenomenon in solids that results from a radiative transition in ions, molecules, or a crystal from an excited electronic state to a ground or other states with lower energy [123]. According to different lifetimes of luminescence emission, it can be differentiated between fluorescence (lifetime shorter than 10^{-8} s after excitation) and phosphorescence (lifetime longer than 10^{-8} s after excitation). Excitation can be provided, for example, by electrons (cathodoluminescence), photons (photoluminescence), or heat (thermoluminescence).

Cathodoluminescence (CL) is the emission of light as the result of electron bombardment. This phenomenon was observed in the middle of the 18th century during the experiments on electrical discharges in evacuated glass tubes, where luminescence appeared when electrons struck the glass. The observation of luminescence due to cathode-ray bombardment also led to discovery of the electron and determination of its charge-to-mass ratio by J. J. Thomson in 1897 [124]. Cathodoluminescence is most widely used in cathode-ray tube (CRT) based instruments, such as old oscilloscopes, televisions and computer monitors, and on fluorescent screens of transmission electron microscopes.

Cathodoluminescence analysis performed in an electron microscope can be divided into microscopy (luminescence images or maps of regions of interest) and spectroscopy (a spectrum corresponding to a selected area of the sample). Electron beam excitation in general leads to emission by all the luminescence mechanisms in contrast to photoluminescence, where the emission may strongly depend on the excitation (photon) energy. Cathodoluminescence provides high spatial resolution as the excitation by the electron beam is well localized, and ability to obtain depth-resolved information by varying the electron beam energy. However, the spatial resolution of CL is given by the interaction volume, which is determined not only by the probe size, but also by thickness and another properties of the material. The spectral resolution of CL is given by the spectrometer and is usually around 1 nm in wavelength. Therefore, CL combines the advantages from electron microscopy and optical spectroscopy: high spatial resolution (better than conventional optical spectroscopy) and high spectral resolution (better than EELS).

Photons are emitted as the result of any radiative transition in the sample. Mechanism of generating cathodoluminescence is usually classified into two categories as follows [58]: (i) Incoherent emission represented by radiative recombination between an electron and a hole in the energy bands bound at the energy gap, which is mediated by localized shallow states associated with impurity and exciton, a typical mechanism of the luminescence in semiconductors. This is widely used in geosciences, where the cathodoluminescence signal is connected to impurity states in oxides and minerals [125, 126, 127]. Another application of cathodoluminescence is covered by using phosphorus nanoparticles and nanodiamonds as biological luminescent markers [129, 130]. (ii) Coherent emission represented by light emission accompanied by movement of an electron such as transition radiation [128, 131], Čerenkov radiation [131, 132], Smith–Purcell radiation [133], and surface plasmon–mediated light emission [57, 58, 134, 135].

Incoherent cathodoluminescence

The theory of incoherent cathodoluminescence discussed in this section follows the theory summarized in [125], which is established mainly for application of SEM-CL instruments in mineralogy. The penetration depth of electrons and accordingly, the excitation depth from a crystal depends on the energy of electrons and is commonly in the range of 2–8 µm. However, energy transfer may occur in a crystal provided by the lattice, anion groups, or interaction of neighboring lattice defects, and then the emission site may be far away from the site of excitation. The CL intensity is, in general, proportional to the acceleration voltage and current density, but the power level used is limited by a destruction of the specimen or of specific defects including luminescence centers under electron bombardment [126]. These luminescent centers are defect centers in crystals, which can be related to pure lattice defects like vacancies or other electron-hole centers, or to incorporated impurities of foreign ions or atoms [123, 126, 127].

The emission of photons in luminescence processes is due to an electronic transition between an initial state with the energy E_i and the final state with the energy E_f. The energy, or the wavelength, of the emitted photon can be found from the relation

$$h\nu = \frac{hc}{\lambda} = E_\mathrm{f} - E_\mathrm{i}. \tag{3.32}$$

Luminescence emission spectra can be divided into intrinsic and extrinsic emission. In the case of electron transitions between the valence and conduction band (even modified by lattice imperfections), the energy reflects the band gap energy and the luminescence is called intrinsic, fundamental, or edge luminescence. If defects related to impurity atoms/ions (activators) are involved in the luminescence process it is called extrinsic, activated, or characteristic luminescence and the energy of the emitted luminescence can be related to the type of the impurity defect [126, 127]. Intrinsic luminescence, which appears at ambient temperatures as a near Gaussian-shaped band of energies with its intensity peak at a photon energy $h\nu \approx E_\mathrm{g}$, is due to recombination of electrons and holes across the fundamental band gap E_g (intrinsic property of the material). This edge emission band arising from conduction-band to valence-band transitions is produced by the inverse of the mechanism responsible for the fundamental absorption edge. In the case of an indirect-gap material, like Si or GaP, momentum must be conserved, therefore a phonon participation is required. The probability of such a process is significantly lower compared with the direct transitions, so the fundamental emission in indirect-gap semiconductors is relatively weak. The emission spectra (in both direct and indirect semiconductors), which depend on the presence of impurities, are extrinsic in nature, because the radiation due to impurities or defects can be much more intense than intrinsic CL at ambient temperatures even in direct-gap materials.

The generation factor G (i.e. the number of electron-hole pairs generated per incident beam electron) is given by

$$G = (1 - \gamma_{\mathrm{B}} - \gamma_{\mathrm{T}}) \frac{E_0}{E}, \tag{3.33}$$

where E_0 is the electron beam energy, E is the ionization energy (i.e. the energy required for the formation of an electron-hole pair), γ_{B} represents the fractional electron beam energy loss due to the backscattered electrons, and γ_{T} represents the fractional electron beam energy loss due to the transmitted electrons.

The local generation rate of carriers is

$$g(r, z) = \langle g \rangle G \frac{I_0}{e} = \langle g \rangle (1 - \gamma_{\mathrm{B}} - \gamma_{\mathrm{T}}) \frac{I_0 E_0}{eE} \tag{3.34}$$

where $\langle g \rangle$ is the normalized distribution of the ionization energy in the generation volume, I_0 is the electron beam current, and e is the electron charge [125].

Light is emitted from solids due to radiative recombination of excited states. Recombination centers are radiative or nonradiative, depending on whether the recombination leads to the emission of a photon or not. Examples of nonradiative recombination processes are multiple-phonon creation (direct conversion of the energy of an electron to heat), Auger effect (in which the energy of an electron transition is absorbed by another electron excited to a higher-energy state in the conduction band with subsequent creation of the electron from the semiconductor or dissipation of its energy through emission of phonons), and recombination due to surface states and defects. These centers are characterized by a rate of recombination $R \propto 1/\tau$, where τ is the recombination time. The carrier diffusion length L is related to the lifetime τ by $L = \sqrt{D\tau}$, where D is the diffusion coefficient. When competitive radiative and nonradiative centers are both present, the observable lifetime is given by

$$\frac{1}{\tau} = \frac{1}{\tau_{\mathrm{rr}}} + \frac{1}{\tau_{\mathrm{nr}}}, \tag{3.35}$$

where τ_{rr} and τ_{nr} are the radiative and nonradiative (including all nonradiative recombination processes) recombination lifetimes. The radiative recombination efficiency (or internal quantum efficiency) η is defined as

$$\eta = \frac{R_{\mathrm{rr}}}{R} = \frac{\tau}{\tau_{\mathrm{rr}}} = \frac{1}{1 + \tau_{\mathrm{rr}}/\tau_{\mathrm{nr}}}, \tag{3.36}$$

with R_{rr} as the radiative recombination rate. The rate of cathodoluminescence emission is proportional to η [125].

The cathodoluminescence intensity L_{CL} corresponding to the number of photons generated per second at the depth z is

$$L_{\mathrm{CL}} = f_{\mathrm{D}} f_{\mathrm{A}} f_{\mathrm{R}} \frac{G I_0}{e} \eta = f_{\mathrm{D}} f_{\mathrm{A}} f_{\mathrm{R}} (1 - \gamma_{\mathrm{B}} - \gamma_{\mathrm{T}}) \frac{I_0 E_0}{eE} \eta, \tag{3.37}$$

where f_{D} is a constant factor that accounts for such parameters of the CL detection system as the overall collection efficiency of the light collector, the photomultiplier (or solid-state detector) quantum efficiency, the transmissive efficiency of the monochromator, and the signal amplification factor, f_{A} and f_{R} are a factors accounting absorption and internal reflection losses, respectively [125].

Coherent cathodoluminescence signal

Coherent cathodoluminescence signal covers the transition radiation [128, 131], Čerenkov radiation [131, 132], Smith–Purcell radiation [133], and surface plasmon–mediated light emission [57, 58, 134, 135].

As long as the speed of the swift probe electron v does not exceed the speed of light inside the sample c/n, with c as the vacuum speed of light and n as the refractive index of the probed material, a particle uniformly moving in a homogeneous medium radiates no electromagnetic waves as the Čerenkov effect is not excited [95]. To initiate the transition radiation a heterogeneity must be created in the medium trough which the electron passes. The simplest case of such heterogeneity is a planar interface between two homogeneous materials. The theory for the photon emission at such infinite planar boundary (and two boundaries) was derived [136] and then thoroughly analyzed [97, 128, 131, 132]. In case of light, such an interface causes light reflection and refraction being well described by Fresnel. An analogous phenomenon, an electron passing through an infinite planar boundary with normal incidence from medium 1 to medium 2, was originally examined by V. L. Ginzburg and I. M. Frank in 1940s [97, 137]. For more details, see Appendix A.2 on page 121.

The cathodoluminescence intensity for a given electron trajectory $\vec{r_\mathrm{e}}(t)$ and energy $\hbar\omega$ can be expressed as [51, 109]

$$\Gamma^{\mathrm{CL}}(\vec{r_\mathrm{e}}(t),\omega) = \frac{c}{4\pi^2\hbar\omega}\int_{\Omega_\mathrm{D}} \mathrm{d}\Omega \left|\vec{f}^{\mathrm{ind}}_{\mathrm{el}}(\Omega,\omega)\right|^2, \tag{3.38}$$

where Ω_D is the detection solid angle of collected light and $\vec{f}^{\mathrm{ind}}_{\mathrm{el}}(\Omega,\omega)$ denotes the far-field amplitude produced by the fast electron (for example, the far-field amplitude of LSP). It is calculated by removing the free-space solution of the far-field amplitude from the total computed far-field amplitude. An application of Equation 3.38 for localized surface plasmons will be discussed more in detail in Section 4.2.

Cathodoluminescence spectrometers

Cathodoluminescence detectors are mounted into scanning electron microscopes (SEM), but also special CL sample holders for transmission electron microscopes (TEM) are available. Emitted photons are collected above or below the sample by a parabolic mirror and then transferred to the spectrometer by a set of mirrors or by optical fibers. Figure 3.7 shows a cathodoluminescence detector in a scanning electron microscope detecting the light emitted upwards, it means the backward emission with respect to the primary electron beam. An example of such commercial detector is Gatan Mono CL4 Plus installed on SEM FEI Magellan in Laboratory of Electron Microscopy, Institute of Scientific Instruments of the Czech Academy of Sciences (LEM ISI CAS) in Brno. Figure 3.8 shows a cathodoluminescence holder for transmission electron microscopy detecting the backward emission, the forward emission, or both the backward and the forward emission together. An example of such commercial detector is Gatan VULCAN installed on TEM FEI Tecnai at University service center for transmission electron microscopy, Vienna University of technology (USTEM TU Wien) in Vienna. More advanced spectrometers allows to measure the angular distribution of emitted light, too [58]. Collected light is dispersed in the spectrometer by a set of mirrors and a diffraction grating, and finally the spectrum is recorded on a CCD camera or photons are collected by a photomultiplier tube (PMT) as illustrated in Figure 3.9.

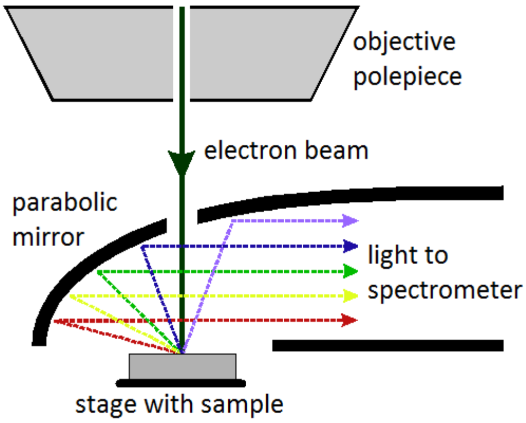

Figure 3.7: Schematic drawing of a cathodoluminescence detector in a scanning electron microscope detecting the light emitted in top direction, i.e. the backward emission with respect to the primary electron beam. This Figure was originally adopted from Reference [138] and further adjusted.

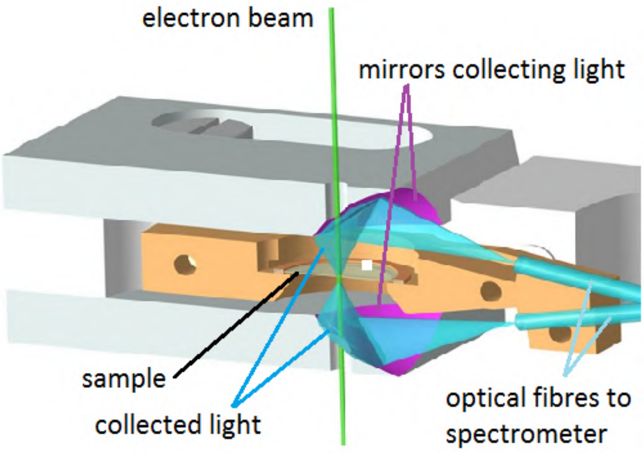

Figure 3.8: Cathodoluminescence holder for transmission electron microscopy detecting the light emitted in top direction, in bottom direction, or both mixed together. It means the backward emission, the forward emission, or both the backward and the forward emission mixed together. This Figure was originally adopted from Reference [139] and further adjusted.

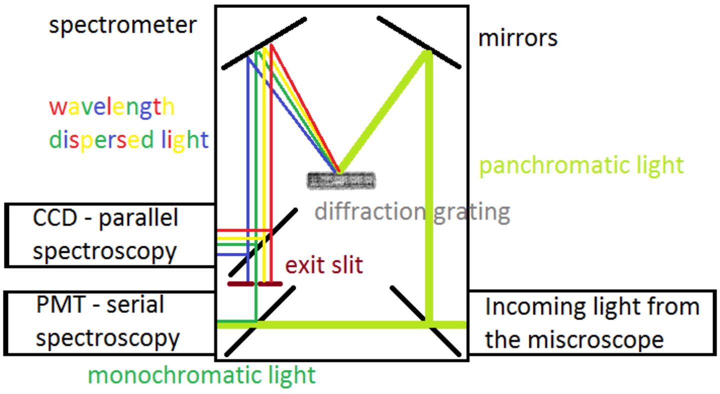

Figure 3.9: Schematic lay-out of a cathodoluminescence spectrometer: Collected light is dispersed by a diffraction grating and the spectrum is recorded by a CCD camera or wavelength-filtered photons are collected by a photomultiplier tube.

Cathodoluminescence microscopy generally offers three imaging possibilities: panchromatic imaging, monochromatic imaging, and true color imaging. The panchromatic CL image is obtained as the total intensity integrated over the whole recorded spectrum. The monochromatic CL image is obtained as the total intensity integrated over a selected spectral region of a recorded spectrum. Such a spectral region can be defined by inserting a color filter or a slit, or by numerical post-processing of a full spectrum image (if the whole CL spectrum is recorded in every pixel of the image). The true color CL image is the image where the color of every pixel is recalculated from the CL spectra recorded in this pixel.

3.6 Energy dispersive X-ray spectroscopy

Energy dispersive X-ray spectroscopy (EDS) deals with high energy photons (X-rays) emitted from the sample irradiated by the electron beam. There are two types of emitted X-rays [99]: (i) continuum bremsstrahlung X-rays created when electrons are slowed down by electrostatic interaction with the nucleus and (ii) characteristic X-ray radiation created when an atom excited by the electron beam returns to its ground state. Characteristic X-ray radiation creates the characteristic peaks in energy dispersed X-ray spectra which are unique to the ionized atom and therefore easily allow qualitative chemical analysis. In the case of a (S)TEM, where the energy of primary electron beam is high enough, the energy dispersed X-ray spectrum includes all common elements heavier than beryllium in one acquisition range as the typical acquisition range is 0.2 keV to 40 keV. Consequently, EDS allows to determine qualitative chemical composition of the sample very easily.

There are several disadvantages of this technique. The spectral resolution of EDS is rather poor, usually 135 eV, which might lead to overlap of some characteristic peaks, and the real energy dispersed X-ray spectrum includes several artifact peaks, too. First, internal fluorescence peak connected to the excitation of X-ray photon in the silicon detector which is afterwards detected (Si K_α X-ray energy is 1.74 keV). Second, escape peaks at the energy of the characteristic X-ray peak minus the energy of internal fluorescence peak (the characteristic X-ray photon excites first a Si K_α X-ray photon in the detector and is detected afterwards, therefore we detect the characteristic X-ray photon at the energy lower about 1.74 keV). Third, sum peaks created by two different X-ray photons coming to the detector at the same time and therefore detected as one X-ray photon with summed energy. Fourth, X-rays emitted by scattered electrons anywhere around the position of interest and secondary X-rays, such as X-rays from the grid, from the sample holder, and from the polepiece of the objective lens. To get the net intensity spectrum for a quantitative analysis, all these artifact peaks and the continuum bremsstrahlung background need to be removed.

If a thin sample is assumed, any absorption or fluorescence in the sample might be neglected. In such a case, the mass fractions of each element w_A and w_B can be related to net intensities of their characteristic peak I_A and I_B by the Cliff-Lorimer equation [99] as

$$\frac{w_\mathrm{A}}{w_\mathrm{B}} = k_\mathrm{AB}\frac{I_\mathrm{A}}{I_\mathrm{B}}, \tag{3.39}$$

where k_AB is the Cliff-Lorimer factor or k-factor, which is a sensitivity factor strongly dependent on the experimental conditions such as the beam energy and the detection solid angle. This equation can be easily extended to ternary and higher order systems by adding the equations [99]

$$\frac{w_\mathrm{B}}{w_\mathrm{C}} = k_\mathrm{BC}\frac{I_\mathrm{B}}{I_\mathrm{C}} \tag{3.40}$$

and

$$w_\mathrm{A} + w_\mathrm{B} + w_\mathrm{C} = 100\,\%, \tag{3.41}$$

while the k-factors for different pairs of elements are related to each other as

$$k_\mathrm{AB} = \frac{k_\mathrm{AC}}{k_\mathrm{BC}}. \tag{3.42}$$

A correct k-factor determination should involve taking many spectra from different parts of a thin foil standard for exactly defined experimental conditions. However, k-factors are usually calculated using different models taking into account atomic weight of elements, ionization cross sections, fluorescence yield, relative transition probability, and detector efficiency. This leads to a quick and easy evaluation of chemical composition, but the accuracy is rather disputable as k-factors calculated using different models differs in range of units of percents, but in some cases might differs up to 30 % (k-factors for Ag K_α X-rays with respect to Fe standard calculated using cross sections by Mott-Massey and Powell; adopted from Table 35.3A on page 651 in Reference [99]). For more detailed discussion about EDS quantification I refer to Chapter 35 in the textbook by D. B. Williams and C. B. Carter [99] and references therein.

EDS plays an important role in the field of plasmonics when qualitative or quantitative (as far as the highest accuracy is not essential) chemical composition is needed. In this Thesis, EDS was used for chemical analysis of gold disc shaped antennas fabricated by EBL and FIB discussed in Section 6 or for chemical analysis of silver amalgam nanoparticles discussed in Section 9.

4 Electron beam spectroscopy in the field of plasmonics

This Chapter briefly introduces plasmonics and, consequently, electron beam spectroscopy in the field of plasmonics. Plasmonics deals with surface plasmon polaritons (SPP), which are collective oscillations of free electrons connected to metal-dielectric interfaces associated with the local electromagnetic field which is strongly confined to the interface (Section 4.1). SPP do not exist only at infinite planar interfaces of metal and dielectric, but also at surfaces of small metallic structures (nanostructures or microstructures), where SPP are spatially confined to the structures and upon resonances form standing waves called localized surface plasmons (LSP) possessing highly enhanced near fields (Section 4.2). Such a localized field enhancement is responsible for an increased intensity of optical processes, higher sensitivity of spectroscopic methods and enables their better spatial resolution. A large number of optical properties can be easily tuned by the size, shape, and dielectric properties of structures and substrates [8]. The metallic structures supporting LSP are often called plasmonic antennas. For detailed introduction to plasmonics I refer to References [1, 8, 77, 140]. The last part of Chapter 4, Section 4.3, gives an overview of EELS and cathodoluminescence investigations of plasmonic antennas in literature.

4.1 Metal-dielectric interfaces

The interaction of a material with an electromagnetic field is described by the Maxwell equations

$$\nabla \cdot \vec{D} = \rho_{\mathrm{ext}}, \tag{4.1}$$

$$\nabla \cdot \vec{B} = 0, \tag{4.2}$$

$$\nabla \times \vec{E} = -\frac{\partial \vec{B}}{\partial t}, \tag{4.3}$$

$$\nabla \times \vec{H} = \vec{J}_{\mathrm{ext}} + \frac{\partial \vec{D}}{\partial t}, \tag{4.4}$$

which connect the macroscopic fields (electric field $\vec{E}$, electric displacement $\vec{D} = \epsilon_0 \vec{E} + \vec{P}$, vacuum permittivity ϵ_0, polarization density $\vec{P}$, magnetic field $\vec{H}$, magnetic induction $\vec{B} = \mu_0 \vec{H} + \vec{M}$, vacuum permeability μ_0, and magnetization $\vec{M}$) with an external charge density ρ_{ext} and current density $\vec{J}_{\mathrm{ext}}$.

The solution of the Maxwell equations at an infinite metal-dielectric interface is a transverse magnetic wave propagating along the interface. This wave represents the SPP and can be generated for the transverse magnetic (TM) mode. This mode has the transverse magnetic field $\vec{H}$ with the nonzero component H_y and the nonzero transverse and

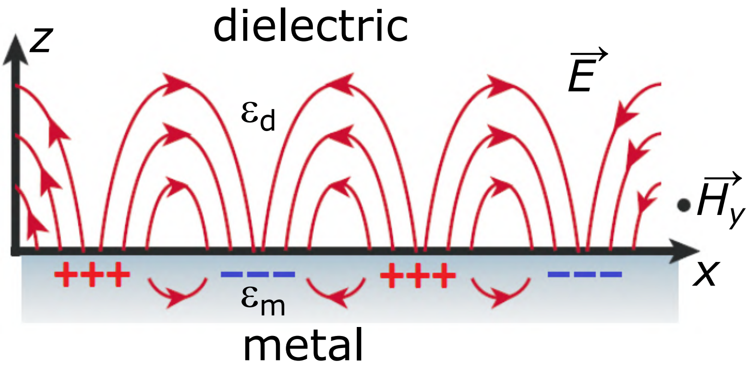

Figure 4.1: Illustration of the field components of a SPP propagating in x direction supported by a metal–dielectric interface. The transverse magnetic mode has the nonzero transverse magnetic component H_y. The nonzero transverse and longitudinal electric field E with components E_z perpendicular to the interface and E_x along the propagation direction is marked by the red arrows.

longitudinal electric field $\vec{E}$ with components E_z perpendicular to the interface and E_x along the propagation direction

$$\vec{H} = (0, H_y, 0) = (0, A, 0)\, \mathrm{e}^{ik_x x} \mathrm{e}^{-k_z^{d,m} z}, \tag{4.5}$$

$$\vec{E} = (E_x, 0, E_z) = \left(iAk_z^{d,m}, 0, -Ak_x\right) \frac{1}{\epsilon_0 \epsilon_r} \mathrm{e}^{ik_x x} \mathrm{e}^{-k_z^{d,m} z}, \tag{4.6}$$

where A is the amplitude defined by initial conditions, $\left(k_z^{d,m}\right)^2 = k_x^2 - \frac{\omega}{c}\epsilon_r$ while in dielectric (i.e., for $z > 0$) $\epsilon_r = \epsilon_d$ and in metal (i.e., for $z < 0$) $\epsilon_r = \epsilon_m$. Frequency of the wave ω is connected to the wave vector component k_x parallel to the interface along the propagation direction as

$$k_x = \frac{\omega}{c}\sqrt{\frac{\epsilon_\mathrm{m}\epsilon_\mathrm{d}}{\epsilon_\mathrm{m} + \epsilon_\mathrm{d}}}, \tag{4.7}$$

which is the well known dispersion relation of SPP. Their intensity exponentially decays in both the metal and dielectric with the increasing distance from the interface (Figure 4.1). For more details see, for example, References [4, 8, 77, 141].

4.2 Localized surface plasmons in metallic nanoparticles

In metallic nanostructures, SPP form localized resonances (standing waves) called localized surface plasmons (LSP). A schematic sketch of a LSP resonance is shown in Figure 4.2.

LSP modes in metallic nanoparticles can be classified into two groups: bright modes and dark modes (see Figure 4.3). The bright mode is a mode with a non zero electric dipole moment, which couples to a plane wave. It can be excited by light. On the other hand, the dark mode can be excited only by a highly localized field, for example, by a focused electron beam. Consequently, the dark mode cannot be generally excited by unstructured light. It is observed, for example, when an antenna with a gap (for example, a nanorod dimer with a small gap) is probed by a focused electron beam in the gap.

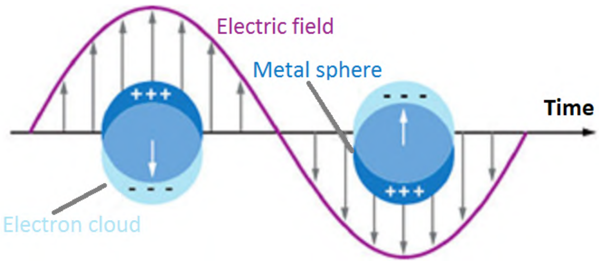

Figure 4.2: Free electrons in a metallic nanosphere are excited by an external electric field and oscillates in time forming the resonance called localized surface plasmons (LSP).

Figure 4.3: Two LSP modes in a nanorod dimer: bright (bonding) and dark (anti-bonding) mode. Position of an electron beam, by which the mode is excited, is marked by the green point. Red color corresponds to a positive charge, blue color to a negative charge.

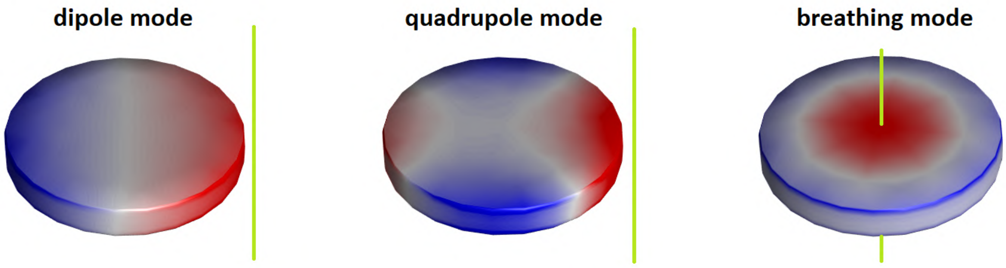

Figure 4.4: LSP modes in a nanodisc: the dipole, quadrupole, and breathing mode. Position of an electron beam, by which the mode is excited, is marked by the green line. Red color corresponds to positive charge, blue color to negative.

LSP modes in metallic nanoparticles can be classified also by their characteristic charge distribution as illustrated on a metallic nanodisc in Figure 4.4, where the charge distribution of the dipole, quadrupole, and breathing mode is shown. The dipole and the quadrupole is excited when the electron beam passes next to the disc. They differ in energy and their charge distribution has different rotational symmetry. At the circumference of the disc we see two maxima (one positive, one negative) and two minima in the case of the dipole mode. In the case of the quadrupole mode, we see four maxima (two positive, two negative) and four minima. The breathing mode is a radial monopole mode oscillating in the center of a nanoparticle analogous to acoustic vibrations, for example, in the middle of a disc. See also Reference [175], where a complete plasmonic spectrum of a silver disc is presented.

LSP resonances in rotationaly symmetric metallic nanoparticles have similar dispersion relation as SPP at large planar metal-dielectric interfaces. The wave vector is not arbitrary, but is connected to the size of the nanoparticle. Geometric interpretation of LSP dispersion relations in silver nanospheres is introduced in Reference [142]. They discuss mainly the dispersion relations where the wave vector is connected to different LSP modes and the dispersion curve follows different LSP modes in one nanoparticle. In a similar way, the wave vector is connected to the reciprocal value of the particle diameter and the dispersion curve follows the same LSP mode for nanoparticles with various diameters [143]; see also Figure 5.15 right.

G. Mie established an exact analytical description of the LSP resonances in submicrometer metallic nanoparticles [9, 144]. If the particle is much smaller than the wavelength λ of the incident light, just the dipole oscillation contributes to the absorption and scattering and so we can use a quasi-static approximation. Let us consider a nanosphere with the diameter d (much smaller than the wavelength λ) and dielectric function $\epsilon_\mathrm{s} = \epsilon_1 + i\epsilon_2$ in a dielectric medium with the dielectric function ϵ_d in a uniform electric field $\vec{E_0}$ in z direction. The electric field $\vec{E_0} = -\nabla\Phi$ fulfills the Laplace equation $\Delta\Phi = 0$. In the case of a nanosphere we use the spherical coordinates, hence

$$\frac{1}{r^2\sin\theta}\left[\sin\theta\frac{\partial}{\partial r}\left(r^2\frac{\partial}{\partial r}\right)+\frac{\partial}{\partial\theta}\left(\sin\theta\frac{\partial}{\partial\theta}\right)+\frac{1}{\sin\theta}\frac{\partial^2}{\partial\varphi^2}\right]\Phi(r,\theta,\varphi)=0, \tag{4.8}$$

which has a general solution in the form

$$\Phi_\mathrm{s}(r,\theta) = \sum_{l=0}^{\infty} A_l r^l P_l(\cos\theta), \tag{4.9}$$

$$\Phi_\mathrm{d}(r,\theta) = \sum_{l=0}^{\infty}\left(B_l r^l + C_l r^{-l-1}\right)P_l(\cos\theta), \tag{4.10}$$

where Φ_s and Φ_d is the electric potential inside and outside the sphere, respectively. Applying the boundary condition at $r = d/2$ we obtain

$$\Phi_\mathrm{s}(r,\theta) = -\frac{3\epsilon_\mathrm{d}}{\epsilon_\mathrm{s}+2\epsilon_\mathrm{d}}E_0 r\cos\theta, \tag{4.11}$$

$$\Phi_\mathrm{d}(r,\theta) = -E_0 r\cos\theta + \frac{\epsilon_\mathrm{s}-\epsilon_\mathrm{d}}{\epsilon_\mathrm{s}+2\epsilon_\mathrm{d}}E_0\frac{d^3}{8r^2}\cos\theta. \tag{4.12}$$

The electric field can be expressed as

$$\vec{E_\mathrm{s}} = \frac{3\epsilon_\mathrm{d}}{\epsilon_\mathrm{s}+2\epsilon_\mathrm{d}}\vec{E_0}, \tag{4.13}$$

$$\vec{E_\mathrm{d}} = \vec{E_0} + \frac{1}{4\pi\epsilon_0\epsilon_\mathrm{d}}\frac{3\vec{n}(\vec{n}\cdot\vec{p})-\vec{p}}{r^3}, \tag{4.14}$$

where $\vec{n} = \vec{r}/r$ is the unit vector in the direction of point of interest and $\vec{p}$ is the electric dipole moment induced in the sphere by the external field

$$\vec{p} = \frac{1}{2}\pi\epsilon_0\epsilon_\mathrm{d}d^3\frac{\epsilon_\mathrm{s}-\epsilon_\mathrm{d}}{\epsilon_\mathrm{s}+2\epsilon_\mathrm{d}}\vec{E_0}. \tag{4.15}$$

The scattering cross section of the sphere can be evaluated by dividing the total radiated power of the dipole P_rad by the intensity of the exciting wave I as

$$\sigma_\mathrm{sca}(\omega) = \frac{P_\mathrm{rad}}{I} = \frac{\frac{\omega^4}{12\pi\epsilon_0\epsilon_\mathrm{d}c^3}|\vec{p}|^2}{\frac{1}{2}c\epsilon_0\epsilon_\mathrm{d}E_0^2} = \frac{\pi}{24c^2}\omega^4 d^6\left|\frac{\epsilon_\mathrm{s}-\epsilon_\mathrm{d}}{\epsilon_\mathrm{s}+2\epsilon_\mathrm{d}}\right|^2. \tag{4.16}$$

The absorption cross section of the sphere can be evaluated by dividing the power P_abs dissipated by a point dipole by the intensity of the exciting wave I as

$$\sigma_\mathrm{abs}(\omega) = \frac{P_\mathrm{abs}}{I} = \frac{\frac{\omega}{2}\Im\left\{\vec{E_0}\cdot\vec{p}^\star\right\}}{\frac{1}{2}c\epsilon_0\epsilon_\mathrm{d}E_0^2} = \frac{\pi}{2c}\omega d^3\Im\left\{\frac{\epsilon_\mathrm{s}-\epsilon_\mathrm{d}}{\epsilon_\mathrm{s}+2\epsilon_\mathrm{d}}\right\}. \tag{4.17}$$

The sum of scattering and absorption is extinction, therefore the extinction cross section is

$$\sigma_{\text{ext}} = \sigma_{\text{sca}} + \sigma_{\text{abs}}. \tag{4.18}$$

When $\epsilon_1 + 2\epsilon_{\text{d}} = 0$, the absorption and scattering reaches a resonant maximum, corresponding to the dipole LSP resonance of the metallic sphere, see Equations (4.16) and (4.17). Generally, if we go beyond the quasi-static approximation, the energy of LSP resonances in spheres depends on their diameter and the dielectric properties of the sphere and the medium around.

Characterization of LSP by electron beam spectroscopy

Both EELS and CL performed in the scanning mode of (transmission) electron microscopes have become well established techniques in plasmonics and many of different plasmonic nanoparticles have been investigated by them as summarized in the following Section 4.3. However, EELS and CL do not deliver exactly the same signal. EELS detects all LSP modes, whereas CL measures exclusively LSP modes emitting light. The theory presented by A. Losquin and M. Kociak [109] says that the signal detected by EELS corresponds to the full electromagnetic local density of states projected onto the beam direction and is proportional to the extinction cross section, whereas the CL signal corresponds to the radiative electromagnetic local density of states and is proportional to the scattering cross section. It is advantageous to introduce the theory for measuring LSP resonances by EELS and CL that complements Equations (3.26) and (3.38) presented in Chapter 3.

Let us introduce the electric Green tensor $\overset{\leftrightarrow}{G}(\vec{r},\vec{r'},\omega)$ at points $\vec{r}$ and $\vec{r'}$ and frequency ω and its far-field asymptote $\overset{\leftrightarrow}{G}_{\infty}(\Omega,\vec{r'},\omega)$ depending on the direction Ω, source position $\vec{r'}$ and frequency ω. The quantities measured by EELS, loss probability $\Gamma^{\text{EELS}}(\vec{R},\omega)$, and CL, radiative probability $\Gamma^{\text{CL}}(\vec{R},\omega)$, can be expressed as [109]

$$\begin{aligned}
\Gamma^{\text{EELS}}(\vec{R},\omega) &= -\frac{4e^2}{\hbar}\Im\left\{\vec{e}_z\cdot\hat{\overset{\leftrightarrow}{G}}{}^{\text{ind}}(\vec{R},\vec{R},\omega/v,-\omega/v,\omega)\cdot\vec{e}_z\right\}, && (4.19)\\
\Gamma^{\text{CL}}(\vec{R},\omega) &= \frac{4\omega ce^2}{\hbar}\int_{\Omega_{\text{D}}}\mathrm{d}\Omega\vec{e}_z\cdot\left[\hat{\overset{\leftrightarrow}{G}}{}^{\text{ind}}_{\infty}(\Omega,\vec{R},\omega/v,\omega)\right]^{\text{T}}\times\\
&\quad\times\ \hat{\overset{\leftrightarrow}{G}}{}^{\text{ind}*}_{\infty}(\Omega,\vec{R},\omega/v,\omega)\cdot\vec{e}_z, && (4.20)
\end{aligned}$$

considering a fast electron traveling along the z axis at position $\vec{R} = x\vec{e_x} + y\vec{e_y}$. Therefore, the position of the electron is $\vec{r}_{\text{e}}(t) = \vec{R} + z(t)\vec{e}_z$. $\hat{\overset{\leftrightarrow}{G}}{}^{\text{ind}}(\vec{R},\vec{R},k_z,k'_z,\omega)$ denotes the Fourier transform of $\overset{\leftrightarrow}{G}{}^{\text{ind}}$ with respect to z and z', where $\overset{\leftrightarrow}{G}{}^{\text{ind}}$ presents the induced part of the Green tensor obtained from the Green tensor $\overset{\leftrightarrow}{G}$ by subtracting the free-space contribution. Similarly, $\hat{\overset{\leftrightarrow}{G}}{}^{\text{ind}}_{\infty}(\Omega,\vec{R},k_z,\omega)$ denotes the Fourier transform of $\overset{\leftrightarrow}{G}{}^{\text{ind}}_{\infty}$ with respect to z.

In BEM formalism, LSP modes of the plasmonic antenna can be defined through the electric fields $\vec{E}_k(\vec{r})$ obtained from a biorthogonal basis of geometric eigenmodes that only depend on the shape of the antenna. If we consider a plasmonic antenna surrounded by vacuum and the electron beam passing outside the antenna, then $\overset{\leftrightarrow}{G}{}^{\text{ind}}$ and $\overset{\leftrightarrow}{G}{}^{\text{ind}}_{\infty}$ reduces to surface terms [109, 145]

$$\begin{aligned} \overset{\leftrightarrow}{G}^{\text{ind}}(\vec{r},\vec{r'},\omega) &= -\frac{1}{4\pi\omega^2}\sum_k f_k(\omega)\vec{E}_k(\vec{r})\otimes\vec{E}_k^*(\vec{r'}), && (4.21)\\ \overset{\leftrightarrow}{G}^{\text{ind}}_{\infty}(\Omega,\vec{r'},\omega)\vec{e}_n &= -\frac{1}{4\pi c^2}\sum_k f_k(\omega)E_k^{n*}(\vec{r'})\vec{p}^{\,*}_{k\perp}(\Omega), && (4.22) \end{aligned}$$

where $\vec{p}^{\,*}_{k\perp}(\Omega)$ is the transverse component of the dipole moment $\vec{p}_k$ associated with the surface charge distribution of mode k, E_k^n is the projection of the electric field $\vec{E}_k$ of the mode k along the $\vec{e}_n$, and $f_k(\omega)$ is the spectral function characteristic of mode k

$$f_k(\omega) = \frac{\lambda_k + 1}{\lambda_k - \lambda(\omega)} \tag{4.23}$$

with λ_k as a real eigenvalue and

$$\lambda(\omega) = \frac{1+\epsilon(\omega)}{1-\epsilon(\omega)}. \tag{4.24}$$

EELS and CL then can be expressed as [109]

$$\begin{aligned} \Gamma^{\text{EELS}}(\vec{R},\omega) &= \frac{e^2}{\pi\hbar\omega^2}\sum_k \Im\left\{f_k(\omega)\right\}\left|\hat{E}_k^z\left(\vec{R},\frac{\omega}{v}\right)\right|^2, && (4.25)\\ \Gamma^{\text{CL}}(\vec{R},\omega) &= \frac{e^2\omega}{4\pi^2\hbar c^3}\left[\sum_k |f_k(\omega)|^2\int_{\Omega_\text{D}}\mathrm{d}\Omega\,|\vec{p}_{k\perp}(\Omega)|^2\left|\hat{E}_k^z\left(\vec{R},\frac{\omega}{v}\right)\right|^2 + \right. && (4.26)\\ &\left. + \quad 2\sum_k\sum_{l<k}\Re\left\{f_k(\omega)f_l^*(\omega)\right\}\int_{\Omega_\text{D}}\mathrm{d}\Omega\vec{p}_{k\perp}(\Omega)\cdot\vec{p}^{\,*}_{l\perp}(\Omega)\hat{E}_k^{z*}\left(\vec{R},\frac{\omega}{v}\right)\hat{E}_l^z\left(\vec{R},\frac{\omega}{v}\right)\right], \end{aligned}$$

where $\hat{E}_k^z$ is the projection along z of the Fourier transform along z of the electric field $\vec{E}_k$ of the mode k. To summarize the most important result, Equation (4.25) shows that EELS detects a sum of different LSP modes, whereas Equation (4.26) shows that CL detects a sum of different LSP modes together with some intermodal coupling corresponding to the second row of Equation (4.26). This intermodal coupling might make the interpretation of measured LSP modes by CL rather complicated. For more detailed discussion about the theory of EELS and CL measurements of LSP modes I refer to the manuscript by A. Losquin and M. Kociak [109], manuscript by G. Boudarham and M. Kociak [145], review paper by F. J. García de Abajo [51], and references therein.

Numerical simulations of LSP resonances

EEL and CL spectra of LSP resonances in plasmonic nanostructures can be calculated numerically. Simulations are important, especially when exact understanding of single modes in a structure with several modes is required. However, analytical solutions of scattering of electromagnetic waves are available only for metallic spheres or ellipsoids [9, 144]; therefore numerical simulations are necessary. Several numerical methods may be applied – the boundary element method (BEM), the finite-difference time-domain (FDTD) method, the finite element method (FEM), and the discrete dipole approximation (DDA). Comparison of some of these methods is summarized in References [146] and [147]. DDA calculation of EELS is introduced in Reference [148]. FEM simulation is often performed in the commercial software COMSOL Multiphysics [149]. In this work, BEM simulations using the software package MNPBEM [150, 151, 152] and some FDTD simulations by Lumerical FDTD solutions [153] are presented.

MNPBEM is a toolbox for the simulation of metallic nanoparticles, using a boundary element method approach developed by F. J. García de Abajo and A. Howie [154]. The main purpose of the toolbox is to solve Maxwell's equations for a dielectric environment, where bodies with homogeneous and isotropic dielectric functions are separated by abrupt interfaces. The approach is perfectly suitable for metallic nanoparticles with sizes ranging from a few to hundreds of nanometers, and for frequencies in the optical and near-infrared regime. Furthermore, the toolbox contains a Mie solver as a reference tool for spheres. Both EELS and CL simulations are possible in MNPBEM. However, it is somewhat tricky to include extended objects with open boundaries, such as substrates, adhesion layers, or TEM membranes.

The FDTD method is probably the most popular numerical simulation technique providing spectral responses in the electrodynamics and was firstly introduced by K. S. Yee [155]. In this algorithm, different components of the electromagnetic field are computed via solving Maxwell's equations by approximation of spatial and temporal derivatives by corresponding finite differences. A commercial FDTD solver Lumerical is designed primary to calculate the optical response for plane wave excitation, but it offers simulation of CL, too [156]. In contrast to MNPBEM, substrates are not problematic and a sphere on a membrane can be simulated easily. EELS simulation using Lumerical is possible, but rather complicated [147], therefore no EELS calculations have been performed in Lumerical in this work.

Experimental remarks

From the experimental point of view, the EELS measurement is straightforward. Electrons interacts inelastically with the sample and then they are detected in the spectrometer by a scintillator followed by a CCD camera. The only problematic part is correct background and zero-loss peak (ZLP) subtraction or a proper deconvolution. The spectral resolution depends on the spectrometer and the FWHM of the ZLP and on our system, TEM FEI Titan Themis Cubed with GIF Quantum at the CEITEC Nano Research Infrastructure, is better than 0.2 eV (see, for example, Figure 5.12).

In the case of CL, photons collected by mirrors are guided through optical fibers and processed by several mirrors and dispersed by a diffraction grating. The experimental setup has to be calibrated taking into account spectral dependence of absorption in optical fibers, reflectivity of mirrors, and CCD efficiency. Additionally, CL offers a possibility of polarization measurement and angle resolved measurement of the light emitted from plasmonic antennas which brings additional information about the emission. The spectral resolution depends on the spectrometer only. On both systems used in this work, TEM FEI Tecnai F20 with Gatan VULCAN at USTEM TU Wien and SEM FEI Magellan with Gatan MonoCL4 Plus at the LEM ISI CAS in Brno, it is better than 0.05 eV (see, for example, Figure 5.13).

EFTEM offers better spatial resolution than EELS but worse energy resolution [112]. It is quite a rare technique in plasmonics since a very accurate setting of the energy slit is necessary. For example, a plasmon map at the energy loss (1.4 ± 0.1) eV needs an energy slit of 0.2 eV width perfectly stable during the whole acquisition. In the case of an energy drift, much more intense beam of elastically scattered electrons might damage the camera. These are the main reasons why no EFTEM imaging of LSP was done in this work.

4.3 Overview of electron beam spectroscopy investigations in the field of plasmonics

As this work is mainly focused on electron energy loss spectroscopy (EELS) and cathodoluminescence (CL) of plasmonic antennas, it is useful to summarize the investigations in this field which are partially summarized in review papers [54, 55, 157]. Let us start from elementary shapes, like spheres and rods and their assemblies, proceeding to more complicated plasmonic antennas.

EELS investigations were performed on gold nanospheres, nanoellipsoids, and similar nanoparticles linked through DNA strands to a silicon nitride membrane [158], and on individual silver nanospheres with the radius between 3 and 30 nm [159]. In both cases, only the dipole mode was observed. For spheres encapsulated in silicon nitride, additional higher order surface plasmon resonances were observed for particles with the radius between 4 and 20 nm [160]. LSP resonances in clusters of aluminum nanospheres were studied by EELS in the year 1982, which is one of the pioneering measurements of EELS in plasmonics [10]. Furthermore, quantum tunnelling was studied by EELS between two [161] and three [162] silver nanospheres. Photon emission from silver particles induced by a high-energy electron beam was observed in the year 2000, which is one of the pioneering measurements of CL in plasmonics [57] followed by a complex CL investigation of gap and Mie plasmons in individual silver nanospheres [163]. Recently, 3D multipole rotation in silver nanospheres was theoretically described and measured by CL [164] and plasmonic quantum size effects in silver nanoparticles were investigated by EELS [165].

Surface plasmon modes of a single silver nanorod were mapped using energy filtered transmission electron microscopy [166], EELS [167], and CL [168]. In all cases, higher-order modes in a single rod are mapped. EELS study was performed on gold nanorods of different sizes with resonances in infrared region [169], and gold nanorods and nanocrosses [44]. Plasmonic modes in gold nanowires were observed using CL on a silicon substrate [134] and on a glass substrate covered with an indium-tin-oxide layer [129]. Plasmonic dark modes were studied on triangular system arrangements of gold nanorods [171]. They claimed that the dark modes do not couple to the far field and can arise from the plasmon hybridization in a set of interacting nanoparticles. Due to their lack of a net dipole moment, dark modes have longer lifetimes than bright modes. The strong confinement of energy in these modes and their associated near fields hold great promise for achieving strong coupling to single photon emitters [171]. Silver nanocrosses were presented as an easily tunable plasmonic system especially with tuning the higher order modes in a very controlled manner with the help of EELS [172]. Aluminum mostly rod-shaped antennas were characterized by both EELS and CL [173].

Gold discs with different diameters were studied by CL [77], but the observed CL spectra are very noisy. Panchromatic CL maps of silver discs were shown [174]. Modes of single Ag disks and their dimers were mapped by EELS [83]. Line scans through the structures shows a dipole and a breathing mode in the disc, and bonding (bright) and antibonding (dark) modes in the disc dimer. A complete plasmonic spectrum of a silver disc was investigated by EELS [175] and angle- and polarization-resolved CL [176]. Breathing modes in silver discs were investigated by both EELS and CL [177]. Results show, that the mode with the strongest coupling to the electron beam has radial symmetry with no net dipole moment, therefore it does not couple to light and cannot be observed by optical measurements. This radial breathing mode has the character of an extended two-dimensional surface plasmon with a wavenumber determined by the circular disk confinement. Its strong near fields can influence the hybridization in coupled plasmonic nanoparticles as well as coupling with nearby quantum emitters [175]. Additionally, the effect of metallic adhesion layers on EELS of LSP resonances in gold discs was discussed [41].

According to Babinet's principle of complementarity, circular holes in a metallic layer are apertures complementary to discs. Spectral, spatial, and angular CL response of individual nanoholes with the diameter ranging from 50 to 180 nm in the 80 nm thick gold layer on a silicon substrate is discussed in Reference [178]. Results show small changes in the resonant wavelength of the observed dipole mode. The maximal intensity of the mode is detected when the electron beam is located on the gold layer close to the edge of the hole.

Morphing of a silver nanodisk into a nanotriangle by producing a series of nanoparticles with electron beam lithography was presented [179]. Using EELS, plasmonic eigenmodes are mapped in the series of particles. As the result, they suggest that the disc modes, characterized by the angular order, can serve as a suitable basis for other nanoparticle geometries and are subject to resonance energy shifts and splittings, as well as to hybridization upon morphing. Similar to the linear combination of atomic orbitals in quantum chemistry, the authors introduced a linear combination of plasmonic eigenmodes to describe plasmon modes in different geometries [179]. LSP resonances in silver nanotriangles were mapped by EELS [53] as one of the first measurement using a monochromated transmission electron microscope in this field and presented in 2007, energy filtered transmission electron microscopy [56] as one of the pioneering measurements in this field and presented in 2009, CL [135, 180], and by EELS and CL correlated together [181], where small shifts between EELS and CL measurements are noticeable. However, these shifts are in agreement with the theory. Breathing and edge modes in aluminum nanotriangles were investigated by EELS [182]. Triangles might be used as building elements and dimers, like bowtie, and trimers are designed. Such structures were mapped by EELS, too [183].

Gold and silver nanodecahedra were mapped by both the EELS and CL [184], crescent-shape gold antennas [70] and silver split-ring resonators [185] were investigated using EELS. One of the recent EELS study covers plasmon coupling in plasmonic heterodimers made of gold and silver, or gold and aluminum [186].

Using EELS and CL, 3D tomography of LSP resonances is possible, too. CL 3D tomography was done on polystyren nanospheres covered by gold [187]. The way for a fully three-dimensional plasmon-field tomography by EELS was paved and EELS was establish as a quantitative measurement device for plasmonics [188, 189]. Correlated 3D mapping by EELS was done on a silver nanocuboid dimer [190]. Finally, a three-dimensional EELS imaging of LSP resonances was performed on silver nanocubes [191]. Silver nanocubes were also mapped by CL [192], but with no essence of 3D tomography.

New trends in EELS and CL in the field of plasmonics are illustrated, for example, by measuring the interference of surface plasmons and Smith-Purcell emission by angle-resolved CL [133], plasmon to nitrogen-vacancy color center coupling probed by photons and electrons at the nanometer scale [193], probing the symmetry of the potential of localized surface plasmon resonances with phase-shaped electron beams [194], LSP mode mixing detection and interpretation by CL [164, 176], and by measuring strong coupling phenomena using EELS in different systems, such as coupling between ZnO excitons and LSP of silver nanoparticles [87], between silver bow-tie antennas and quantum dots [88], on silver nanowires supported by hexagonal boron nitride [89], and on silver nanoparticles supported by tungsten disulfide [90].

5 Fabrication and characterization of plasmonic nanostructures

In this Chapter, auxiliary methods and results related to fabrication and characterization of plasmonic antennas are presented. It provides a general background for the following chapters that are aimed at particular scientific topics, such as fabrication procedures, quality-test protocols, selection of suitable substrates, and illustrative examples of EELS and CL measurements of plasmonic antennas.

The first part covers the fabrication of plasmonic antennas. Plasmonic nanostructures can be fabricated using many different techniques, such as chemical synthesis [30], optical lithography [31], electron beam lithography [32, 33], focused ion beam milling [34, 35], or 3D nanoprinting [36, 37]. Section 5.1 covers sample preparation using chemically synthesized nanoparticles, but not the chemical synthesis itself which is beyond the scope of this work. For detailed discussion about EBL fabrication process I refer to PhD thesis by J. Babocký [72] and references therein. Section 5.2 describes plasmonic antennas fabrication by focused ion beam (FIB) lithography. A comparison of plasmonic antennas fabricated by EBL and FIB is given in Chapter 6.

The second part covers several practical results illustrating electron beam spectroscopy in the field of plasmonics. Section 5.3 deals with CL measurements of possible substrates for plasmonic antennas. The following sections cover investigation of nanoparticles prepared by chemical synthesis: Section 5.4 deals with a gold disc-shaped nanoparticle, the first measurement of LSP by EELS at CEITEC, and a silver amalgam nanoparticle with silver satellite nanoparticles proving experimentally the energy resolution of our system. Note that the silver amalgam nanoparticles are discussed in more detail in Chapter 9. Section 5.5 introduces CL measurement of LSP resonances in a gold diabolo antenna. Section 5.6 discusses the material and the size dependency of LSP resonances in metallic nanospheres investigated by numerical simulations, which is necessary for designing more advanced experiments. Section 5.7 summarizes the study of gold spherical and triangular particles which was published in Fine Mechanics and Optics [78].

5.1 Chemically synthesized nanoparticles

The simplest plasmonic sample for electron beam spectroscopy is a dielectric substrate randomly covered by chemically synthesized plasmonic nanoparticles. In the case of SEM-CL investigation, the substrate can be a piece of any bulk material with sufficient dielectric properties and as low background cathodoluminescence signal as possible. In the case of any TEM measurement, the substrate must be a thin membrane with the thickness below 100 nm made of, for example, silicon nitride or silicon dioxide. In principle, there are two ways, how the sample can be prepared.

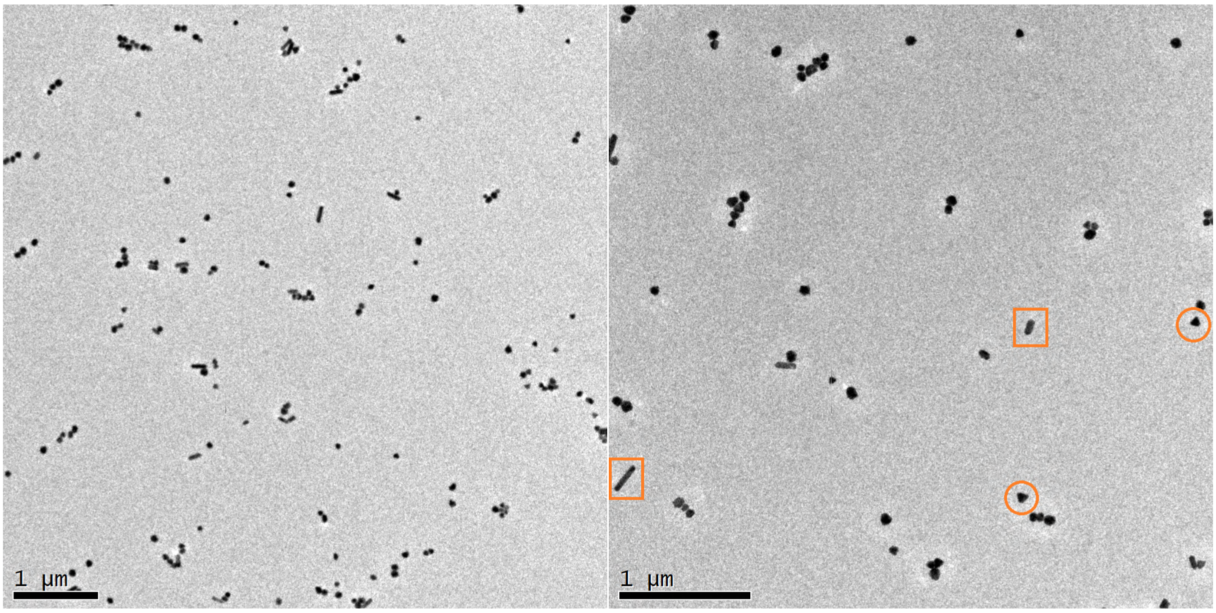

Figure 5.1: TEM micrographs of two random parts of the sample with commercial 80 nm gold nanospheres adsorbed on the surface of the 50 nm thick silicon nitride membrane. The sample was prepared by dipping the membrane into the suspension with nanospheres. Individual isolated spheres are rather frequent, but clusters are present quite often. Rods (marked by the orange rectangles in the right panel) and triangular-shaped particles (marked by the orange circles in the right panel) are rarely present, too.

The first option is dipping the substrate into the suspension with plasmonic nanoparticles for a certain time. Afterwards, the sample is removed from the suspension with some nanoparticles adsorbed to the surface. The sample described in Section 5.7 was prepared by dipping a 50 nm thick silicon nitride membrane for TEM into the suspension with gold nanospheres for 100 min. Afterwards, the sample was removed from the suspension with many nanoparticles adsorbed to the surface. The distribution of the nanoparticles over the sample surfaces (both the top side and the bottom side of the membrane) is random. Individual isolated nanoparticles are rather frequent, although clusters are present, too (see Figure 5.1).

The second option is drop-casting of several microliters of suspension onto the substrate. After drying the liquid, the sample is prepared. The sample shown in Figure 5.2 was prepared by drop-casting of 2 µl of the suspension onto a 50 nm thick silicon nitride membrane. Afterwards, the sample was kept for 2 h in a dry place to get dried. The distribution of the nanoparticles over the sample's surfaces is random. Individual isolated particles are rarely present, but the most of particles formed clusters together with some contamination. The TEM sample with silver amalgam nanoparticles (Chapter 9) was prepared in a similar way.

The main problem of both procedures is the contamination coming from the liquid phase. In an optimal case, the particles should be dispersed in demineralized water. Solvents must be vacuum compatible and must not create maps on the sample surface when dried. For example, isopropanol must not be used, because a dried drop of isopropanol on a silicon nitride membrane creates a film which is getting charged by the electron beam. As the result, such a sample cannot be measured by an electron microscope.

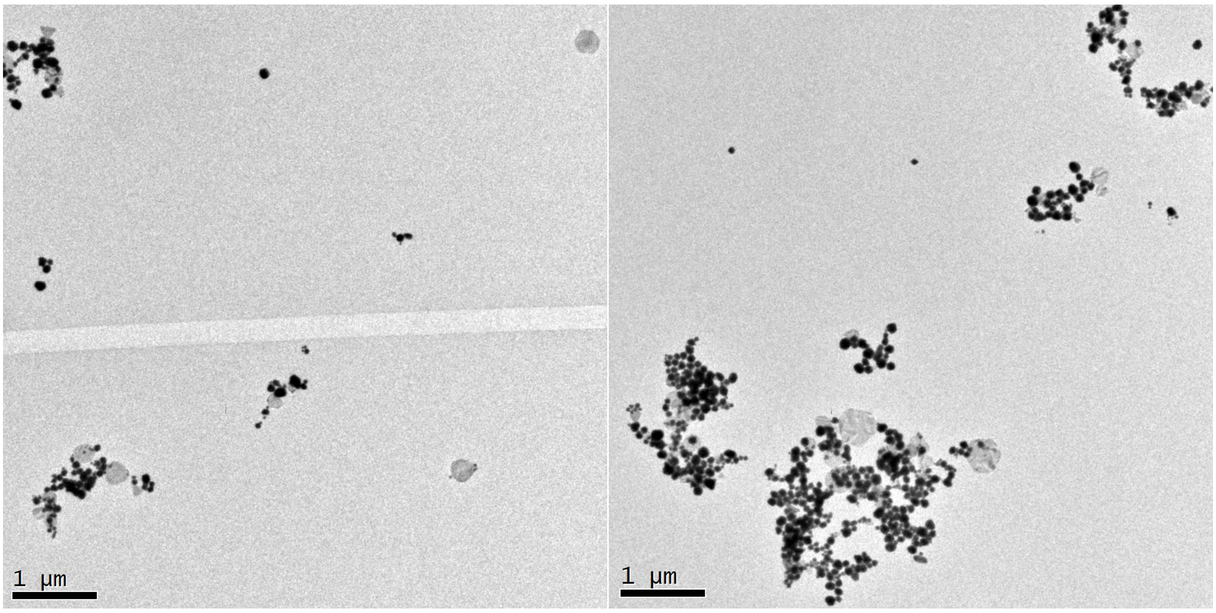

Figure 5.2: TEM micrographs of two random parts of the sample with gold nanoparticles on the surface of the 50 nm thick silicon nitride membrane. The sample was prepared by drop-casting of several microliters of suspension onto the membrane. Individual isolated particles are rarely present (gray polygon and disc-like particles), but the most of particles formed clusters together with some contamination or residues of chemical precursors (black sphere-like particles).

5.2 Focused ion beam lithography

Plasmonic antennas fabrication by FIB lithography is very straightforward. It consist of two steps. First, a thin layer of metal is deposited on a suitable substrate. The substrate can be, for example, a piece of silicon wafer or a thin silicon nitride membrane for a TEM. Second, the pristine material is patterned by the FIB. In the case of particle antennas, the volume of sputtered material is rather large as the antennas need to be positioned inside a metal-free frame that is large enough to prevent the interaction between the antenna and the frame. Therefore, the technique is suitable for fabrication of individual antennas or small arrays. For aperture antennas the volume of sputtered material is rather small and includes only the aperture itself. Therefore, fabrication of aperture antennas is rather fast.

In literature, one can find high precision plasmonic antennas fabrication by helium ion microscope [35], from a deposited metal layer [70], a single crystal gold flakes [195, 196], and a comparison between the performance of helium, gallium, and xenon focused ion beam [197].

Optimal parameters of FIB fabrication

One of the important parameters of FIB fabrication is spatial resolution. The best resolution of the FIB machine is usually at the highest ion beam energy and the lowest ion beam current. The resolution of Focused Ion Beam/Scanning Electron Microscope FEI Helios NanoLab 660 located at the CEITEC Nano Research Infrastructure is 4 nm at 30 keV with 1.1 pA ion beam current. The disadvantage of FEI Helios is that the lowest ion beam current is determined exclusively by an aperture and cannot be further decreased by changing the condenser lens focus. Consequently, the optimal parameters of FEI Helios

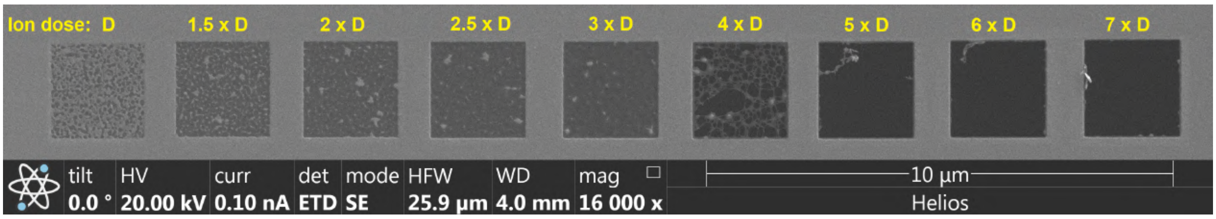

Figure 5.3: SEM image of the process of ion dose optimization. The basic dose $D = 6 \cdot 10^8$ ions per µm^2 was multiplied to test the optimal ion dose. For the dose $1 \times D$ the gold layer is milled partially and preferentially at grain boundaries. The optimal ion dose is between $2.5 \times D$ and $3 \times D$ (i.e., around $15 \cdot 10^8$ ions per µm^2) as the gold layer is removed and the membrane (dark grey) is undamaged. For the dose $4 \times D$ the membrane is partially destroyed and looks like a spider web. If the dose is $5 \times D$ or larger, the membrane is completely destroyed.

are ion beam energy of 30 keV with the 1.1 pA aperture, which should produce the ion beam current of 1.1 pA. The last important parameter is the milling time or the total ion dose. This needs to be optimized by an experiment testing different ion doses. Figure 5.3 shows milling of a 30 nm thick gold layer deposited on a 30 nm thick silicon nitride membrane. The basic dose $D = 6 \cdot 10^8$ ions per µm^2 was incrementally multiplied for several times to test the optimal ion dose. The optimal ion dose is between $2.5 \times D$ and $3 \times D$ (i.e., around $15 \cdot 10^8$ ions per µm^2) as the gold layer is removed and the membrane remains undamaged. If the ion dose is smaller, the gold layer is not fully removed. If the ion dose is higher, the membrane is totally destroyed.

The next step is to design the pattern for plasmonic antennas. Rectangular and circular plasmonic antennas can be designed using the basic shapes pre-programmed in the software of FEI Helios. The design of an aperture antenna is very simple as it is the part to be milled. In the case of a particle antenna, the gold is milled around the antenna while the antenna itself remains intact. Figure 5.4 shows an example of a disc shaped plasmonic antenna with a diameter of 150 nm located in the middle of a 2×2 µm^2 sputtered square.

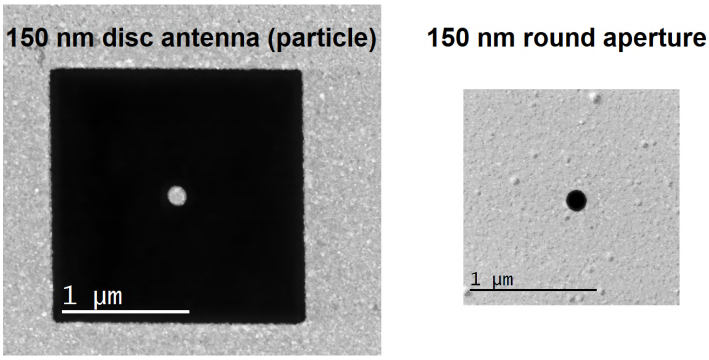

Figure 5.4: STEM dark field micrographs of a 150 nm gold disc antenna in the form of a particle (left) and aperture (right) fabricated by FIB. The black area corresponds to the removed metallic layer. The grey area corresponds to the polycrystalline gold layer. In the case of a particle (left), the area with the removed metallic layer is a square 2×2 µm^2 to prevent the interaction between the antenna and the frame.

If the shape of plasmonic antenna is more complicated, the easiest way is to create a bitmap with a milled pattern. This strategy allows to fabricate plasmonic antennas of arbitrary shapes. Figure 5.5 shows an example of a pattern for a bow-tie antenna in the form of a particle and an aperture.

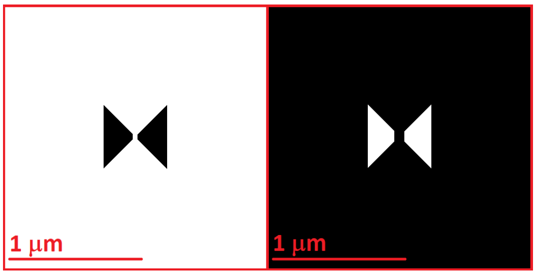

Figure 5.5: Bitmaps with the patterns designed for FIB fabrication of a bow-tie antenna in the form of a particle (left) and an aperture (right). White represents the area treated with the FIB (i.e., metal-free). Black represents the area that is not treated with FIB (i.e., metallic).

Pitfalls of FIB fabrication

The FIB fabrication of plasmonic antennas described in the previous part seems to be very straightforward. However, there are several pitfalls which need to be considered. First, the finite size of focused ion beam causes a slightly large size of the milled area than designed. Second, the shape of the metal-free area around particle-type antennas is rather important as this area is, in principle, a large aperture supporting its own LSP resonances. Third, the metallic layer may become thermally, chemically, or mechanically unstable and damaged in the way that cavities between the metallic layer and the membrane might be formed. Fourth, the adhesion layer is not necessary for the FIB fabrication of plasmonic antenna, but if any adhesion layer is present, it may act as a stopping layer for ions and at the end remain on the sample as an unwanted contamination layer. Fifth, the FIB fabrication itself might introduce some contamination like hydrocarbon layer coming from the FIB chamber environment or implantation of ions from the ion beam to the sample.

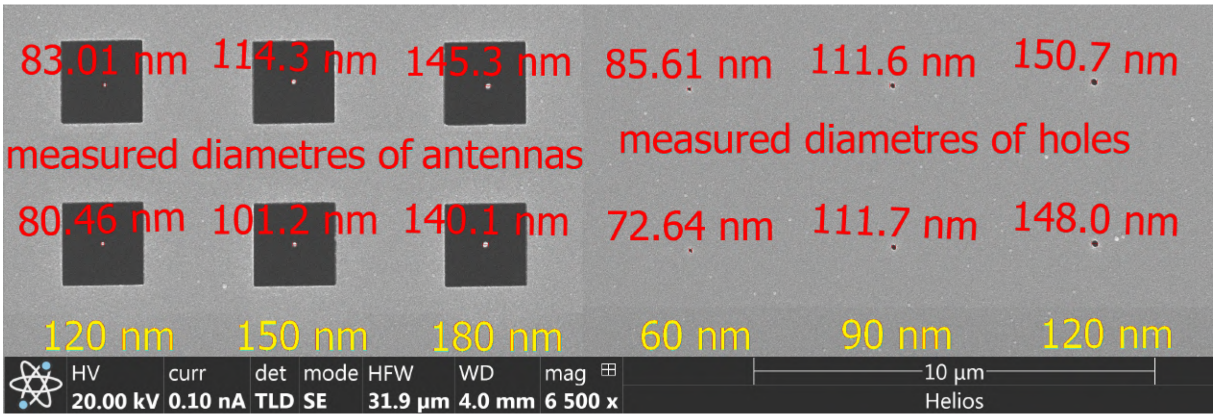

Figure 5.6: SEM image of the test series for gold disc shaped antennas in the form of particle (left) and aperture (right). The red numbers denote the real diameter of fabricated antennas measured at this SEM image, whereas the yellow numbers correspond to the diameter of the respect circle in the designed pattern.

As the focused ion beam spot is not infinitesimally small the real size of the treated area is slightly larger than its designed size. This means that fabricated particle antennas are slightly smaller than their pattern for FIB milling, whereas the fabricated aperture antennas are slightly larger than their pattern. The solution is very simple. The size of the pattern for FIB milling should be experimentally adjusted on a test series of the antennas before the fabrication of the final set. Figure 5.6 shows an example of such test series for gold disc shaped particle and aperture antennas. Note that the real diameters of the particle antennas are approximately 40 nm smaller than the diameter of the designed pattern, whereas the real diameters of the aperture antennas are approximately 20 to 30 nm larger than the diameter of the designed pattern. For example, to fabricate a disc shaped plasmonic antenna with a diameter of 110 nm, the diameter of the circle in the designed pattern should read 150 nm in the case of a particle antenna or 90 nm in the case of an aperture antenna.

The shape of metal-free area around the antenna can be, in principle, arbitrary. In the case of a disc shaped antenna the first idea is to make the surroundings circular, too. However, the metal-free area may act as a large aperture supporting its own LSP resonances. Figures 5.7 and 5.8 show a 100 nm gold disc shaped antenna located in the middle of a circular metal-free area with a diameter of 1.5 µm and in the middle of a squared metal-free area with a 2 µm long edge, respectively. The circular metal-free area supports some resonance at the energy around 2 eV (Figure 5.7), which is rather close to the LSP resonance in the 100 nm gold disc. The situation is completely different in the case of the squared metal-free area as the only detected resonance is located directly at the edge of the structure at the energy around 1.55 eV (Figure 5.7). There was detected no resonance with profound intensity in the central part of the squared metal-free area. To conclude, the size and shape of the metal-free area shall be properly designed so that its coupling to the central plasmonic antenna is excluded.

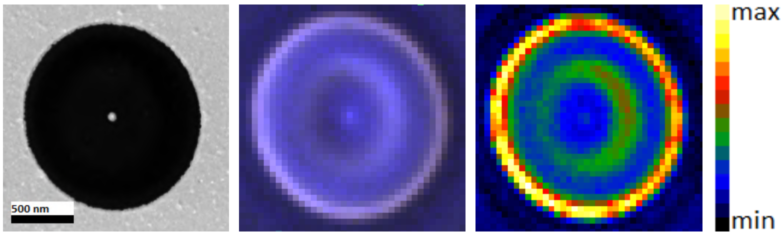

Figure 5.7: A gold disc with a diameter of 100 nm in a circular metal-free area (1.5 µm diameter). *Left to right:* STEM HAADF micrograph, CL true color map, and CL intensity map at the energy range 2.00–2.06 eV (600–620 nm).

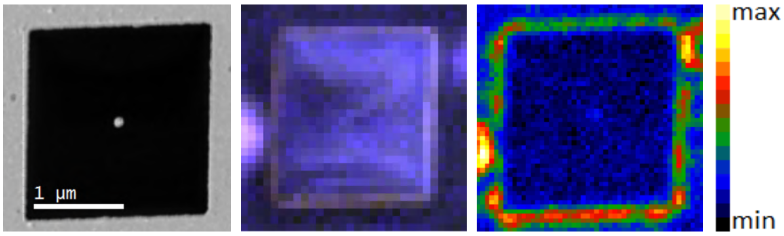

Figure 5.8: A gold disc with a diameter of 100 nm gold disc in a squared metal-free area (2 µm edge). *Left to right:* STEM HAADF micrograph, CL true color map, and CL intensity map at the energy range 1.53–1.57 eV (790–810 nm).

The finished sample consisting of a silicon nitride membrane with a gold layer seems to be very stable in time as there is, for example, nothing to oxidize. However, the sample usually undergoes cleaning in plasma and electron beam spectroscopy measurement. In both cases, the sample is heated and the metallic layer may become unstable and cavities between the metallic layer and the membrane might be formed. Figure 5.9 shows cavities between the metallic layer and the membrane which have appeared as the result of heating the sample by a highly localized intense electron beam and by plasma during the plasma cleaning. The sample consisted of a 30 nm gold polycrystalline layer on a 3 nm titanium

Figure 5.9: Cavities between the metallic layer and the membrane are formed on the sample consisting of a 30 nm thick silicon nitride membrane with a 30 nm thick deposited gold layer during plasma cleaning and during the CL measurement. *Left to right:* STEM HAADF micrograph of the area before spectrum imaging, CL true color map, and STEM HAADF micrograph of the area after spectrum imaging.

adhesion layer deposited on a 30 nm silicon nitride membrane. One can speculate, that these cavities are formed due to oxidation of the titanium adhesion layer, but this is not the case. Formation of such cavities is observed on samples with and without titanium adhesion layer as well. These cavities produce strong luminescence and therefore they are clearly visible by cathodoluminescence. As these cavities are formed under the metallic layer, they are not detrimental for particle antennas which are isolated from the cavities by the metal-free area, but they can strongly affect the apertures.

The adhesion layer between the gold layer and the silicon nitride membrane is not necessary for the FIB fabrication of plasmonic antenna. However, if any adhesion layer is present, it may act as a stopping layer for ions and at the end remain on the sample as an unwanted contamination layer. This is partially the case of a titanium adhesion layer as shown in Figure 6.4 and corresponding discussion in Chapter 6. The titanium has much slower sputtering rate than gold, therefore the gold is sputtered out preferentially so the gold distribution on the sample is better defined than in the case of no adhesion layer. If there is no adhesion layer, some rests of gold might stay on the sputtered areas of the sample. Note also that the adhesion layer may affect the LSP resonances [41, 42].

The last pitfall to be considered is the contamination coming from the FIB fabrication itself. The FIB machine is not an ultra high vacuum system and usually contains gas injection system nozzles for electron beam and ion beam induced deposition. However, the precursor gases contain metal-organic or organic-only molecules which are decomposed by the beam to a deposited material and hydrocarbons which should be pumped away by the vacuum system. As the result, the environment in the FIB chamber — when not plasma cleaned and pumped properly — contains hydrocarbons which may introduce a hydrocarbon contamination layer on the sample. Finally, the ions from the ion beam must be considered, too, as they can be easily implanted into the sample. The contamination of plasmonic antennas prepared by FIB is discussed in detail in Chapter 6 in the part related to Figure 6.4 and Table 6.1.

5.3 CL measurement of substrates

The ideal substrate should have a low CL signal and be thin enough or conductive to prevent charging. In addition, the beam energy must be selected properly. Low beam

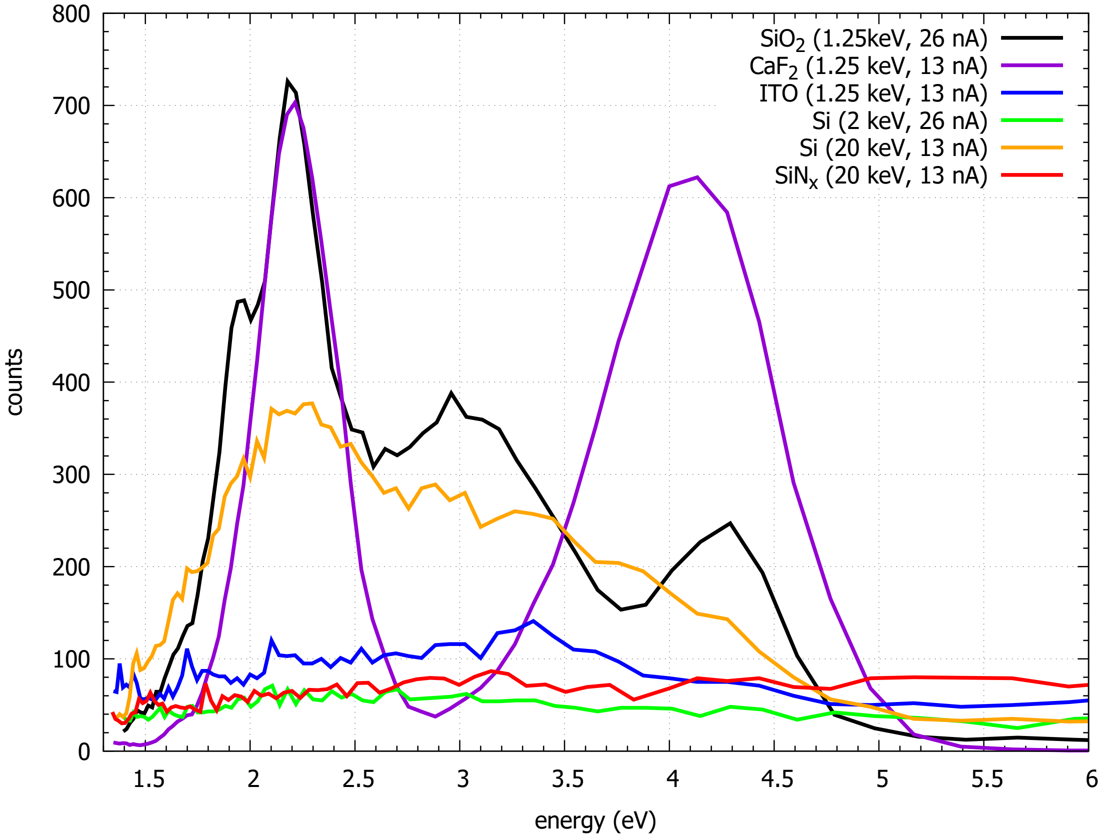

Figure 5.10: CL spectra of several common substrates: SiO_2, Si, ITO (indium-tin-oxide layer on glass), CaF_2, and SiN_x membrane measured on FEI SEM Magellan with the Gatan MonoCL4 Plus spectrometer. Counts for SiO_2 are divided by a factor of 3 and counts for CaF_2 are divided by a factor of 10. Experimental conditions (beam energy and beam current) are marked in the legend. The difference between the two silicon spectra show the importance of proper experimental parameters.

energy means a low penetration depth, a small interaction volume and therefore a low CL signal. High beam energy means a large penetration depth, a huge interaction volume and therefore a strong CL signal. Unfortunately, the most of CL intensity would come in such cases from the substrate and effects like the transition and Čerenkov radiation [51] may appear, especially when the beam energy is higher than the Čerenkov limit for the material [95].

CL spectra of several substrates, which might be suitable for plasmonic applications, namely SiO_2, Si (including a native oxide layer on the surface), ITO (indium-tin-oxide layer on glass), CaF_2, and SiN_x membrane, are summarized in Figure 5.10. CL measurement was performed on SEM FEI Magellan equipped with the Gatan MonoCL4 Plus spectrometer at LEM ISI CAS in Brno. However, only the silicon nitride membrane seemed to be a suitable substrate for CL measurements. Other substrates produce the strong CL signal (SiO_2 and CaF_2), suffer from charging (SiO_2, ITO, and CaF_2), or have the Čerenkov limit at the low energy (Si). The peaks in SiO_2 can be assigned to a non-bridging oxygen center at 1.9 eV and to the triplet and singlet luminescence of a twofold coordinated silicon center at 2.7 eV and 4.3 eV [125]. Another explanation of the peaks in SiO_2 is that the peak around 1.9 eV corresponds to residual OH or adsorbed H_2O, the peaks around 2.2 eV and 4.3 eV correspond to electron beam induced defects, and the peak around 3 eV corresponds to carbon implantation [125]. The peaks in the CaF_2 spectra can be assigned to color center peaks: F center around 2.3 eV and H center around 4.3 eV [198, 199]. The difference between the two silicon spectra plotted in Figure 5.10 for two different values of the electron energy show the importance of proper experimental parameters as 2 keV electron beam is below the Čerenkov limit of Si (which is 13.3 keV), whereas 20 keV electron beam is above this limit [95].

5.4 EELS measurement of a plasmonic nanoparticle

The crucial thing in the case of EELS measurement of LSP resonances in a plasmonic nanoparticle is the energy resolution of the method. Monochromated TEM is needed to achieve reasonably good energy resolution. A typical spectral region of interest is the low loss region including energy losses from 0 eV to 5 eV. The energy resolution is usually defined by the FWHM of the ZLP. However, the best way to prove the energy resolution is to find a simple system with two different LSP modes which are close to each other in their energy.

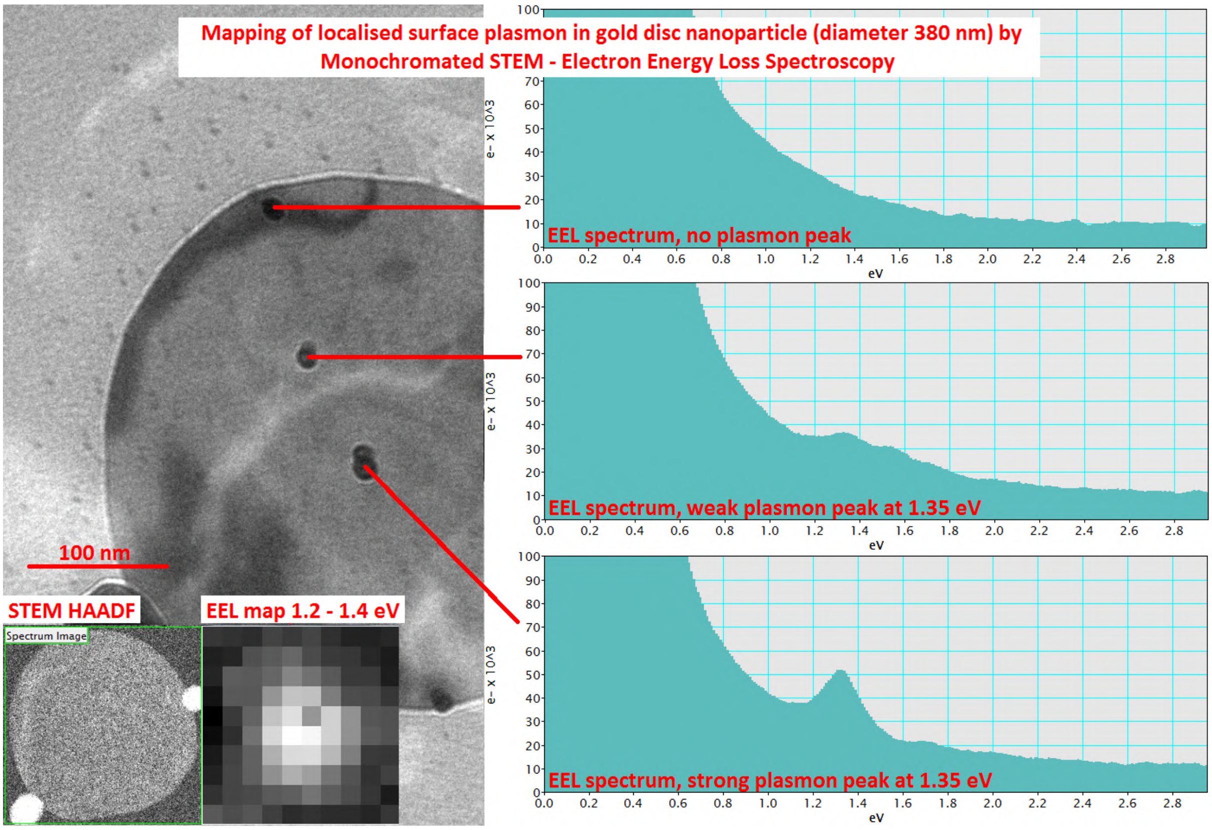

Figure 5.11: Mapping of LSP resonance in a gold disc-shaped nanoparticle with a diameter of 380 nm on a 50 nm thick silicon nitride membrane. The observed LSP resonance (breathing mode) at 1.35 eV has its maximum in the middle of the nanoparticle and vanishes with increasing the distance from the middle. The black points in TEM micrograph are carbon contamination spots grown during the measurement. This figure was presented on Ceitec Nano research infrastructure Facebook profile on June 9th, 2016 [202].

The first successful mapping of localized surface plasmon resonances in a metallic nanoparticle by electron energy loss spectroscopy in CEITEC BUT with FEI Titan Themis Cubed, which was installed in December 2015, was performed on June 7th, 2016 by me (see Figure 5.11). The object of interest was a gold disc-shaped nanoparticle with a diameter of 380 nm prepared by chemical synthesis by M. Šimšíková for another research topic [200, 201] deposited from a colloid onto a 50 nm thick silicon nitride membrane. For the whole overview of the sample see Figure 5.2 in Section 5.1 where the sample preparation is described. Observed LSP resonance (a breathing mode) at 1.35 eV has its maximum in the middle of the nanoparticle and vanishes with increasing the distance from the center.

The energy resolution of our system is illustrated in Figure 5.12 showing EEL spectra from a small silver nanoparticle located close to a large silver amalgam particle. Such structures are discussed in detail in Section 9. In this case, two modes are observed: a dipole mode (3.54 eV) and a breathing mode (3.74 eV) of the small silver satellite particle. To prove the energy resolution of our system experimentally, the spectra are integrated over the region of interest (red square in Figure 5.12) which includes both modes overlapping together. These two modes with an energy difference of 0.2 eV are well resolved in the spectra as two different peaks while the ZLP FWHM is 0.15 eV.

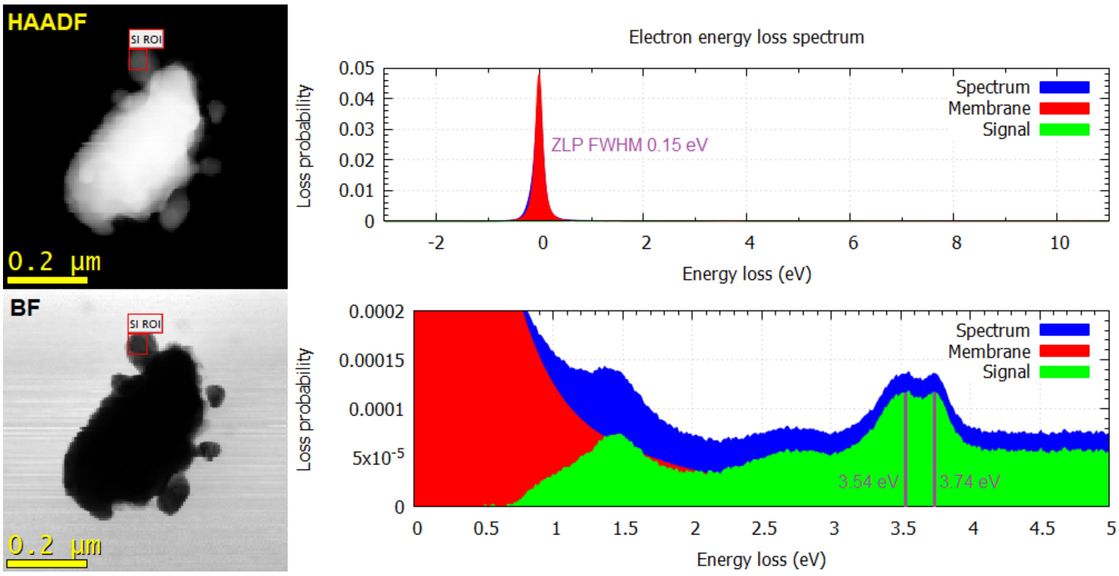

Figure 5.12: *Left:* STEM BF and STEM HAADF micrograph of an silver amalgam nanoparticle with silver satellites around. The region of interest (ROI), marked by the red square, contains the silver nanosphere with a diameter around 40 nm. *Right:* EEL spectra integrated over the ROI experimentally proving the peak to peak resolution of 0.2 eV while the dipole mode (3.54 eV) and the breathing mode (3.74 eV) of the nanoparticle are well distinguishable in the spectra. The top graph shows the whole recorded spectrum, whereas the bottom graph shows the same spectra, but the area of interest is zoomed in.

5.5 CL measurement of a plasmonic antenna

The crucial parameter in the case of CL measurement of LSP resonances in a plasmonic nanoparticle is the exposure time. To achieve a reasonably good signal-to-noise ratio a large electron beam current is needed. Electron beam currents in the range from 1 nA to 30 nA are used. The accessible spectral region is limited by the CL spectrometer and ranges typically from 1 eV to 4 eV. The energy resolution is much better than in EELS and is limited just by the spectrometer, typically around 10 meV.

Figure 5.13 shows the CL measurement of a gold diabolo antenna with a total length of 290 nm using TEM FEI Tecnai F20 with Gatan VULCAN at USTEM TU Wien.

The panchromatic CL image is obtained as the total intensity integrated over the whole recorded spectrum. The true color CL image is the image where the color of every pixel is recalculated from the CL spectra recorded in this pixel. Graphs in Figure 5.13 show the CL spectrum integrated over the region of interest, the bridge of the diabolo antenna, as recorded and after correction and background subtraction. The correction consists of multiplying the recorded spectra by a system specific correction function which includes all effects of the system performance, like wavelength dependent efficiency of the CCD and mirrors and absorption in optical fibers. Such a correction function can be evaluated experimentally by transition radiation measurement and comparing the experimental result with the theory [58]. Background subtraction is performed by subtracting the CL signal recorded on the membrane far away from any plasmonic structure.

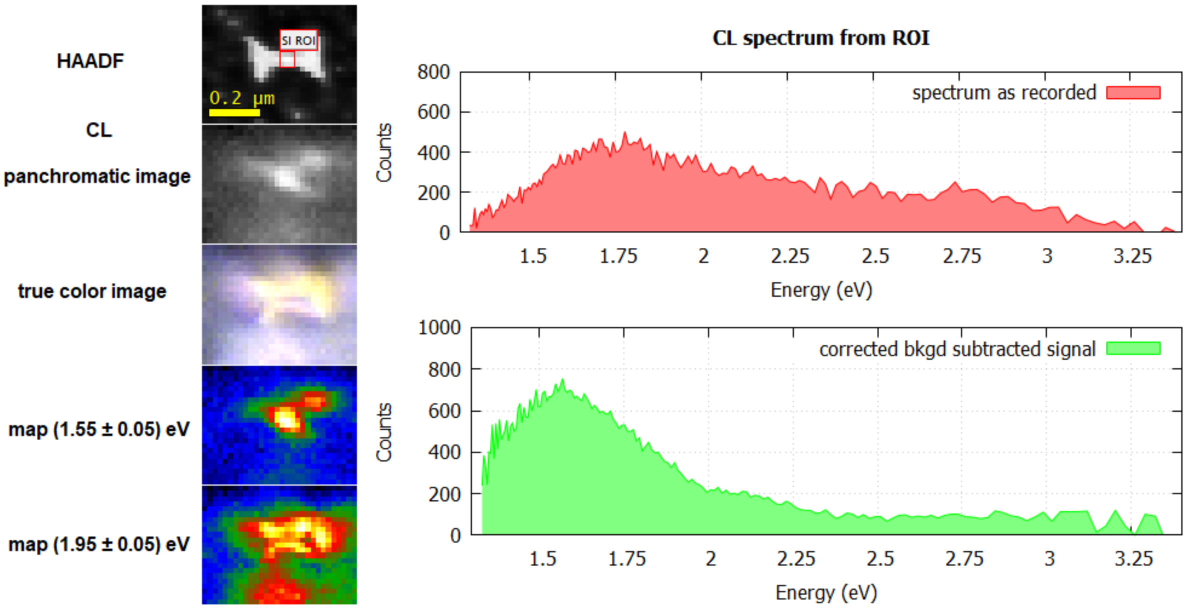

Figure 5.13: Cathodoluminescence measurement of a 290 nm long gold diabolo antenna. Left panels show STEM HAADF micrograph of the diabolo antenna with the marked region of interest (ROI), panchromatic CL image, true color CL image, and two energy filtered maps at 1.55 eV and 1.95 eV corresponding to the gap and the edge mode, respectively. The graphs show the CL spectrum integrated over the region of interest, the bridge of the diabolo antenna, as recorded and after correction and background subtraction.

5.6 Localized surface plasmons in metallic nanospheres

The energy of LSP resonances in spheres depends on their diameter and the dielectric properties of the sphere and the medium around. Material dependency is illustrated in Figure 5.14 presenting calculated EEL spectra for nanospheres with a diameter of 80 nm for four different metals common in plasmonics: gold, silver, aluminum, and copper [203]. In BEM simulations, the dielectric functions of copper, gold, and silver from Reference [204] and aluminum from Reference [205] were used. The 300 keV electron beam with FWHM of 0.1 eV was located 5 nm outside the sphere. The strongest plasmonic response (the highest peak) has been observed for a silver nanosphere, whose spectrum consists of a double peak with maxima at 3.20 eV and 3.57 eV). The second strongest plasmonic response has been found for a gold nanosphere, whose spectrum consists of a

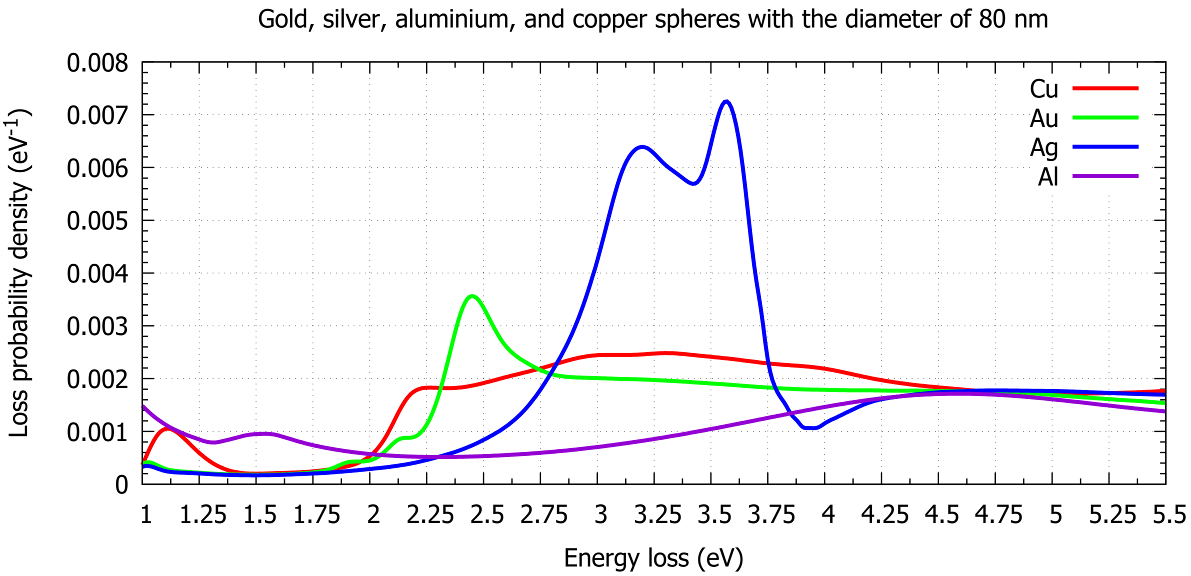

Figure 5.14: EEL spectra simulated by BEM for gold, silver, aluminum, and copper nanospheres with a diameter of 80 nm in vacuum. The dielectric functions of copper, gold, and silver were used from Reference [204] and aluminum from Reference [205]. The 300 keV electron beam with FWHM of 0.1 eV was located 5 nm outside the sphere.

single peak at 2.45 eV. Aluminum nanosphere has had a broad peak around 4.6 eV and copper nanosphere indicates just a significantly weak LSP peak around 2.2 eV. Other features in the spectra do not correspond to the plasmon resonances, but are connected, for example, with absorption in the material, which can be easily verified by computing EEL spectra for spheres of different sizes. In such case, the peak corresponding to LSP resonance changes and its energy is shifted, but the peak corresponding to absorption in the material remains nearly the same.

As the simplest EEL spectrum has the gold nanosphere, the size dependency is illustrated in Figure 5.15 showing simulated EEL spectra for gold nanospheres of different diameters. In BEM simulations, the dielectric function of gold was taken from Reference [206]. The 300 keV electron beam with FWHM of 0.1 eV was located 5 nm outside the sphere. The results of the boundary element method are in perfect agreement with the solution according to the Mie theory. With an increasing diameter, LSP resonance shifts to lower energies (it means to higher wavelengths, therefore the *redshift*) and the loss probability of the resonance increases.

Figure 5.16 shows the comparison of EEL spectra simulated by BEM for gold nanospheres with a diameter of 80 nm in vacuum using different dielectric functions of gold: dielectric function measured by reflective EELS by Werner, Glansching, and Ambrosch-Draxl [207], dielectric function from Handbook of optical constants by Palik [204], dielectric functions measured by ellipsometry by McPeak et al. [203] and Olmon et al. for both the gold single crystal and polycrystalline evaporated gold layer [208], and the dielectric function by Johnson and Christy [206]. The 300 keV electron beam with FWHM of 0.1 eV was located 5 nm outside the sphere. The results are quite similar for dielectric functions by McPeak et al., Olmon et al. (both of them), and Johnson and Christy. The peak energy is in the range from 2.41 eV to 2.44 eV and the maximal loss probability density is in the range from 0.0035 eV^{-1} to 0.0041 eV^{-1}. The result computed using the dielectric function by Palik shows additional small peaks around 1.8 eV and 2.1 eV, which are not present in the case of any other dielectric functions. Finally, the result calculated using the dielectric function measured by reflective EELS is completely different predicting the LSP resonance around 2.9 eV.

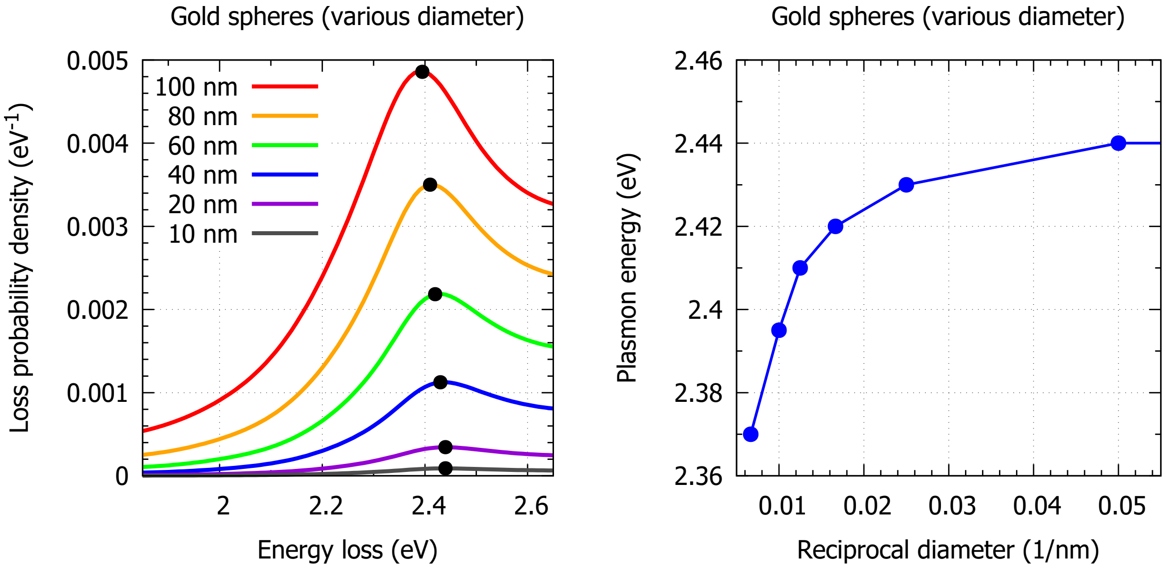

Figure 5.15: *Left:* EEL spectra simulated by BEM for gold nanospheres of different diameters in vacuum. *Right:* Dispersion relation of the dipole LSP resonance in gold nanospheres. The points correspond to the LSP resonance energies in the left graph (marked by black points). The dielectric function of gold from Reference [206] was used. The 300 keV electron beam with FWHM of 0.1 eV was located 5 nm outside the sphere.

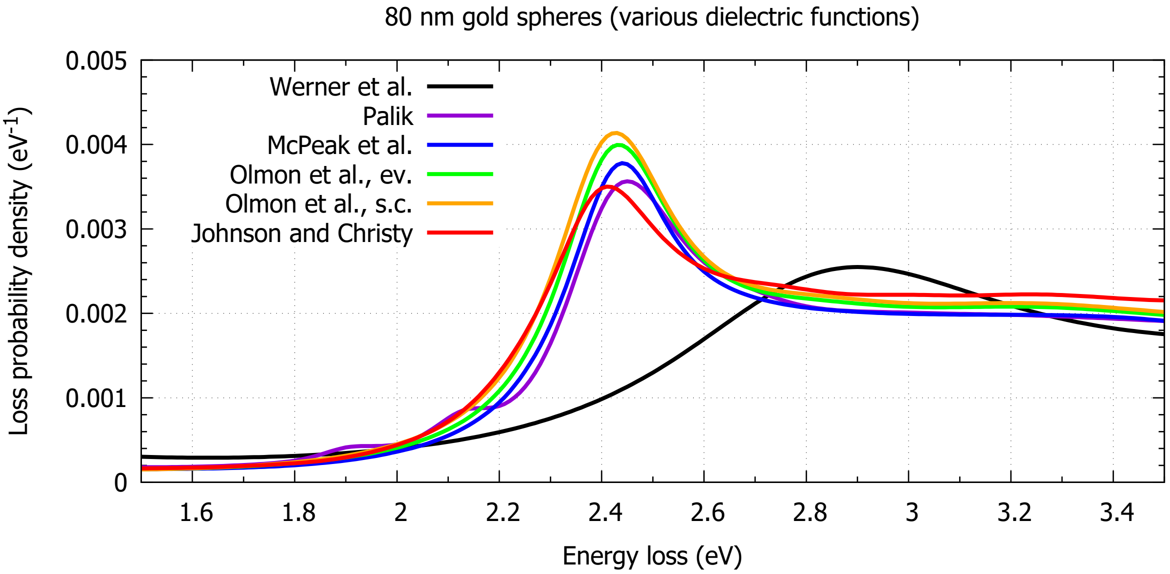

Figure 5.16: EEL spectra simulated by BEM for gold nanospheres with a diameter of 80 nm in vacuum using different dielectric functions of gold: dielectric function measured by reflective EELS by Werner, Glansching, and Ambrosch-Draxl [207], dielectric function from Handbook of optical constants by Palik [204], dielectric functions measured by ellipsometry by McPeak et al. [203] and Olmon et al. for both the gold single crystal (s.c.) and polycrystalline evaporated gold layer (ev.) [208], and the dielectric function by Johnson and Christy [206]. The 300 keV electron beam with FWHM of 0.1 eV was located 5 nm outside the sphere.

5.7 Gold nanospheres and nanotriangles

Nanoparticles prepared by chemical synthesis are monocrystalline or close to single crystals. Consequently, their plasmon resonances are stronger than in similar polycrystalline bodies, where grain boundaries and defects contribute to the electron scattering.

Gold spheres with the diameter of 80 nm were investigated by both EELS and CL. The sample preparation is described in section 5.1. The EELS and CL investigation was performed on two nanospheres with the same diameter.

EELS investigation was carried out by the transmission electron microscope FEI Titan Themis with the GIF Quantum spectrometer. The EEL spectrum, measured at the border of the sphere, is shown in Figure 5.17 left. The spectrum consists of a single resonance with an energy of 2.4 eV, which is in perfect agreement with the theory represented by BEM simulation using the dielectric function of gold by Johnson and Christy [206] and neglecting the membrane. The spatial distribution of the loss probability at the energy of the resonance is shown in Figure 5.18.

CL measurement was performed using the scanning electron microscope FEI Magellan equipped with the Gatan MonoCL4 Plus spectrometer at LEM ISI CAS in Brno. Measured spectrum is in good agreement with FDTD simulation in Lumerical using the dielectric function of gold by Johnson and Christy [206] and the dielectric function of Si_3N_4 by McIntosh et al. [209], see Figure 5.17 right. In the CL spectrum, three peaks are present: the first at 2.43 eV, the second at 2.21 eV, and the third at 1.98 eV. The CL measurement requires a high electron beam current to produce enough light. Consequently, the electron beam diameter was too large to see any spatial dependence. CL mapping with much better spatial resolution was performed on the transmission electron microscope FEI Tecnai F20 with the Gatan VULCAN spectrometer in the STEM mode at USTEM TU Wien. Intensity maps at the energies (wavelengths) corresponding to the peaks in the CL spectrum (Figure 5.19) show the spatial distribution of the luminescence intensity.

Nanotriangles are basic building elements for more complex structures with advanced functionalities, like *bow-tie* (with an electric field hot spot) [210] and *diabolo* (with a magnetic field hot spot) [211] discussed in Chapter 8. They were occasionally present on the sample with gold spheres (Figure 5.1). The EELS and CL mapping of LSP resonances was again performed on two different nanoparticles (of the similar shape and size), because it was impossible to locate a specific nanoparticle on the sample due to their random distribution. It must be noticed, that just the planar projection showing the triangular-shape is observed, the real shape (especially the thickness profile) of the particles is unknown.

As in the case of nanospheres, EELS investigation was performed on the TEM FEI Titan Themis with the GIF Quantum spectrometer. Three different resonances are observed. EEL spectra recorded at different positions are plotted in Figure 5.20 left. Spatial distributions of the resonances, the corner mode at 2.05 eV, the edge mode at 2.38 eV, and the breathing mode at 2.55 eV, are shown in Figure 5.21.

CL measurement was again performed on the TEM FEI Tecnai F20 with the Gatan VULCAN spectrometer at USTEM TU Wien. The CL investigation shows only one radiative LSP mode, the edge mode. The spectrum is plotted in Figure 5.20 right, and the spatial distribution of the resonance in the form of an intensity map at the energy corresponding to the spectrum peak is shown in Figure 5.22.

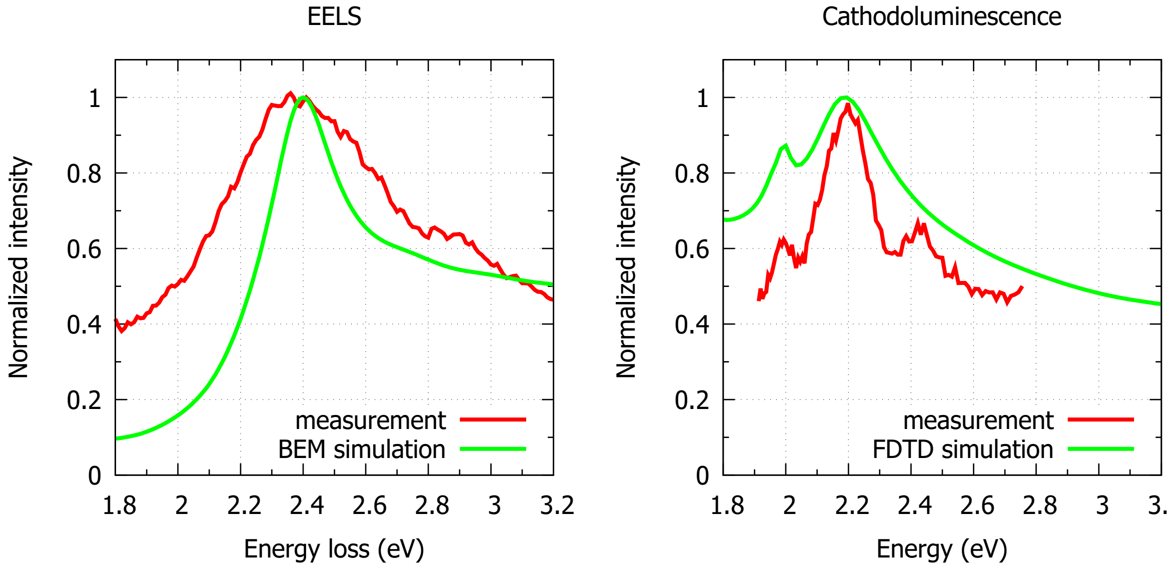

Figure 5.17: Measured EEL (left) and CL (right) spectra of two gold nanospheres with the diameter of 80 nm (one for EELS, another for CL) on a 50 nm thick silicon nitride membrane compared to the spectra obtained from simulations (left: BEM, right: FDTD). It is worth mentioning that no processing was applied to the spectra. In the BEM simulation, the substrate (membrane) is neglected.

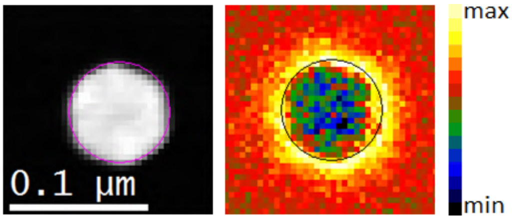

Figure 5.18: STEM dark field micrograph of the gold sphere with the diameter of 80 nm (left) and EEL intensity map (right) at the energy of (2.4 ± 0.1) eV, the peak position in the EEL spectrum in Figure 5.17. Circles with the diameter of 80 nm are marking the position of the sphere.

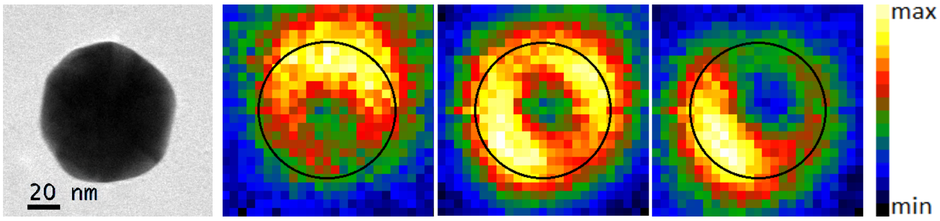

Figure 5.19: *Left to right:* TEM bright field micrograph of the gold sphere with the diameter of 80 nm; CL intensity maps at the energies corresponding to the peak positions in the CL spectrum in Figure 5.17: (1.98 ± 0.04) eV, (2.21 ± 0.04) eV, and (2.43 ± 0.05) eV. The corresponding wavelengths are (625 ± 10) nm, (560 ± 10) nm, and (510 ± 10) nm. Black circles with the diameter of 80 nm are marking the position of the sphere.

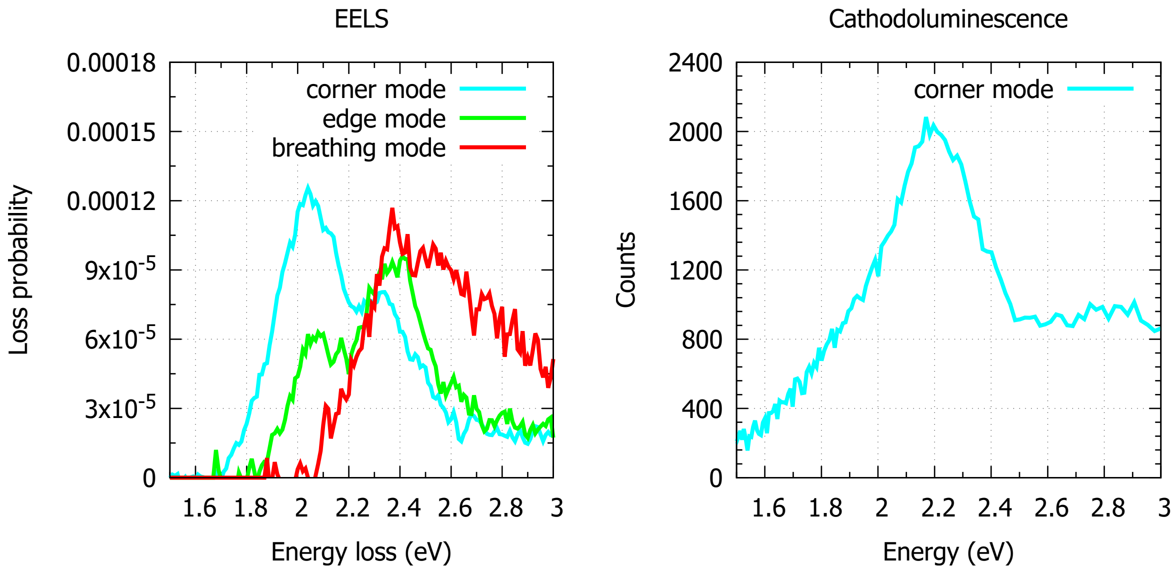

Figure 5.20: Measured EEL (left) and CL (right) spectra of LSP resonances in two different gold triangular nanoparticles. The EEL spectra are background subtracted and integrated over several pixels in the corner, in the center, and in the middle of the edge of the particle. The CL spectrum shows a LSP resonance only in the corner of the particle.

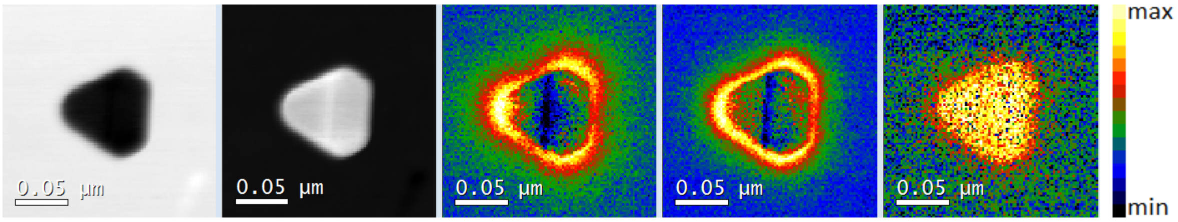

Figure 5.21: *Left to right:* STEM bright and dark field micrograph of the gold triangular particle; EEL intensity maps at the energy of (2.05 ± 0.05) eV (corner mode), (2.38 ± 0.05) eV (edge mode), and (2.55 ± 0.05) eV (breathing mode overlapped with absorption in gold), the peak positions in the EEL spectrum shown in Figure 5.20.

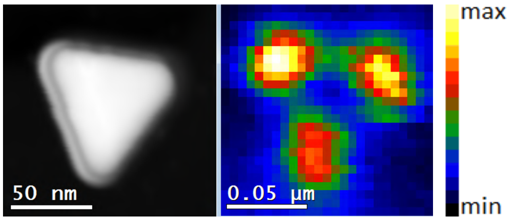

Figure 5.22: Dark field micrograph of the gold triangular particle (left) and CL intensity map at the wavelength of (570 ± 10) nm. The corresponding energy is (2.18 ± 0.04) eV, the peak position in the CL spectrum shown in Figure 5.20.

6 Plasmonic antennas fabricated by electron beam and focused ion beam lithography

This Chapter summarizes a comparative study of plasmonic antennas fabricated by electron beam and focused ion beam lithography published in Scientific Reports [75]. Plasmonic antennas are often fabricated by electron beam lithography (EBL) or focused ion beam (FIB) milling. The EBL process consists of the following steps: (i) deposition of a resist sensitive to electron beam on a substrate, (ii) exposition of the resist to the electron beam and development of the resist (removal of exposed or unexposed regions of the resist), (iii) deposition of a thin layer of metal, and (iv) removal of the remaining resist covered by the redundant metal (lift-off) and final cleaning of the sample. FIB lithography is more straightforward, consisting of two steps: (i) deposition of a thin layer of metal and (ii) exposition to a focused ion beam that locally sputters off the metal (Figure 6.1). Both the EBL process and the FIB milling are capable to create sub-10-nm structures [35, 212].

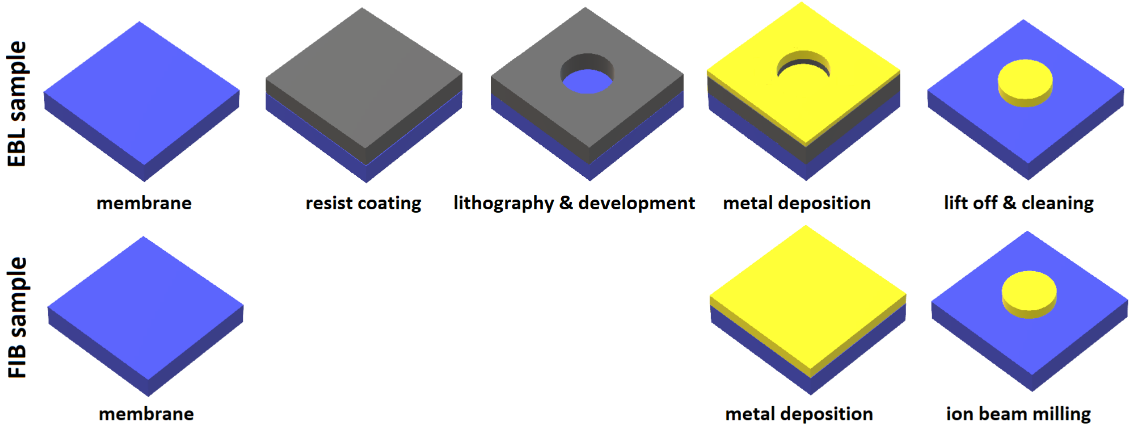

Figure 6.1: Schematic overview of individual steps in the fabrication process of the EBL and the FIB antennas.

Naturally, both fabrication techniques have their advantages and disadvantages. In EBL, final structures can be contaminated by the residual resist or solvents. Lift-off can exert a pronounced mechanical force that can damage the fabricated structure or even the substrate, which is particularly dangerous for thin membranes used as the substrate. In FIB, large-area mechanical effects are absent but the focused ion beam can damage the sample locally. Redeposition of sputtered-off metal atoms can reduce the quality of products of the technique. There are no chemicals involved in the process but the ions in the milling beam and atoms sputtered from the metal and substrate can still contaminate the fabricated structures. EBL consists of more steps but is more suitable for large area lithography as the exposition, the only local process, is considerably faster than for FIB. On the other hand, FIB is faster when only a single antenna or a small field of antennas is being fabricated. For example, considering optimal parameters for FIB and EBL (see the Methods section), FIB milling of one antenna inside a $2 \times 2\,\mu\mathrm{m}^2$ metal-free square takes typically 2 minutes. Array of 50×50 antennas is fabricated in 84 hours (3.5 days). On the other hand, in EBL the length of chemical processes (resist coating, development, and lift off) is independent on the number of fabricated antennas and takes typically 6 hours. Electron beam exposition of one antenna lasts far below 1 second; the array of 50×50 antennas is exposed in 5 seconds. FIB enables fabrication of single crystalline plasmonic antennas when a chemically grown single crystal gold flake transferred onto a substrate is used as the pristine material instead of a sputtered or an evaporated polycrystalline thin film [195, 196]. The quality of lithographically fabricated plasmonic antennas can be further enhanced by annealing which enlarges the grains and accordingly reduces the number of grain boundaries so the behavior of nanostructures is closer to a single crystal [43, 44]. It is clear that suitability of both methods depends on specific tasks and experimental comparison of the structures fabricated by both methods is of high importance for the judicious selection of the optimal method.

Four individual disc-shaped gold plasmonic antennas were studied in detail: two series prepared by both EBL and FIB consisting of antennas with designed diameters of 120 nm and 140 nm and with designed height of 25 nm. After their fabrication, several characterization methods have been applied. Some of those methods can modify the samples. In particular, a hydrocarbon contamination is developing during measurements in electron microscopes using high beam current (i.e., EELS and EDS) [213, 214]. For this reason, the characterization methods have been applied in specific order for all investigated antennas: EELS, EDS, AFM. As possible contamination is considered to be a part of PA functionality, no specific cleaning steps have been applied between individual measurements. In particular, no plasma cleaning has been applied prior to EELS measurements, although it is often used to remove the hydrocarbon contamination.

6.1 Methods

Standard 50 nm thick silicon nitride membranes for TEM with a window size of $250 \times 250\,\mu\mathrm{m}^2$ and frame thickness of 200 µm by Silson Ltd. (UK) were used.

Electron beam lithography (EBL) was performed using the following procedure. As the resist, we used a 70 nm thick layer of poly(methyl methacrylate) 679.02 all-resist dissolved in ethyl acetate. The exposition has been performed within the Tescan MIRA3/RAITH SEM operated at 30 kV with the electron beam current of 100 pA and the dose of $320\,\mu\mathrm{C\,cm}^{-2}$. Exposed samples were developed in the developer AR 600-56 all-resist for 3 minutes, as the stopper we used isopropyl alcohol for 30 seconds. Afterwards, the sample was cleaned by demineralized water for 30 seconds. Lift-off was performed by 4 hour acetone bath applying mega sound for 1 hour finished by acetone stream wash. Finally, the sample was cleaned by isopropyl alcohol for 30 seconds, followed by cleaning using ethanol for 30 seconds and demineralized water for 30 seconds. To prevent the collective interaction of the antennas we fabricated individual isolated antennas with a distance between two nearby antennas of 3 µm.

Metal deposition was done in the electron beam evaporator BESTEC. Pressure during the deposition was in the order of 10^{-5} Pa and voltage was set to 8 kV. We deposited a 5 nm Ti adhesion layer at a deposition speed of $0.05\,\mathrm{nm\,s^{-1}}$ and a 25 nm Au layer at a deposition speed of $0.02\,\mathrm{nm\,s^{-1}}$. Metal pellets were purchased from Kurt J. Lesker Company. Membranes were rotated at a speed of 10 rpm (revolutions per minute) to ensure the homogeneity of the layers. Both samples were deposited during one session to have exactly the same metallic layer on both of them. During the deposition, the thickness of the layer was measured in situ by a quartz crystal microbalance monitor.

Focused ion beam (FIB) lithography was performed in the dual beam FIB/SEM microscope FEI Helios using gallium ions with the energy of 30 keV and ion beam current of 2.4 pA. The energy (the highest available) and the current (the lowest available) are optimized for the best spatial resolution of the milling. The antennas were located in the middle of a $2 \times 2\,\mathrm{\mu m^2}$ metal-free square, which is perfectly sufficient to prevent their interaction with the surrounding metallic frame [70].

Electron energy loss spectroscopy (EELS) measurements were performed with the TEM FEI Titan equipped with the GIF Quantum spectrometer operated in the monochromated scanning regime at 300 kV. The beam current was set to 0.8 nA and the FWHM of the ZLP was around 0.18 eV. The convergence angle was set to 10 mrad, the collection angle to 20.5 mrad, and the dispersion of the spectrometer to 0.01 eV/pixel. EELS spectrum images were recorded with the size of $300 \times 300\,\mathrm{nm^2}$ (100×100 pixels with the pixel size of 3 nm). In every pixel of the spectrum image 30 EEL spectra were recorded within the total pixel time of 20 ms. They were further cross-correlated and summed up. EEL spectra were integrated over the ring-shaped areas around the disc edge where the LSP resonance is significant (inner diameter about 50 nm, outer diameter about 200 nm) and divided by the integral intensity of the whole spectrum to transform measured counts to a quantity proportional to the loss probability. EEL maps were calculated by dividing the map of integrated intensity at the plasmon peak energy with an energy window of 0.1 eV by the map of the integral intensity of the zero-loss peak. Radial distributions of LSP resonances were calculated from the EEL maps by rotational averaging (considering the azimuthal symmetry of a disc) followed by the background subtraction (base level of the intensity in the EEL maps far away from the antennas).

Energy dispersive X-ray spectroscopy (EDS) measurement was performed on the TEM FEI Titan equipped with the Super-X spectrometer operated in the scanning regime at 300 kV. The electron beam current was set to 2 nA. EDS spectrum images were recorded with the size of $600 \times 600\,\mathrm{nm^2}$ (300×300 pixels with the pixel size of 2 nm) using integration of 100 images with the acquisition time of 10 µs per pixel. Spectrum images were post processed in the Velox software. EDS maps show the net intensity (i.e. background subtracted and artifact corrected intensity). EDS quantification in atomic percents was performed in the Velox software using a parabolic background model and Brown-Powell ionization cross-section model.

Atomic force microscopy (AFM) measurement was performed using the Scanning Probe Microscope Bruker Dimension Icon in the PeakForce Tapping mode, which enables larger control over applied force to prevent damaging the membrane [215]. The peak force setpoint was set to 5 nN, the scanning window was $400 \times 400\,\mathrm{nm^2}$ (256×256 pixels with the pixel size of 1.6 nm).

Numerical simulations of EELS spectra were performed using the MNPBEM toolbox [151, 152] based on the boundary element method (BEM). The dielectric function of evaporated gold was taken from Olmon et al. [208] and the dielectric function of the silicon nitride membrane was set to 4 [179]. The titanium adhesion layer has been neglected in the simulations. For the calculations of spectra the electron beam was positioned 2 nm from the outer side of the antenna. The obtained loss probability density was recalculated to loss probability at 0.01 eV energy intervals (corresponding to the dispersion of the spectrometer in the experiment 0.01 eV per pixel).

6.2 Results

The three-dimensional (3D) morphology of the antennas measured by EELS in terms of relative thickness is shown in Figure 6.2. The average relative thickness is (0.23 ± 0.05) for 120 nm EBL antenna, (0.20 ± 0.07) for 120 nm FIB antenna, (0.23 ± 0.05) for 140 nm EBL antenna, and (0.20 ± 0.06) for 140 nm FIB antenna, see also Figure 6.3d. The relative thickness is proportional to the absolute thickness of the antenna with the inelastic mean free path (IMFP) as the constant of proportionality. The IMFP in gold for the actual parameters of the electron beam (electron energy of 300 keV and collection semi-angle of 20.5 mrad) calculated using the software package EELSTools by D. Mitchell [216] applying the algorithm of K. Iakoubovskii et al. [106] equals to 113 nm. Consequently, the absolute thickness of the antennas is (23 ± 7) nm for FIB antennas and about (26 ± 6) nm for EBL antennas, which is in a good agreement with the desired value of 25 nm. Diameters of fabricated antennas measured from TEM micrographs indicate good agreement between the designed and actual value. They read (125 ± 5) nm for the 120 nm EBL antenna, (122 ± 6) nm for the 120 nm FIB antenna, (140 ± 6) nm for the 140 nm EBL antenna, and (142 ± 7) nm for the 140 nm FIB antenna.

There is a clear structural difference between EBL and FIB antennas. The EBL antennas have an irregular shape and their thickness varies rapidly with the position as the gold layer is polycrystalline with a grain size of about 20 nm. The FIB antennas are seemingly more uniform in the thickness and their edges are smooth and featureless. Nevertheless, a closer inspection (see Figure 6.3d) reveals even more pronounced thickness profile (i.e. with a larger amplitude) but smoother (i.e. with a reduced slope) variations of the thickness with a magnitude of nearly 10 nm. The flat boundary is mainly caused by two reasons. First, the metallic layer is deposited on the flat substrate for FIB but on the patterned resist for EBL forming a flat layer in the former case and frayed edges in the latter case. Second, the ion beam has a Gaussian-like profile which leads to smoothing of the edges. Additionally, the ion beam may result into amorphization and recrystallization of gold, smoothening its surface [217]. Finally, redeposition of sputtered-off gold may contribute to the smoothness of the gold surface and might be also partially responsible for the large magnitude of the thickness variation.

Next, EEL spectra were processed to obtain the loss probability related to LSP resonances. This included ZLP and background subtraction. The process is illustrated in Figure 6.3a showing the unprocessed low-loss part of the EEL spectrum decomposed into the contribution of ZLP and background, and signal corresponding to the LSP resonance for the 120 nm EBL antenna. Extracted EEL signal corresponding to the LSP resonance is shown in Figure 6.3b for 120 nm antennas and in Figure 6.3c for 140 nm antennas. Within the spectra a single broad peak corresponding to the dipole LSP mode is resolved. This assignment is further supported by the results of numeric simulations, also shown in Figure 6.3b,c. It is also in agreement with prior investigations of plasmonic disc-shaped antennas [175]. The second peak in the calculated spectra corresponds to the quadrupole LSP mode. Due to its low intensity and instrumental broadening, related to the energy width of the impinging electron beam with the FWHM of about 0.18 eV, this mode is not resolvable in the experimental data. The simulation predicts an energy of the dipole

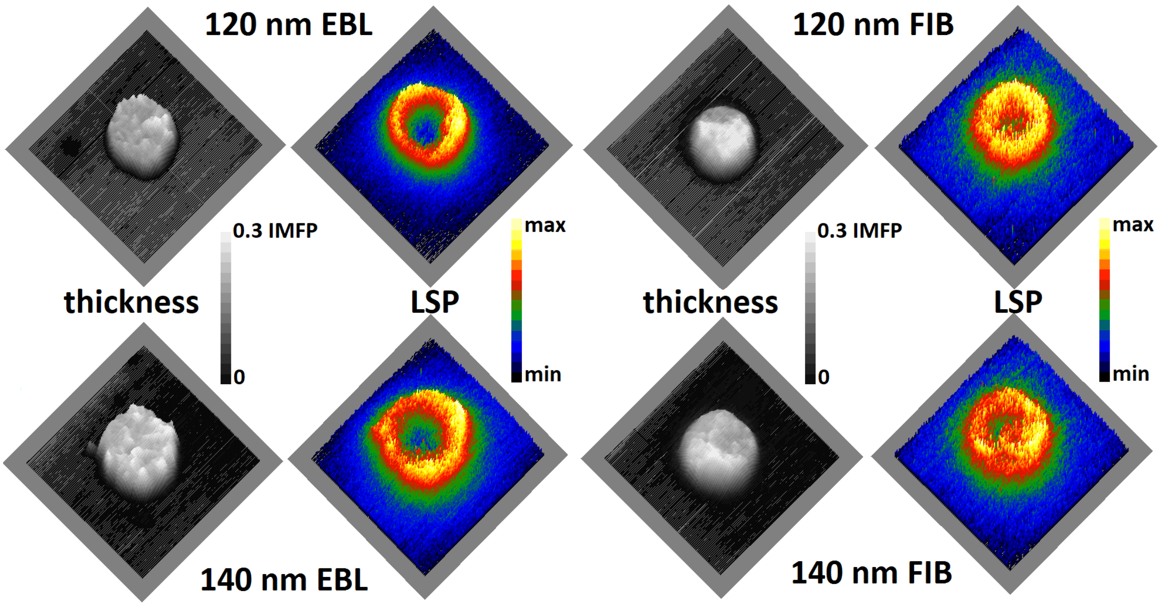

Figure 6.2: Thickness and LSP resonance mapping by EELS. 3D morphology of the antennas represented by the relative thickness (thickness in units of inelastic mean free path, IMFP) measured by EELS (left, grayscale) and EEL intensity maps showing the spatial distribution of LSP resonance at (1.60 ± 0.05) eV for 120 nm antennas and (1.40 ± 0.05) eV for 140 nm antennas (right, color scale). The size of all micrographs is $300 \times 300\,\mathrm{nm}^2$.

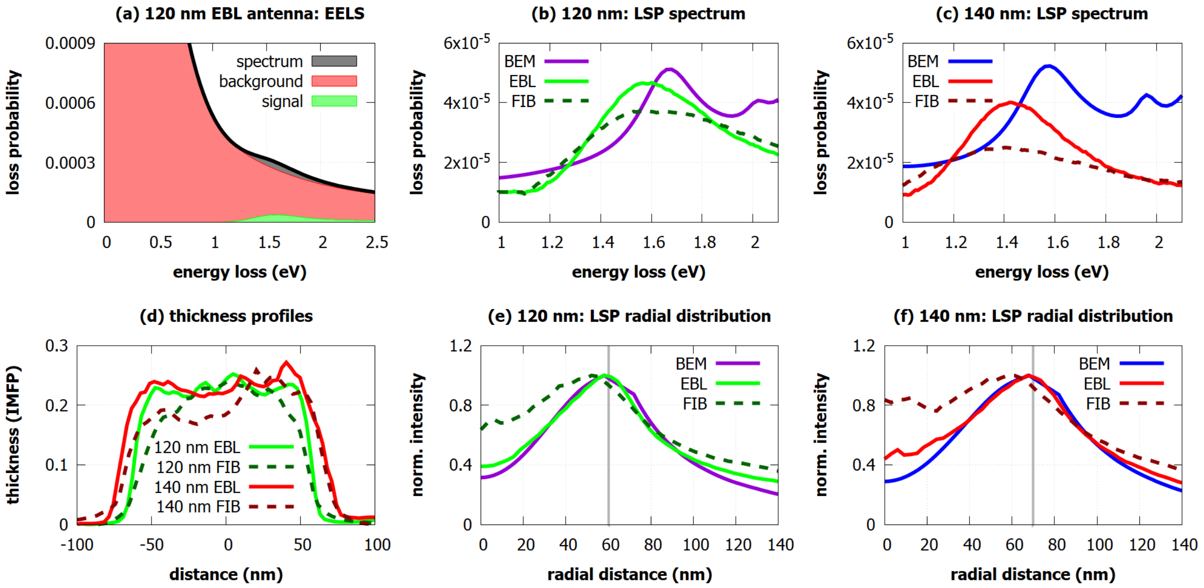

Figure 6.3: EELS measurement of LSP resonances. (a) Typical raw low-loss EEL spectrum (black) decomposed into background including zero-loss peak (red) and the signal corresponding to the LSP resonance (green) for the 120 nm EBL antenna. (b,c) Loss probability related to LSP measured by EELS in the EBL and the FIB antennas together with the calculated values obtained by BEM for 120 nm (b) and 140 nm (c) antennas. (d) Thickness profiles (thickness in units of inelastic mean free path, IMFP) of the antennas determined by EELS. We note that EBL antennas have slightly sharper edges. (e,f) The radial distribution of the LSP-related loss probability (at the energy of its maximum) for 120 nm (e) and 140 nm (f) antennas measured by EELS for EBL and FIB antennas and calculated by BEM. Antennas have their center at 0 nm and the edge of antennas is marked by the grey line.

LSP mode of 1.66 eV for 120 nm antennas and 1.59 eV for 140 nm antennas. Measured LSP resonance energy is (1.56 ± 0.09) eV for 120 nm EBL antenna, (1.62 ± 0.09) eV for 120 nm FIB antenna, (1.43 ± 0.09) eV for 140 nm EBL antenna, and (1.41 ± 0.09) eV for 140 nm FIB antenna. The measured energies are thus systematically red-shifted from the calculated energies, although the magnitude of the shift is rather minor and ranges between 0.04 eV and 0.18 eV. Such a red-shift can be attributed to the deviations of the actual antenna shape from the ideal disc, inhomogeneous thickness of antennas, modification of the dielectric function of gold due to grain boundaries and polycrystallinity of the antennas [45, 46], or effects induced by the contamination [83] and Ti adhesion layer [41, 42].

If we compare EBL and FIB antennas, we observe more intense peak for EBL antennas. Figure 6.2 shows the spatial distribution of the LSP resonance in the form of intensity maps at the energy of (1.60 ± 0.05) eV for 120 nm antennas and (1.40 ± 0.05) eV for 140 nm antennas. The radial dependences of the intensities averaged over the polar coordinate are shown in Figure 6.3e,f. The maximal intensity of LSP resonance is confined to sharp features on the edges of EBL antennas. In the case of FIB antennas, LSP resonance is less confined to the edges of the structures and the EEL intensity maps are blurred, which can be caused, for example, by thickness fluctuation or contamination.

Following the EELS measurements the chemical composition of the antennas including their possible contamination was analyzed by EDS, which enables detection of all elements heavier than Be in one measurement. We have detected and further focused on the following chemical elements: Si and N constituting the membrane, Au and Ti constituting the antenna and the adhesion layer, respectively, Ga that forms the ion beam in FIB and can be implanted into the sample, C and O as frequent contaminants. Spatial distribution of the intensity of characteristic X-ray radiation for these elements is shown in Figure 6.4 for both FIB and EBL antennas with the diameter of 140 nm together with the bright field TEM and high-angle annular dark field (HAADF) STEM micrographs. We distinguish in total three areas with different chemical composition, denoted as Area 1 to 3 in the following. Area 1 corresponds to the antenna and Areas 2 and 3 to its surrounding exposed and unexposed to the electron beam during EELS measurements, respectively. We note that the composition of Areas 2 and 3 is almost identical with the exception of carbon, which has a stronger presence in the Area 2 (exposed to the electron beam) in the case of FIB antenna (see the intense red square in Figure 6.4). The distribution of individual elements within each Area is homogeneous. The average relative atomic rate of each element for each Area is given in Table 6.1. As the thickness of different Areas is not identical, we note that the atomic rates between different Areas are not directly comparable but have to be rescaled to the same thickness.

Both Si and N exhibit almost identical X-ray intensity over all Areas for both FIB and EBL antennas. Slightly increased intensity of Si below the antennas (Area 1) is an artifact related to the secondary emission of X-rays in the silicon-based EDS detector associated with larger thickness and density of this Area. Average stoichiometry of the silicon nitride membrane (neglecting Area 1) reads $Si_3N_{2.0\pm0.6}$. Verification measurement by EELS resulted into average stoichiometry $Si_3N_{1.8\pm0.3}$ which is in a very good agreement with EDS. Gold is present only at the antennas (Area 1), underpinning reliability of both fabrication techniques. In general, EDS is not accurate enough to assess the thickness of the gold layer. It is nevertheless illustrative to provide a rough estimate. The atomic rate of Au is 0.18 ± 0.03 and 0.16 ± 0.03 in the EBL and FIB antenna, respectively. These values are equal within the experimental error. The atomic rates of Si and N are listed in Table 1. We now rescale the atomic rates to the volume rates using covalent radii of

Table 6.1: Chemical composition of the membranes with EBL and FIB antenna in atomic percents determined by EDS after the EELS measurement. The composition is averaged over one of three areas with homogeneous chemical compositions: Area 1 corresponds to the antenna, while Areas 2 and 3 corresponds to their surrounding exposed and unexposed to the electron beam during EELS measurements, respectively.

	EBL antenna			FIB antenna		
	Area 1	Area 2	Area 3	Area 1	Area 2	Area 3
Au	(18 ± 3) %	< 1 %	< 1 %	(16 ± 3) %	< 1 %	< 1 %
Ti	(4 ± 1) %	< 1 %	< 1 %	(4 ± 1) %	(2 ± 1) %	(2 ± 1) %
Si	(35 ± 5) %	(55 ± 5) %	(55 ± 5) %	(32 ± 5) %	(40 ± 5) %	(45 ± 5) %
N	(20 ± 3) %	(35 ± 5) %	(35 ± 5) %	(17 ± 3) %	(25 ± 5) %	(33 ± 5) %
C	(13 ± 3) %	(4 ± 2) %	(4 ± 2) %	(25 ± 5) %	(25 ± 5) %	(8 ± 3) %
O	(6 ± 2) %	(4 ± 2) %	(4 ± 2) %	(5 ± 2) %	(7 ± 2) %	(7 ± 2) %
Ga	< 1 %	< 1 %	< 1 %	< 1 %	(3 ± 1 %	(3 ± 1) %

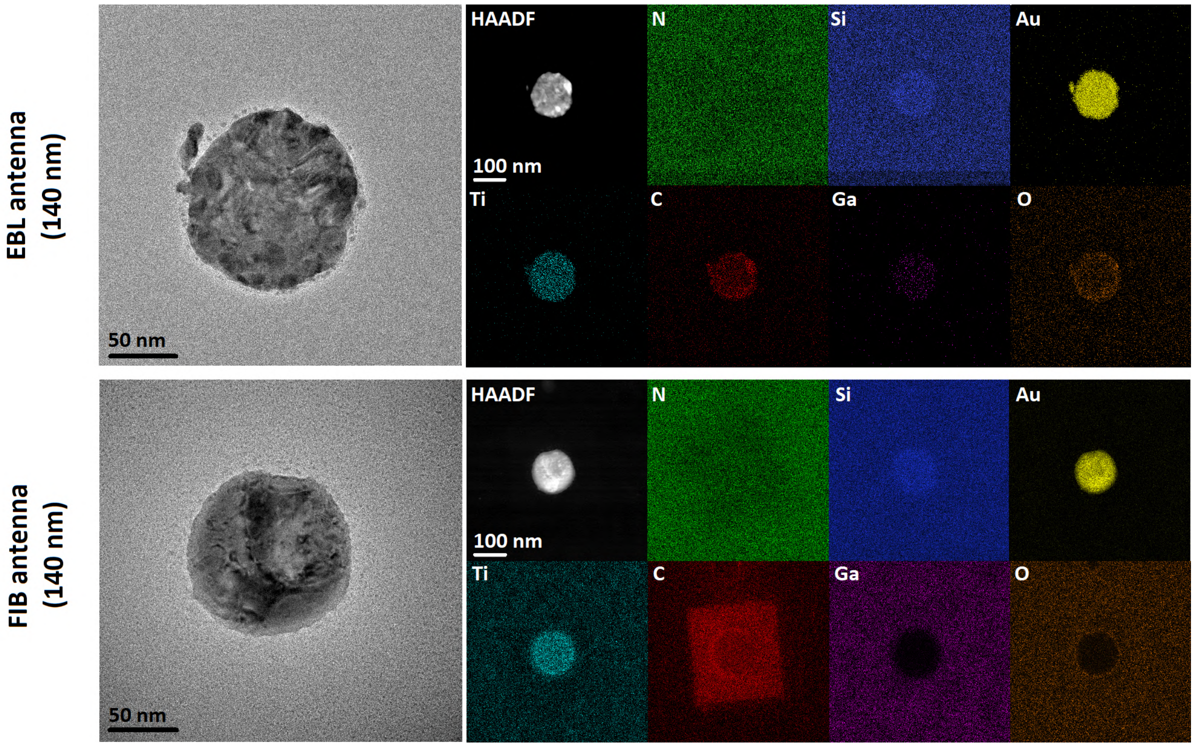

Figure 6.4: TEM micrographs and elemental maps showing chemical composition of 140 nm antennas. Left: TEM bright field micrographs of 140 nm EBL and FIB antennas. Right: STEM-HAADF image of the antennas presenting the distribution of heavy elements and spatial maps of element-specific X-ray intensity obtained from EDS for N, Si, Au, Ti, C, Ga, and O.

N, Si, and Au reading 71 pm, 116 pm, and 124 pm [218]. Considering the thickness of the silicon nitride membrane of 50 nm, we obtain rough estimates of the thickness of the gold layer equal to 28 nm and 27 nm for the EBL and FIB antenna, respectively, in a good agreement with the designed thickness of 25 nm and EELS measurements of 23 nm to 26 nm.

Ti is present in the Area 1 for the EBL antenna but in all Areas for the FIB antenna. Apparently, FIB lithography was unable to fully remove Ti from the desired Areas as the sputter rate of Ti is much smaller than that of Au. Estimated thickness of the Ti contamination layer is 1 nm to 2 nm. Ga ions have been implanted to Areas 2 and 3 (i.e. into the antenna surrounding) for the FIB antenna. The atomic rate of Ga reads 0.03 ± 0.01. Importantly, no Ga contamination is found directly above or inside antennas (i.e. in Area 1), suggesting its rather limited influence on the plasmonic response of the antennas.

Finally, C and O are present as usual contaminants due to several reasons. The EBL antenna indicates larger contamination in Area 1 (i.e., at the position of the antenna) where the atomic rate of C reads 0.13 ± 0.03 and the atomic rate of O is 0.06 ± 0.02. This is probably the result of incomplete resist removal during the development of lithographic pattern. The antenna surrounding (Areas 2 and 3) indicates low level of C and O contamination with the atomic rate of both elements of 0.04 ± 0.02. Such low levels of contamination refers to usual contamination of the sample when it is exposed to air. The FIB antenna indicates much higher C and O contamination. The sample has been contaminated by organic residues present in the FIB chamber. C is particularly strongly present in the areas exposed to the electron beam during the EELS measurement [213, 214] (Areas 1 and 2 corresponding to the intense red square in Figure 6.4) and its atomic rate reads 0.25 ± 0.05. Area 3 then exhibits the atomic rate of C of 0.08 ± 0.03 which is a higher value than for the EBL antenna. The atomic rate of O reads 0.05 ± 0.02 in Area 1 and 0.07 ± 0.02 in Areas 2 and 3 (i.e., in the antenna surroundings) which may indicate that Ti and Ga contaminants present in the surroundings are partially oxidized.

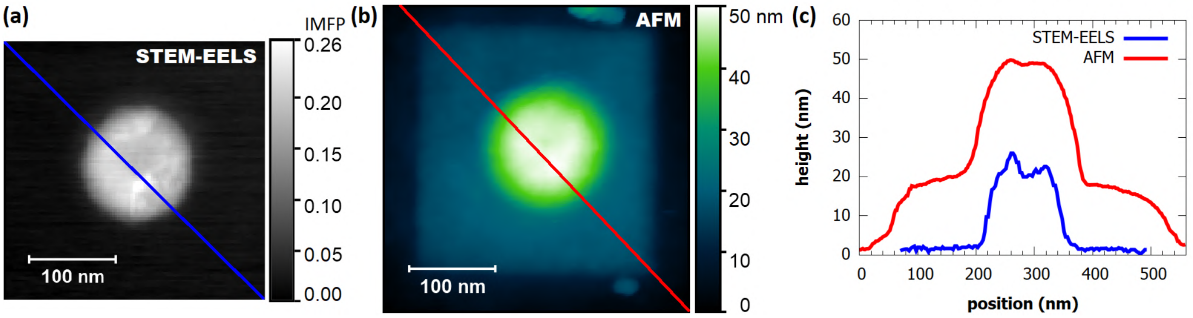

Figure 6.5: Thickness profile of a 140 nm FIB antenna and the hydrocarbon contamination on its surface. (a) Relative thickness (thickness in terms of IMFP) of the antenna retrieved by EELS. (b) Topography of the antenna including the hydrocarbon contamination measured by AFM. (c) Cross-sections of thickness profiles along the lines shown in (a) and (b). Relative thickness is recalculated to absolute thickness using the IMFP in gold of 113 nm. Blue line shows the thickness profile of the antenna determined by EELS, red line shows the thickness profile of the antenna and the contamination layer determined by AFM.

It is impossible to determine the thickness of hydrocarbon contamination layer on the FIB antennas using EELS because the contamination would further evolve during the measurement. Therefore, we have characterized surface topography of antennas by AFM measurement. Figure 6.5 compares the thickness of the 140 nm FIB antenna measured by EELS (assuming low hydrocarbon contamination) and surface topography measured by AFM after the EELS measurements (with hydrocarbon contamination being fully developed). The thickness of the hydrocarbon contamination layer is uniform over the whole area of EELS measurement (Areas 1 and 2) with an average thickness of (18 ± 5) nm determined as the height difference between Areas 2 and 3.

6.3 Conclusion

The choice of a preferred fabrication technique should also consider the time and potential risks of the fabrication process. FIB preparation is simple and more straightforward as no chemistry is used and fast for individual antennas or small series of antennas. Moreover, FIB lithography exerts low mechanical strain and thus enables processing of pristine materials with low adhesion to the substrate such as chemically grown single-crystalline gold flakes. EBL preparation provides generally antennas of a higher quality, but the lithographic process induces potential risks of damaging the sample as the wet chemistry is used. EBL is more time consuming than FIB if a small number of antennas is prepared, but much faster if a large array of antennas is fabricated. In such case, the volume of material to be removed by FIB is too large. Therefore, either of the techniques is suitable for a different class of targeted nanostructures. In general, when no specific issues apply, EBL shall be prioritized over FIB as it produces antennas with stronger plasmonic response and low contamination.

In conclusion, we have performed the comparative study of plasmonic antennas fabricated by EBL and FIB. We have demonstrated that the EBL antennas have better quality. First, they have rather homogeneous thickness profile with decent thickness fluctuation, and sharper edges. Second, they are cleaner, with a moderate contamination of organic origin evidenced by the presence of carbon and oxygen atoms with the total rate up to 20 %. On the other hand, plasmonic antennas fabricated by FIB lithography have slightly dull edges and exhibit pronounced thickness fluctuation. They are also strongly contaminated not only by organic contaminants forming a continuous layer of the thickness of about 18 nm, but also by residues of FIB milling including implanted milling ions and atoms of the titanium adhesion layer, possibly oxidized. In consequence, the plasmonic response of the antennas characterized by EELS is considerably stronger and slightly better localized for the antennas fabricated by EBL than for the antennas fabricated by FIB. To conclude, while both techniques are suitable for the fabrication of plasmonic antennas, EBL shall be prioritized over FIB lithography due to better quality of the resulting antennas.

7 Babinet's principle for disc-shaped plasmonic antennas

Babinet's principle relates the optical response of apertures in thin films and their complementary analogues – solid barriers or particles. Originating in the wave theory of light and analysis of diffraction, it has recently entered the field of plasmonics [28]. According to the Babinet's principle assuming the metallic layer as infinitesimally thin ideal conductor, localized surface plasmons in complementary particles and apertures have identical resonance energies and their near fields are closely linked: The electric field distribution with a specific in-plane polarization for an aperture corresponds to the magnetic field distribution with a perpendicular polarization for a particle [219]. However, the real metallic layer is not an ideal and infinitesimally thin conductor, therefore a perfect complementarity is not fully expected and some differences may arise from the imperfect complementarity. Moreover, some additional differences can be related to fabrication processes and experimental techniques involved in the characterization of the real structures.

7.1 Methods

To assess the theoretically predicted Babinet's complementarity, a set of gold disc-shaped antennas and complementary apertures in a gold layer, schematically shown in Figure 7.1, with various diameters were studied. Plasmonic structures were fabricated by FIB lithography of the 30 nm thick gold layer on the 3 nm thick titanium adhesion layer on a silicon nitride membrane. EEL and CL spectra have been measured for several disc-shaped plasmonic particles and apertures with diameters between 43 nm and 164 nm.

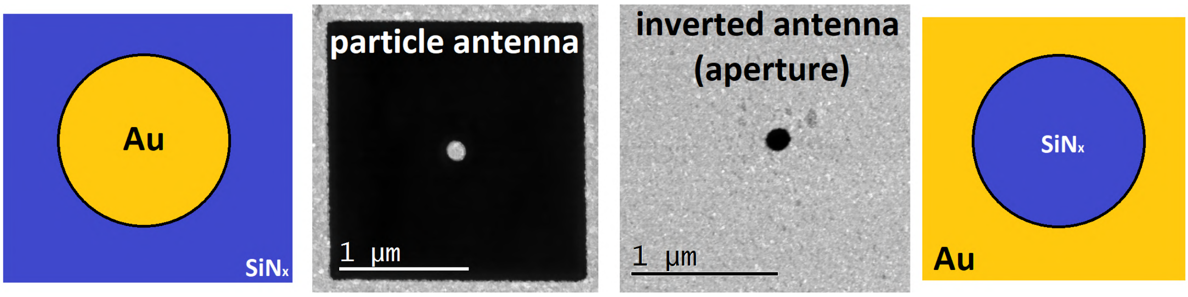

Figure 7.1: Schematic representation and dark field micrograph of a gold disc antenna and an aperture in the gold layer fabricated by FIB lithography.

Raw EEL spectra were processed by ZLP and background subtraction and normalized by dividing the spectra by the integral intensity of the ZLP with the interval of integration from −1 eV to 1 eV. A typical LSP related loss probability spectrum (for a disc with the diameter of 101 nm) is shown in Figure 7.2. The theory predicts two distinct LSP modes

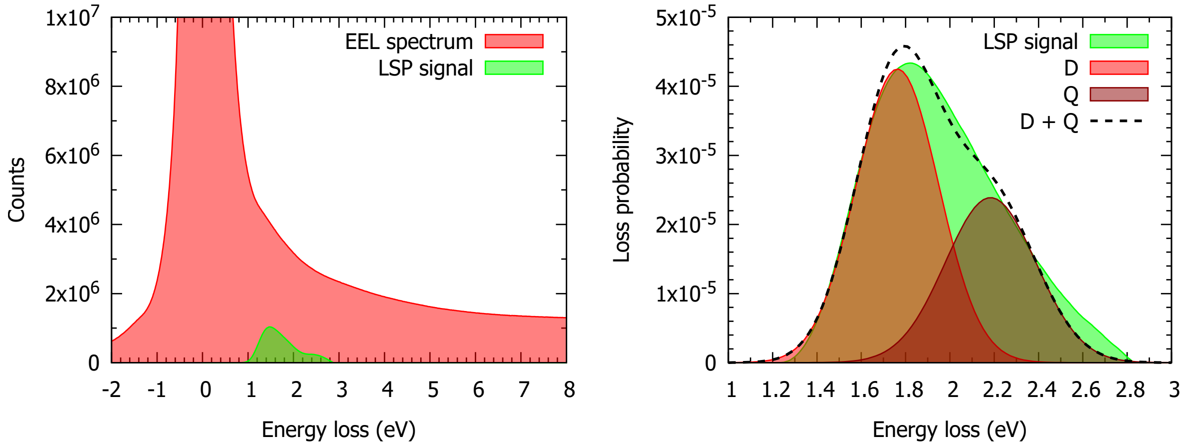

Figure 7.2: Processing of experimental EEL spectra. First, the EEL spectrum recorded for a disc with the diameter of 101 nm is decomposed into a zero-loss peak and background (red area), and LSP related response (green area). Second, the normalized LSP related EEL spectrum (green area) is decomposed into individual Gaussian peaks corresponding to the dipole mode (D) and the second peak corresponding to the quadrupole mode (Q) which is also influenced by the multimodal assembly.

(dipole and quadrupole), but the experimental EEL spectrum features only a single broad peak due to finite experimental resolution mostly limited by the energy distribution of the incident electron beam. Therefore, the experimental spectrum is further decomposed into individual peaks by sequential fitting of two Gaussians. The left side of the peak is fitted by a single Gaussian and the residual spectrum is processed in the same way. In this way, two peaks arising from the excitation of two distinct LSP modes or their superposition can be obtained. The first (lower energy) peak always represents the dipole LSP resonance. The second peak, however, cannot be always related with the quadrupole LSP resonance as it is contributed also by higher-order modes and corresponds thus to a mixture of the quadrupole mode with a multimodal assembly. Further, it is contributed by the bulk absorption that becomes important above 2 eV.

The loss probability maps were obtained by integration the total loss probability (including the ZLP and background) over the 0.1 eV wide energy window centered around the peak energy of the dipole mode and dividing this by the integral of total loss probability across the ZLP using an energy window from -1 eV to 1 eV. Such normalization is important to compensate the intensity differences caused by the different thickness of the parts of the sample covered and uncovered by gold.

7.2 Results

Experimental EEL and CL spectra of disc-shaped plasmonic antennas of different diameters excited near their edge are shown in Figure 7.3 and Figure 7.4, respectively. Within the EEL spectra it is possible to identify two peaks corresponding to the dipole LSP mode and the quadrupole mode mixed together with the multimodal assembly. In the CL spectra, just the dipole LSP mode is present as it is optically active, the higher modes have no net electric dipole moment and are thus optically dark. The peak energies of the detected LSP modes are displayed as functions of an effective wave number in a form of dispersion relations. The effective wave number is in the case of the dipole mode equal to the reciprocal antenna diameter, determined from ADF-STEM images. In the case of the

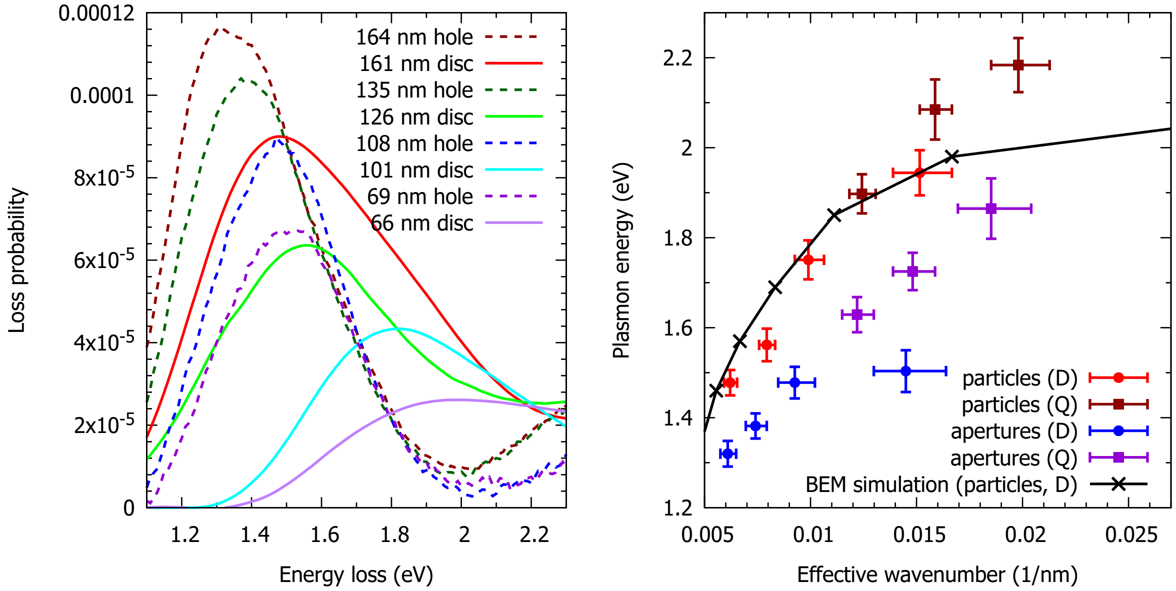

Figure 7.3: Measured EEL spectra of LSP resonance in gold nanodiscs and complementary apertures of different diameters (left) and the dispersion relation of measured LSP resonances by EELS (right). The peak energy is plotted as a function of the effective wavenumber, which corresponds to the reciprocal diameter in the case of the dipole mode or to the reciprocal value of the doubled diameter in the case of the quadrupole mode. To allow a brief comparison with the theory, BEM simulation of the dipole mode in gold nanodiscs is included.

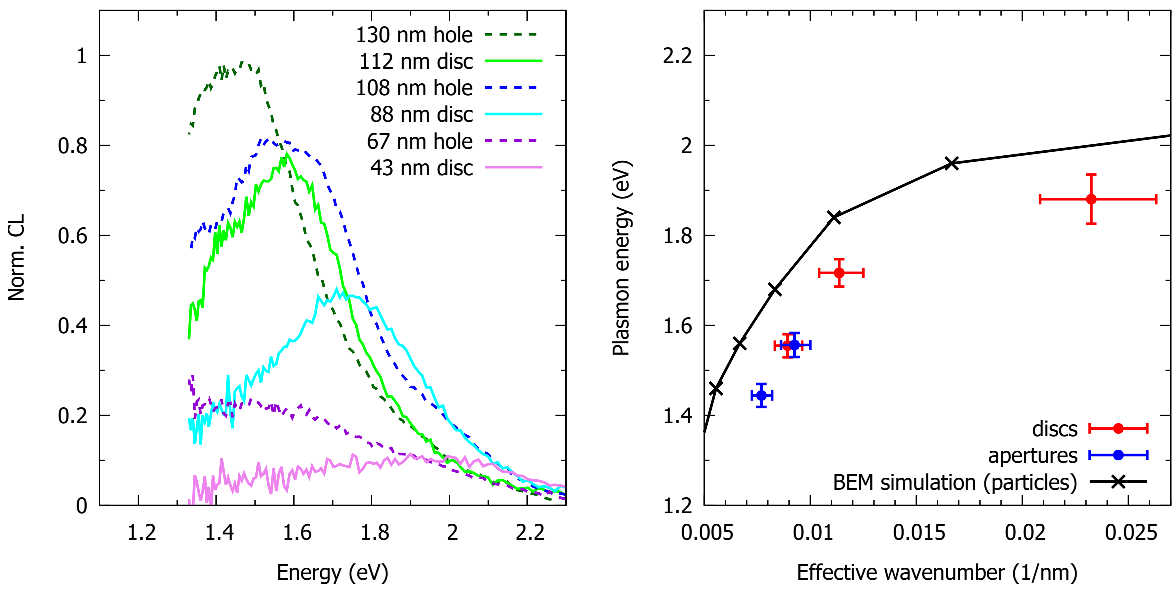

Figure 7.4: Measured CL spectra of LSP resonance in gold nanodiscs and complementary apertures of different diameters (left) and the dispersion relation of measured LSP resonances by CL (right). The peak energy is plotted as a function of the effective wavenumber, which corresponds to the reciprocal diameter. To allow a brief comparison with the theory, BEM simulation of the dipole mode in gold nanodiscs is included.

quadrupole mode, the effective wave number equals to the reciprocal value of the doubled antenna diameter. The error bars correspond to circles inscribed and circumscribed to the STEM micrographs of the antennas. The error bars of the energies include a standard error of the fit and a systematic error primarily related to the background subtraction and in the case of EELS to FWHM of the ZLP. To verify the measured results, a set of BEM simulations was computed. In simulations, the titanium adhesion layer was neglected, the dielectric function of gold was taken from Reference [206], and the dielectric constant of the silicon nitride membrane was set equal to 4 (in agreement with Reference [179]). The energy of the LSP dipole resonance in discs was calculated and is plotted in Figures 7.3 and 7.4 as the reference. Electron energy loss probability, the reference for EELS, and the radiative probability, the reference for CL, were evaluated separately. The energy of the dipole LSP resonance from simulations corresponds quite well to the measured value.

The energies of the dipole LSP mode determined by EELS and CL correspond to each other within the error bars. The agreement in the plasmon energy of disc and holes is excellent in the case of CL measurement. However in the case of EELS, a systematic redshift of apertures is observed. The only exception is the smallest aperture for which CL features no clear peak and the peak energy determined by EELS is strongly redshifted. The origin of this difference is at present not fully clear. Babinet's complementarity was therefore confirmed for the main LSP properties such as the resonance energies, but differences were found, for example, for the excitation efficiency as the measured response of the apertures is higher than for particles. This difference can be attributed to more efficient coupling of the apertures to the electromagnetic field of the relativistic electron or to the quality of fabricated antennas.

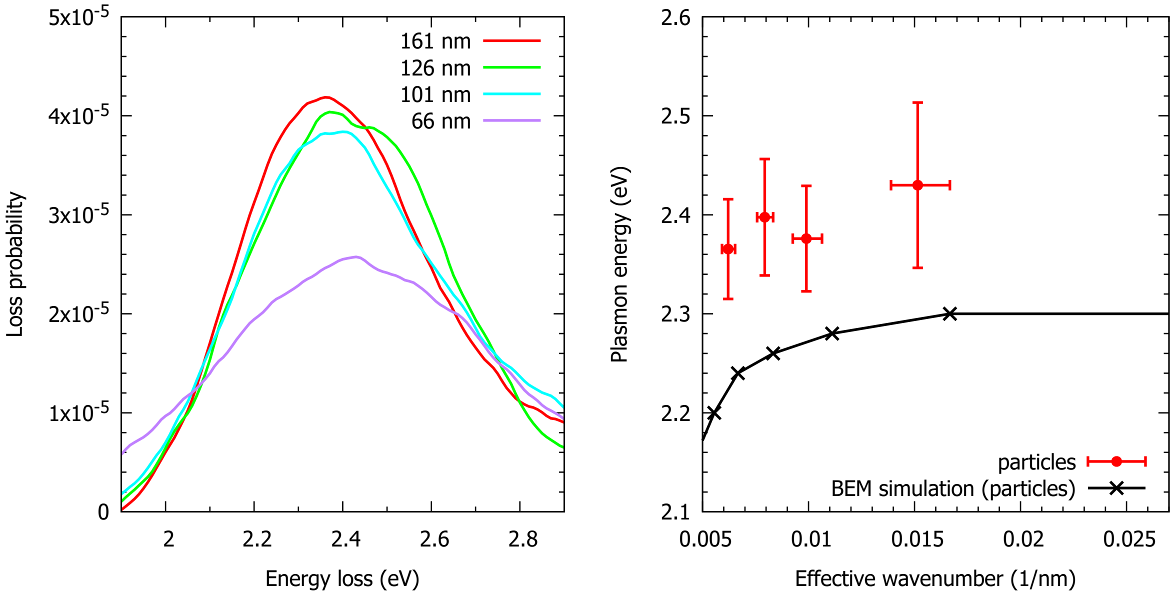

Figure 7.5: Measured EEL spectra of LSP resonance in gold nanodiscs corresponding to the breathing mode and its dispersion relation. In apertures, there was no breathing mode detected. The peak energy is plotted as a function of the effective wavenumber, which corresponds to the reciprocal diameter. To allow a brief comparison with the theory, BEM simulation of the breathing mode in gold nanodiscs is included.

In the case of discs, a radial breathing mode is expected to be detected while the electron beam is situated in the middle of the structure [175]. Experimental EEL spectra of disc-shaped plasmonic antennas of different diameters excited in their center are shown in Figure 7.5. The measured spectra consist of a single peak which corresponds to a mixture of the breathing LSP mode with a material absorption in gold which has a peak at 2.5 eV. Consequently, the dispersion relation indicates a systematic blueshift of the measured values. In the case of apertures, there was no breathing mode detected as the EEL spectra measured in the middle of the aperture did not contain any peak in the considered spectral region.

The spatial distribution of the dipole LSP mode was mapped by EELS only as CL suffered from the sample contamination during the long time spectrum image acquisition and the resulting CL maps can suffer from asymmetry of the collection mirrors. Figure 7.6 shows the dark field micrograph of a set of gold disc antennas and apertures followed by loss probability maps at the peak energy of the dipole mode (extracted from Figure 7.3) showing the spatial distribution of the dipole LSP resonance. Figure 7.7 than shows the spatial distribution of all LSP modes detected by EELS in the largest antennas.

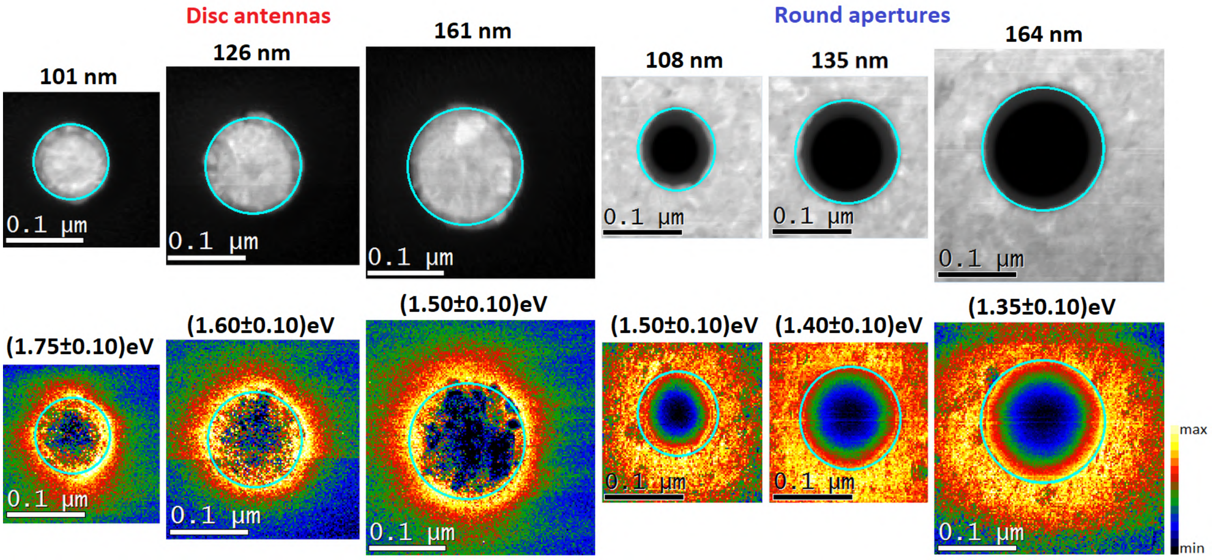

Figure 7.6: Dark field micrograph of a set of gold disc antennas and apertures followed by loss probability maps at the peak energy of the dipole mode (extracted from Figure 7.3) showing the spatial distribution of the dipole LSP resonance. The cyan circle denotes the edge of the antenna.

To allow for a quantitative comparison of rather noisy data and taking into account the radial symmetry, the intensity profile in the loss probability maps in Figure 7.7 was averaged over the angular coordinate. The radial dependencies are displayed in Figure 7.8. For both the dipole and the quadrupole mode the loss probability is the strongest nearby the edge of the antennas, peaking at the inner side of the boundary in the particle and at the outer side of the boundary in the aperture, it means, inside the metal near the edge of the structure. As it is expected, the quadrupole modes are more spatially confined than the dipole modes. The breathing mode in the disc has its maxima in the middle of the disc and its intensity decreases with the increasing distance. The important result is that the modes in apertures are considerably more extended and stronger (the loss probability is higher) than the modes in particles. This can be contributed by two effects. First, electric near field of the modes is less extended (exhibits faster asymptotic decay) than the magnetic near field in the particles, while the opposite holds (in line with Babinet's principle) in the apertures. In line with this finding the possibility to employ Babinet's principle for the imaging of the near magnetic field is revisited. It has been

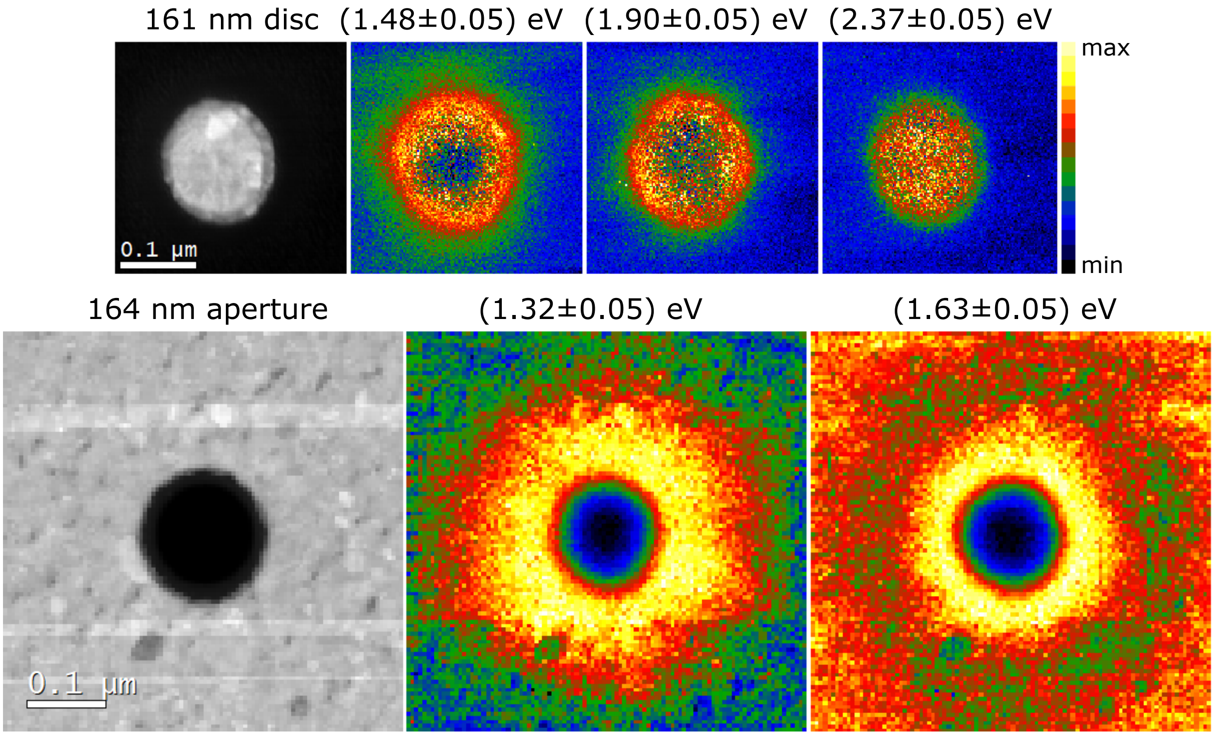

Figure 7.7: Dark field micrograph of gold disc antenna and aperture with the diameter of 161 nm and 164 nm, respectively, followed by loss probability maps showing the spatial distribution of the modes: the dipole (1.48 eV disc, 1.32 eV aperture), the quadrupole (1.90 eV disc, 1.63 eV aperture), and in the case of the disc also the breathing mode (2.37 eV).

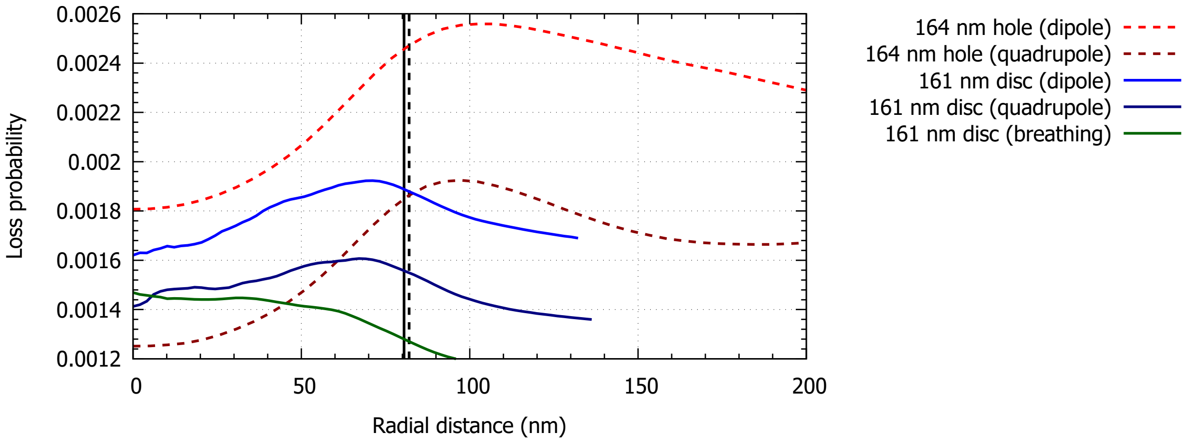

Figure 7.8: Radial dependence of the loss probability at the energy corresponding to the dipole, quadrupole, and breathing mode in the antenna and aperture with the diameter of 161 nm and 164 nm, respectively, obtained by rotational averaging of the intensity profile in loss probability maps in Figure 7.7. The black solid line denotes the radius of the disc and the black dashed line denotes the radius of the aperture, respectively.

proposed that difficult-to-access magnetic near field can be represented by the electric near field in the complementary structures [220, 221]. While this approach was proven successful in THz [220], the results presented in this Section indicate its rather limited applicability for the near infrared and visible spectral range and for using EELS as the magnetic imaging technique.

Differences for the excitation efficiency between particles and apertures can arise due to several reasons. In case of CL, a possible explanation might be a thermal quenching of the CL intensity due to local heating by the electron beam. The exposure time of CL measurements was relatively long (10 s per spectrum) and the beam was very intense (200 keV electron beam with the beam current about 30 nA), which may lead to the heating of the investigated structure. When an excited structure is heated, it relaxes into its ground state with a higher probability through nonradiative processes [125]. If the CL intensity is thermally quenched, the CL signal of the heated structure should decrease in time. One may expect that the gold layer around the apertures conducts the heat away more effectively than the pure membrane around the disc antennas, so the local temperature of the apertures is lower than the local temperature of the disc antennas. This would lead to higher thermal quenching for the disc antennas and to higher excitation efficiency for the apertures. To investigate this, an experiment with a time series of CL spectra with increasing exposure time was performed. Results measured on a disc with the diameter of approximately 80 nm and an aperture with the diameter of approximately 130 nm are summarized in Table 7.1. Note that the normalized counts for particle and aperture are very similar up to exposure time of 20 s and differ slightly for exposure times 30 s and 1 min. Therefore, thermal quenching does not play an important role during the presented CL experiments as the exposure time was 10 s per spectrum. The results summarized in Table 7.1 indicates that if thermal quenching due to different thermal conductivity of the material around the particle and aperture is present, it may play non-negligible role for measurements with acquisition time longer than 1 minute.

Table 7.1: Normalized CL intensity with respect to 1 s exposure time at the peak position for a gold disc shaped particle and aperture.

exposure time (s)	particle	aperture
1	1.00	1.00
2	2.08	2.37
5	5.22	5.77
10	10.87	10.24
20	20.74	22.50
30	29.53	35.05
60	54.41	68.18

7.3 Conclusion

In conclusion, solid and hollow disc-shaped plasmonic antennas exhibit Babinet's complementarity. We confirmed the qualitative validity of the Babinet's principle – both types of plasmonic antennas exhibit LSP resonances of the comparable energy and the related near fields have complementary spatial distribution. On the other hand, we have found quantitative differences. Most prominent differences have been found for the near fields represented by the spatial distribution of loss probability as the plasmonic response of apertures is generally stronger and less confined to the edge of the structure. From the practical point, the observed differences are rather minor. The validity of the Babinet's principle is relevant also for numerous applications. Babinet's complementarity allows to toggle between the magnetic and electric response, or between the reflection and transmission mode. While particles have to be supported by a substrate, substrate-less apertures self-supported by their frame can be fabricated. Apertures also offer better heat and charge management as the thin metallic film surrounding the apertures is usually better conductor than the substrate supporting the particles. This opens the possibility of choice between both types of plasmonic antennas depending on desired fabrication limitations and operational conditions in a wide field of applications.

8 Plasmonic antennas with electric and magnetic hot spots

This Chapter summarizes a study of nanostructures with electric and magnetic hot spots – areas of strong local enhancement of electric and magnetic field. Such effects are supported by bow-tie [210] and diabolo [211] antennas. Four types of plasmonic antennas are introduced applying bow-tie and diabolo duality together with the Babinet's principle [82]: bow-tie and diabolo antenna as plasmonic antennas in the form of particles, and inverted bow-tie and inverted diabolo antenna as plasmonic antennas in the form of apertures. These four types of plasmonic antennas are schematically shown in Figure 8.1. Plasmonic modes in nanoparticle dimers with conductive (diabolo or inverted bow-tie antennas) or insulating (bow-tie or inverted diabolo antennas) junction has been characterized in our study combining EELS, optical spectroscopy, and numerical simulations [80].

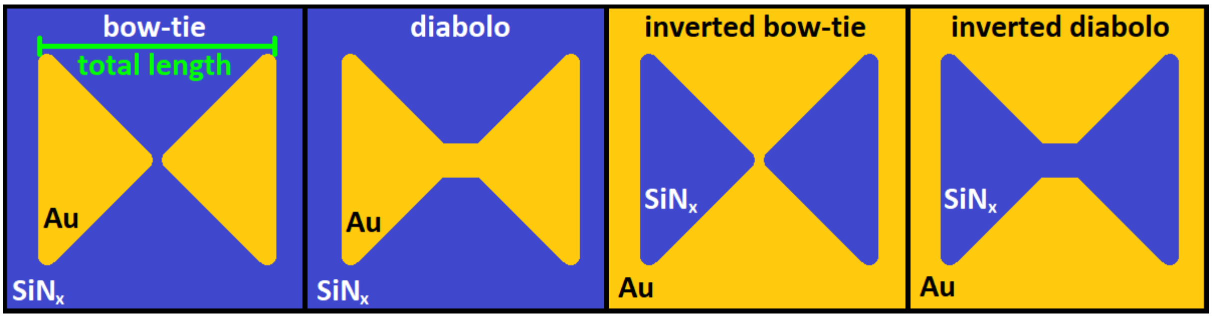

Figure 8.1: Schematic representation of bow-tie, diabolo, inverted bow-tie, and inverted diabolo antenna. The green bar denotes the total length of the antenna which is used as the characteristic parameter for all antennas.

8.1 Methods

Gold plasmonic antennas were fabricated on a 30 nm thick silicon nitride membrane by focused ion beam lithography of a deposited 30 nm thick polycrystalline gold layer. It should be noticed that no adhesion layer was used. Direct antennas were located in the middle of a metal-free square ranging according to their size between 1 µm × 1 µm and 4 µm × 4 µm, which is perfectly sufficient to prevent their interaction with the surrounding metallic frame. Inverted antennas were fabricated as isolated antennas with the distance between two nearby structures of at least 5 µm to prevent their collective interaction. Figure 8.1 shows the design of the bow-tie, diabolo, inverted bow-tie, and inverted diabolo plasmonic antennas. Particle antennas consist of two metallic wings and a bridge which is insulating for a bow-tie and metallic for a diabolo. For inverted structures, the metallic and the insulating parts are interchanged. The dimensions of the bridge are set to approximately 30 nm × 30 nm and the total length of the plasmonic antenna is varied. The wing angle is set to 90° which ensures the maximal complementarity of direct and inverted antennas. In this case, the area with gold and without gold is in the square with the edge corresponding to the total length of the antenna nearly the same. Bow-tie and inverted diabolo antennas concentrate charge and form electric hot spots while diabolo and inverted bow-tie antennas funnel current and form magnetic hot spots [82].

Plasmon resonances were characterized using EELS and partially CL. EELS measurements were performed with the TEM FEI Titan equipped with the GIF Quantum spectrometer operated in the monochromated scanning regime at 300 kV. The beam current was set to 0.4 nA and the FWHM of the ZLP was around 0.1 eV. The convergence angle was set to 10 mrad, the collection angle to 10.4 mrad, and the dispersion of the spectrometer to 0.01 eV/pixel. EELS spectrum images were recorded with the pixel size of 5 nm (except the largest structures where the pixel size was increased), while the number of pixels depended on the antenna size. Every pixel of the spectrum image consists of 30 cross-correlated and summed EEL spectra with the total pixel acquisition time around 25 ms. EEL spectra were integrated over several pixels around the positions of interest, background and zero-loss peak subtracted, and divided by the integral intensity of the whole spectrum to transform measured counts to a quantity proportional to the loss probability. EEL maps were obtained as energy-integrated intensity at the plasmon peak energy with the energy window of 0.1 eV divided by the integral intensity of the ZLP with the integration window from -0.5 eV to 0.5 eV. Such normalization is important to compensate the intensity differences caused by the different thickness of the parts of the sample covered and uncovered by gold. CL measurement was performed with the TEM FEI Tecnai F20 with the Gatan VULCAN spectrometer operated in the scanning regime at 200 kV. The beam current was set to 13 nA, the central wavelength was set to 800 nm which corresponds to the detectable energy range from 1.24 eV to 2.25 eV, the acquisition time was set to 2 s/pixel, and the CL signal was collected from both mirrors (upper and lower) together.

8.2 Bow-tie and inverted bow-tie antennas

A typical bow-tie antenna with the total length of 282 nm and a typical inverted bow-tie antenna with the total length of 300 nm are shown in Figure 8.2. The EEL spectra recorded at different positions reveal three distinct peaks. The nature of modes corresponding to these three peaks is revealed in the loss probability maps at peak energies shown in Figure 8.3.

The first peak in Figure 8.2 is detected at 1.23 eV in the case of bow-tie and at 1.08 eV in the case of inverted bow-tie, respectively. The spatial distribution of the loss probability at the energy of the first peak exhibits maxima in the corners of the bow-tie and therefore corresponds to a transverse dipole mode as it is oriented perpendicular to the total length of the structure. The transverse dipole mode is the lowest mode of this structure as the wing angle is set to 90° which implies the longest length of the metal piece of the bow-tie antenna in the transverse direction. It is a mixture of a bonding and an antiboding mode consisting of parallel and antiparallel alignment of the dipoles in both wings (Figure 8.3 shows the antibonding case). Their energy difference is in this case so low that they are not distinguishable by EELS. In the case of the inverted bow-tie, the energy of this mode is similar. However, the spatial distribution is rather different. From

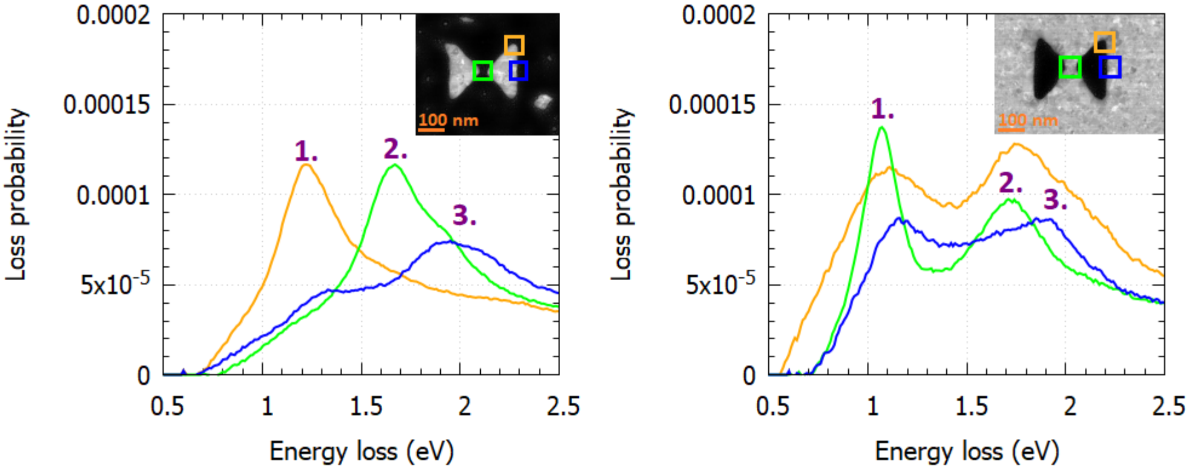

Figure 8.2: Background and ZLP subtracted normalized EEL spectra measured in the corner (orange), in the gap (green), and on the outer edge (blue) of the bow-tie (left) and the inverted bow-tie (right) antenna. The color squares in the insets indicate the areas where the respective spectra were collected. The first peak corresponds to the transverse dipole mode, the second one to the longitudinal dipole mode, and the third one to the edge mode. For better description of these modes, see Figure 8.3.

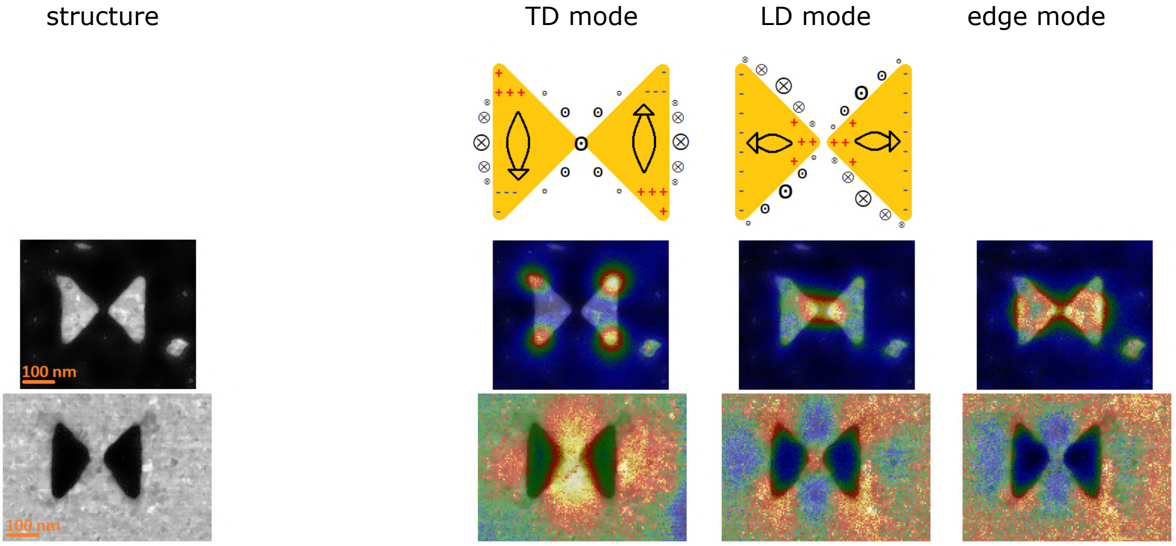

Figure 8.3: Schematic representation of detected plasmonic modes in the bow-tie antenna followed by experimental data corresponding to the transverse dipole (TD) mode, the longitudinal dipole (LD) mode, and the edge mode represented by loss probability maps at peak energies determined from Figure 8.2 placed over a shadow of the micrograph of the antenna shown in the left column. From the Gauss law it follows that the strongest out-of-plane electric field occurs just near the areas of the accumulated charge. Note that in the case of the particle antenna, the measured spatial distribution of the loss probability corresponds to the out-of-plane electric field distribution of the particle antenna, which is close to the accumulated charge distribution in the particle antenna. In the case of the inverted aperture antenna, it corresponds to the out-of-plane electric field distribution, which is close to out-of-plane magnetic field distribution related to the particle antenna.

the Gauss law it follows that the strongest out-of-plane electric field, detected by EELS, occurs just near the areas of an accumulated charge. Therefore, in the case of the particle bow-tie, the highest loss probability is detected in the corners of the structure, where the charge is accumulated. In the case of the inverted bow-tie (i.e. aperture), the Babinet's principle says that its out-of-plane electric field distribution is the same as the out-of-plane magnetic field distribution of the particle. As EELS detects the out-of-plane electric field, in principle, we indirectly detect the spatial distribution of out-of-plane magnetic field corresponding to the transverse dipole mode in the particle when inspecting the first peak in the case of the inverted bow-tie. This is perfectly confirmed by the schematic mode analysis presented in Figure 8.3.

The second peak in Figure 8.2 has the energy of 1.67 eV in the case of the bow-tie and 1.76 eV in the case of the inverted bow-tie, respectively. The spatial distribution of the loss probability at the energy of the second peak exhibits maximum in the gap of the bow-tie and therefore corresponds to a longitudinal dipole mode. Note that in our geometry the longitudinal length of each wing is shorter than their tranversal length. It is again a mixture of a bonding and an antibodning mode consisting of parallel and antiparallel alignment of the dipoles in both wings (Figure 8.3 shows the antibonding case). Their energy difference is also in this case so low that they are not distinguishable by EELS. In the case of the inverted bow-tie, the energy of this mode is similar. However, the spatial distribution is rather different and again corresponds to the spatial distribution of the out-of-plane magnetic field of this mode in the particle bow-tie.

The third peak in Figure 8.2 is detected at 1.95 eV in the case of the bow-tie and at 1.93 eV in the case of the inverted bow-tie, respectively. The spatial distribution of the loss probability at the energy of the third peak exhibits maxima in the middle of all edges of the bow-tie and corresponds to a higher order mode – the edge mode.

To explore the tunability of bow-tie and inverted bow-tie antennas, their size was scaled. A set of bow-tie and inverted bow-tie antennas with the total length from 200 nm to 1500 nm was studied by EELS. The investigation was focused on detection of the energy and spatial distribution of all three LSP modes (transverse dipole mode, longitudinal dipole mode, and edge mode) introduced in Figure 8.3. The energies of these modes are summarized in Table 8.1 for the bow-tie antennas and in Table 8.2 for the inverted bow-tie antennas. The energies of individual modes in particles and apertures are rather similar (for graphical visualization, see Figure 8.11). The transverse dipole mode is tunable in the respect size region from 0.3 eV to 1.4 eV and the longitudinal dipole mode is tunable in the respect size region from 0.6 eV to 2.0 eV in antennas under study. Consequently, both modes are easily tunable through the near-infrared and visible red spectral region. Moreover, larger antennas will support LSP resonances tunable in infrared region at energies which are hardly accessible by electron beam spectroscopy.

Spatial distributions of all three LSP modes is shown in Figure 8.4 for bow-tie antennas and in Figure 8.5 for inverted bow-tie antennas. These experimental maps suffer from two pitfalls. First, LSP modes at energies lower than 0.5 eV are overlapping with a non-negligible intensity from the ZLP, which leads to a poor signal-to-background ratio of EELS below 0.5 eV. Therefore, the maps corresponding to the modes with the energy below 0.5 eV are not shown. Second, these experimental maps show the loss probability integrated over the 0.1 eV interval at the peak energy of the respect LSP mode. Therefore, if the structure supports two different LSP modes at a similar energy, the experimental map detects the summed loss probability of all overlapping modes in the respect energy interval. Note that such loss probability maps are presented. To show the clear distribution of the modes it would be necessary to fit all spectra by eigenmodes functions, which would

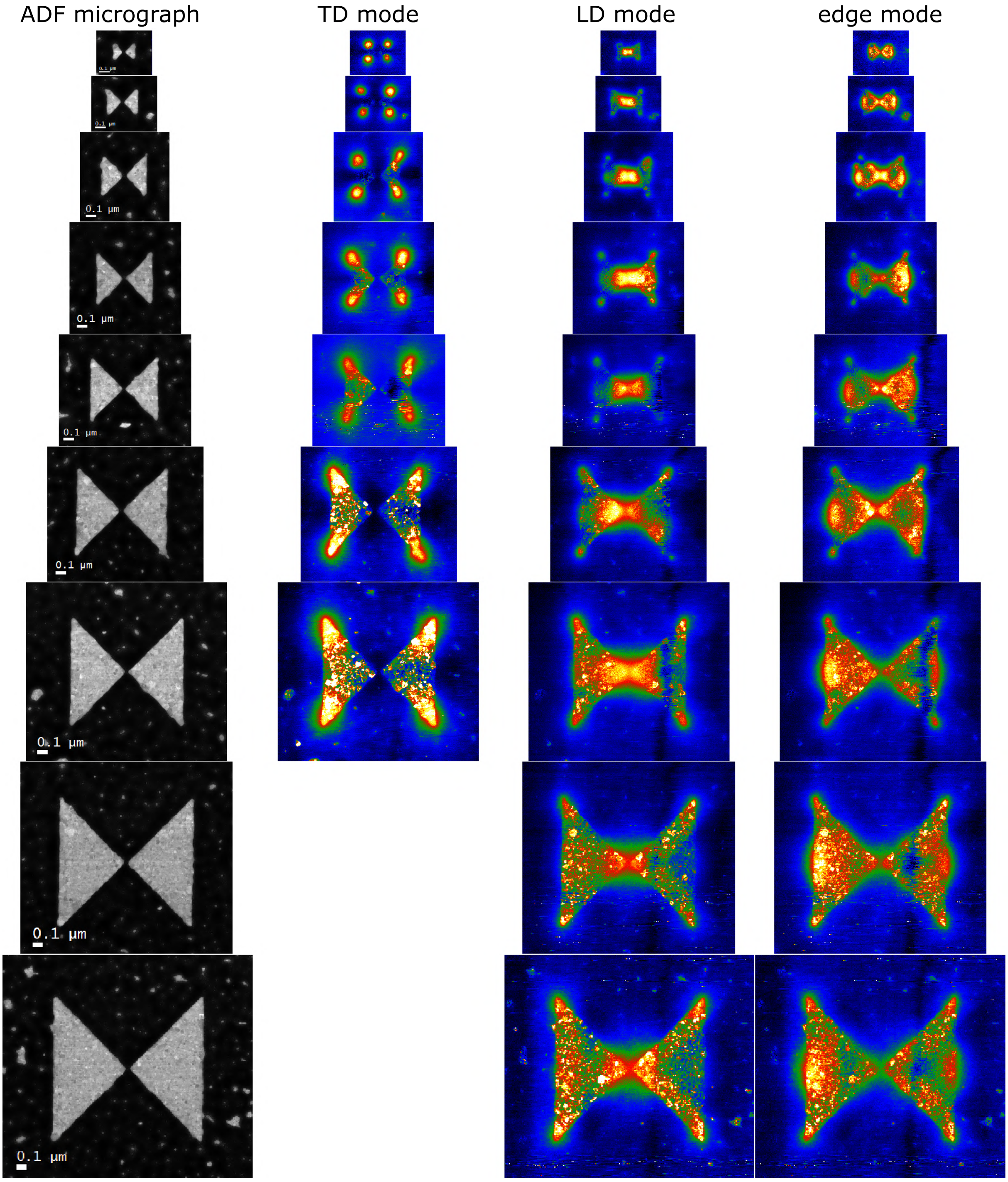

Figure 8.4: Annular dark field STEM micrographs of a set of gold bow-tie antennas followed by loss probability maps at the energy of the transverse dipole (TD) mode, longitudinal dipole (LD) mode, and edge mode listed in Table 8.1. As the experimental loss probability maps gives good results just at energies above 0.5 eV, the maps corresponding to the modes at lower energies are excluded.

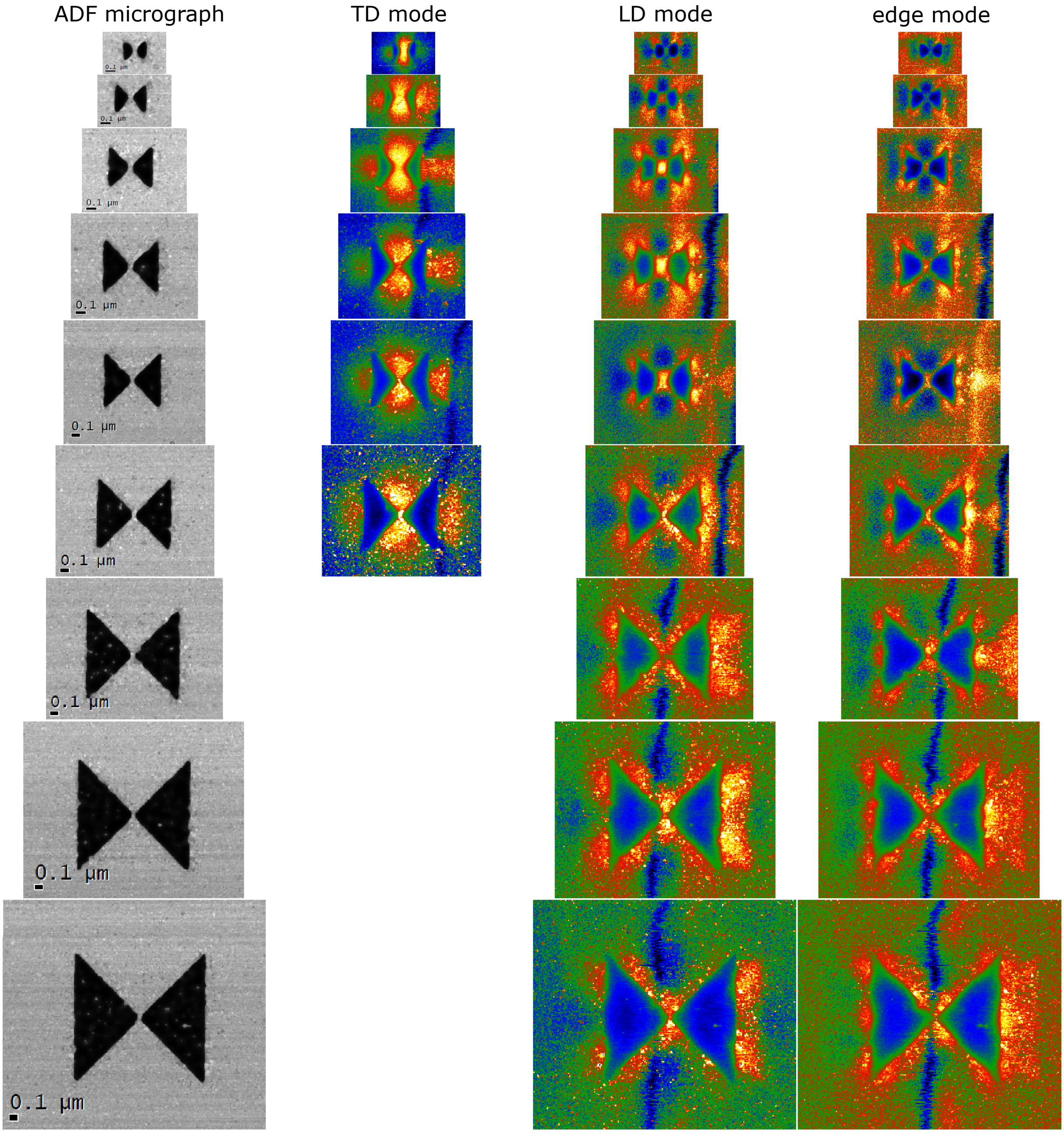

Figure 8.5: Annular dark field STEM micrographs of a set of gold inverted bow-tie antennas followed by loss probability maps at the peak energy of the transverse dipole (TD) mode, longitudinal dipole (LD) mode, and edge mode listed in Table 8.2. As the experimental loss probability maps gives good results just at energies above 0.5 eV, the maps corresponding to the modes at lower energies are excluded.

Table 8.1: Bow-tie antennas: total length of the antenna followed by the energy of the peak corresponding to the transverse dipole (TD) mode, the longitudinal dipole (LD) mode, and the edge (E) mode.

total length (nm)	TD (eV)	LD (eV)	E (eV)
200	1.41	1.85	2.12
282	1.23	1.67	1.95
419	0.97	1.44	1.62
520	0.79	1.23	1.44
610	0.69	1.08	1.27
825	0.58	0.90	1.08
1030	0.50	0.77	0.93
1275	0.45	0.67	0.81
1490	0.35	0.60	0.72

Table 8.2: Inverted bow-tie antennas: total length of the antenna followed by the energy of the peak corresponding to the transverse dipole (TD) mode, the longitudinal dipole (LD) mode, and the edge mode.

total length (nm)	TD (eV)	LD (eV)	Q (eV)
217	1.33	1.95	2.11
300	1.08	1.76	1.93
440	0.87	1.56	1.73
536	0.76	1.38	1.61
652	0.66	1.29	1.53
860	0.56	0.96	1.36
1054	0.45	0.82	1.16
1296	0.39	0.72	0.99
1500	0.35	0.67	0.93

be a rather complicated postprocessing of the experimental data, and to plot the spatial distribution of fitted amplitudes of these functions. It should be also noticed that the vertical blue or yellow line going through the maps is an experimental artifact connected with an insufficiently regenerated CCD camera while recording the EEL spectra.

In the case of bow-tie antennas, the spatial distribution of the modes is the same through all the structures. However, the edge mode maps in the larger structures are not as clear as in the case of smaller structures due to overlapping with other modes. In the case of inverted bow-tie antennas, the spatial distribution of the modes is similar through all the structures. In the smallest apertures, the longitudinal dipole mode and the edge mode are not well distinguishable from each other. In the larger apertures, the spatial maps are different as the loss probability at the energy of the edge mode has maxima in the middle of outer edges of apertures whereas the loss probability at the energy of the longitudinal dipole mode has minima there.

8.3 Diabolo and inverted diabolo antennas

A typical diabolo antenna with the total length of 300 nm and a typical inverted diabolo antenna with the total length of 280 nm are shown in Figure 8.6. EEL spectra recorded at different positions reveal four distinct peaks. The nature of modes corresponding to

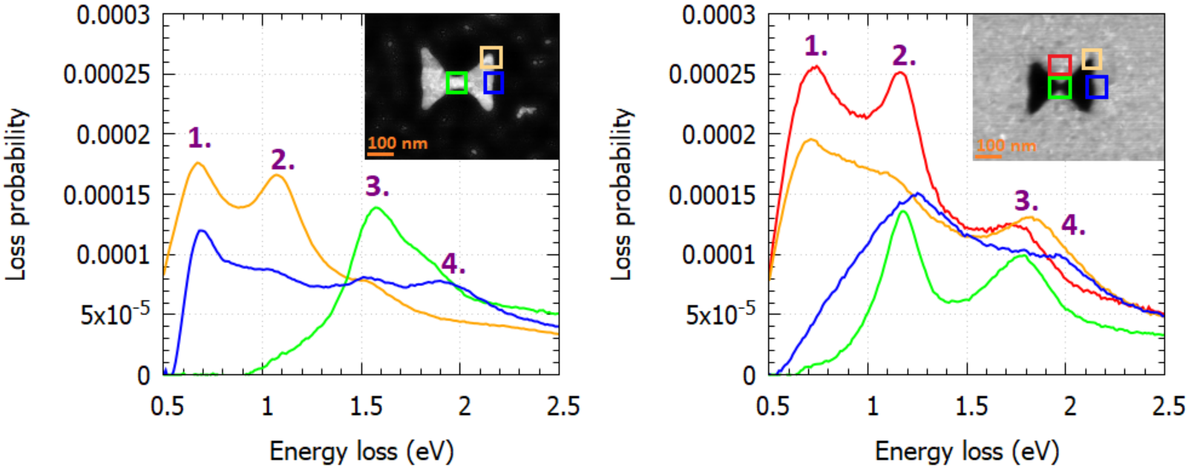

Figure 8.6: Background and ZLP subtracted normalized EEL spectra measured in the corner (orange), in the neck (green), next to the neck (red), and on the outer edge (blue) of the diabolo (left) and the inverted diabolo (right) antenna. The color squares in the insets indicate the areas where the respective spectra were collected. The first peak corresponds to the longitudinal bonding dipole mode, the second one to the transverse dipole mode, the third one to the longitudinal antibonding dipole mode, and the fourth one to the edge mode. For better description of these modes see Figure 8.7.

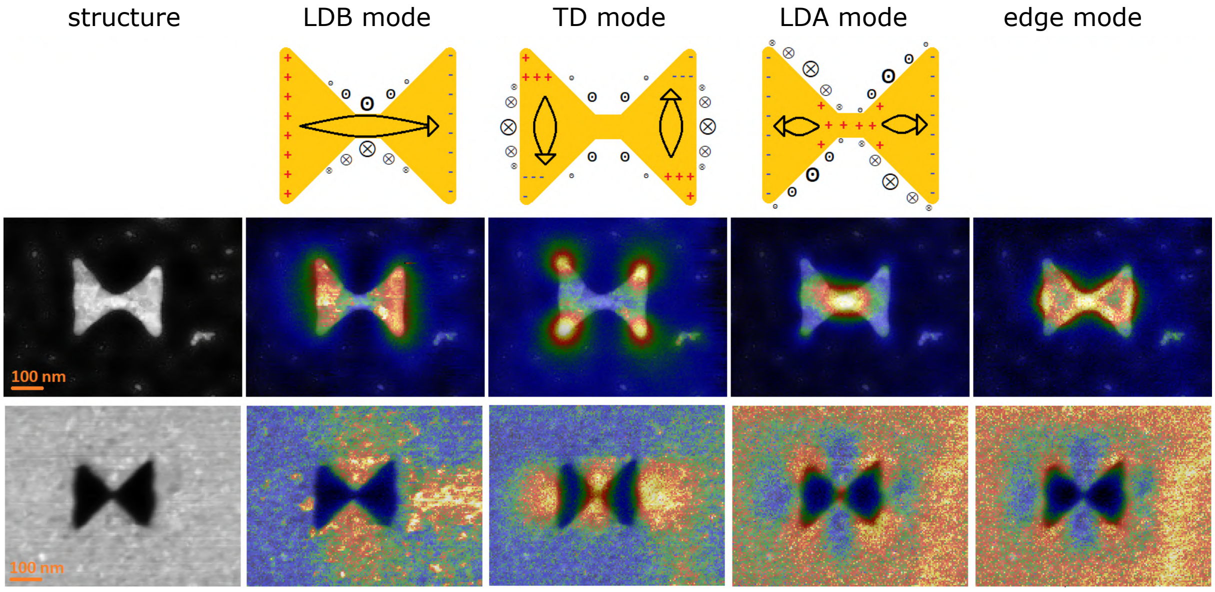

Figure 8.7: Schematic representation of detected plasmonic modes in the diabolo antenna followed by experimental data corresponding to the longitudinal bonding dipole (LDB) mode, the transverse dipole (TD) mode, the longitudinal antibonding dipole (LDA) mode, and the edge mode represented by the loss probability maps at the peak energies determined from Figure 8.6 placed over a shadow of the micrograph of the antenna shown in the left column. From the Gauss law it follows that the strongest out-of-plane electric field occurs just near the areas of the accumulated charge. Note that in the case of the particle antenna, the measured spatial distribution of the loss probability corresponds to the out-of-plane electric field distribution of the particle antenna, which is close to the accumulated charge distribution in the particle antenna. In the case of the inverted aperture antenna, it corresponds to out-of-plane electric field distribution of the aperture antenna, which is close to the out-of-plane magnetic field distribution of the particle antenna.

these four peaks is revealed in loss probability maps at peak energies shown in Figure 8.7.

The first peak in Figure 8.6 is detected at 0.69 eV in the case of diabolo and at 0.73 eV in the case of inverted diabolo, respectively. The spatial distribution of the loss probability at the energy of the first peak exhibits maxima at the outer edges of the diabolo and therefore corresponds to a longitudinal dipole mode. If the diabolo is considered as a coupled structure consisting of two wings connected by a bridge, this mode corresponds to the longitudinal bonding dipole mode as the dipoles in both wings are oriented parallel and acts together to form the basic mode of the diabolo antenna. In the case of the inverted diabolo, the energy of this mode is similar. However, the spatial distribution is rather different. From the Gauss law it follows that the strongest out-of-plane electric field, detected by EELS, occurs just near the areas of the accumulated charge. Therefore, in the case of the particle bow-tie, the highest loss probability is detected in the corners of the structure, where the charge is accumulated. In the case of the inverted bow-tie (i.e. aperture), Babinet's principle says that the out-of-plane magnetic field of the particle has the same spatial distribution as the out-of-plane electric field of the aperture. As EELS detects the out-of-plane electric field, in principle, we detect the spatial distribution of the out-of-plane magnetic field corresponding to the longitudinal dipole mode in the particle when inspecting the first peak in the case of the inverted diabolo. This is perfectly confirmed by the schematic mode analysis presented in Figure 8.7. Note that we observe the same effect as in the case of the bow-tie and the inverted bow-tie discussed in Section 8.2.

The second peak in Figure 8.6 is detected at 1.09 eV in the case of the diabolo and at 1.18 eV in the case of the inverted diabolo, respectively. The spatial distribution of the loss probability at the energy of the second peak exhibits maxima in the corners of the diabolo antenna and therefore corresponds to a transverse dipole mode. It is a mixture of the bonding and the antibonding mode consisting of a parallel and an antiparallel alignment of the dipoles in both wings (Figure 8.7 shows the antibonding case). Their energy difference is in this case so low that they are not distinguishable by EELS. In the case of the inverted bow-tie, the energy of this mode is similar. The spatial distribution is rather different and corresponds to the spatial distribution of the out-of-plane magnetic field of this mode in the diabolo as expected (see Figure 8.7).

The third peak in Figure 8.6 has the energy of 1.58 eV in the case of diabolo and 1.83 eV in the case of inverted diabolo. The spatial distribution of the loss probability at the energy of the third peak exhibits a maximum in the neck of the diabolo and therefore corresponds to a longitudinal antibonding dipole mode where the dipoles in two wings are oriented antiparallel. Note that contrariwise to the bow-tie, the longitudinal bonding dipole mode and the longitudinal antibonding dipole mode are in the case of the diabolo well separated in energy and easily distinguished by EELS.

The fourth peak in Figure 8.6 is detected at 1.95 eV in the case of the diabolo and at 2.00 eV in the case of the inverted diabolo. The spatial distribution of the loss probability at the energy of the fourth peak exhibitss maxima in the middle of all edges of the diabolo and corresponds to a higher order mode – the edge mode.

To explore the tunability of diabolo and inverted diabolo antennas, their size was scaled. A set of diabolo and inverted diabolo antennas with the total length ranging from 200 nm to 750 nm was studied by EELS. The shortest length is the same as in the case of bow-tie antennas as even smaller structures would be rather difficult to fabricate. The longest length is half of the bow-tie longest length. Note that due to the presence of the conductive bridge the effective length in the longitudinal direction is different for the diabolo and bow-tie antenna. In the case of the diabolo antennas, it corresponds to

Table 8.3: Diabolo antennas: total length of the antenna followed by the energy of the peak corresponding to the longitudinal bonding dipole (LDB) mode, the transverse dipole (TD) mode, the longitudinal antibonding dipole (LDA) mode, and the edge (E) mode.

total length (nm)	LDB (eV)	TD (eV)	LDA (eV)	E (eV)
190	0.97	1.52	1.85	2.13
255	0.77	1.30	1.71	2.05
300	0.69	1.09	1.58	1.95
500	0.45	0.81	1.24	1.51
600	0.39	0.72	1.13	1.35
710	0.36	0.66	0.98	1.07

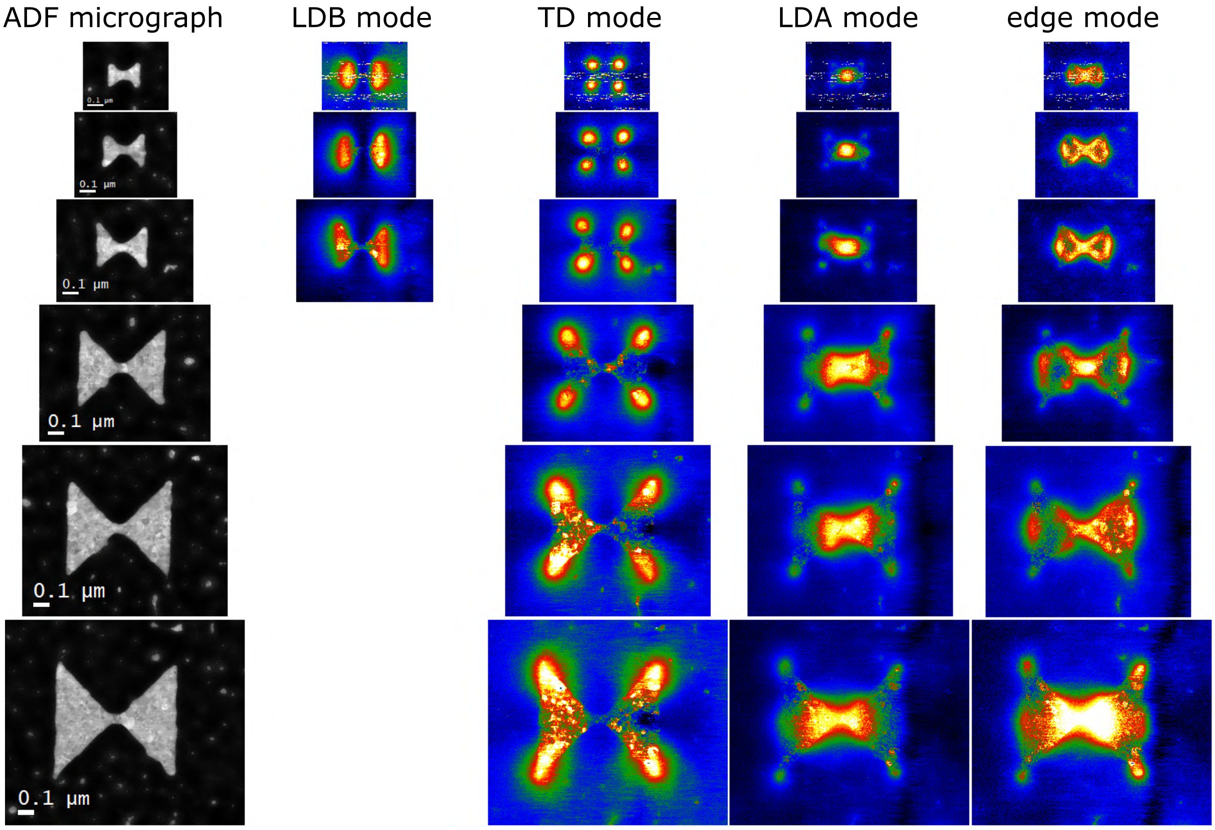

Figure 8.8: Annular dark field STEM micrographs of a set of gold diabolo antennas followed by loss probability maps at the peak energy of the longitudinal bonding dipole (LDB) mode, the transverse dipole (TD) mode, the longitudinal antibonding dipole (LDA) mode, and the edge mode listed in Table 8.3. As the experimental loss probability maps gives good results just at energies above 0.5 eV, the maps corresponding to the modes at lower energies are excluded.

Table 8.4: Inverted diabolo antennas: total length of the antenna followed by the energy of the peak corresponding to the longitudinal bonding dipole (LDB) mode, the transverse dipole (TD) mode, the longitudinal antibonding dipole (LDA) mode, and the edge (E) mode.

total length (nm)	LDB (eV)	TD (eV)	LDA (eV)	E (eV)
220	0.90	1.38	1.95	2.07
280	0.73	1.18	1.83	2.00
320	0.68	1.07	1.78	1.91
430	0.48	0.88	1.57	1.75
530	0.43	0.75	1.41	1.64
630	0.39	0.66	1.26	1.48
770	0.35	0.59	1.15	1.40

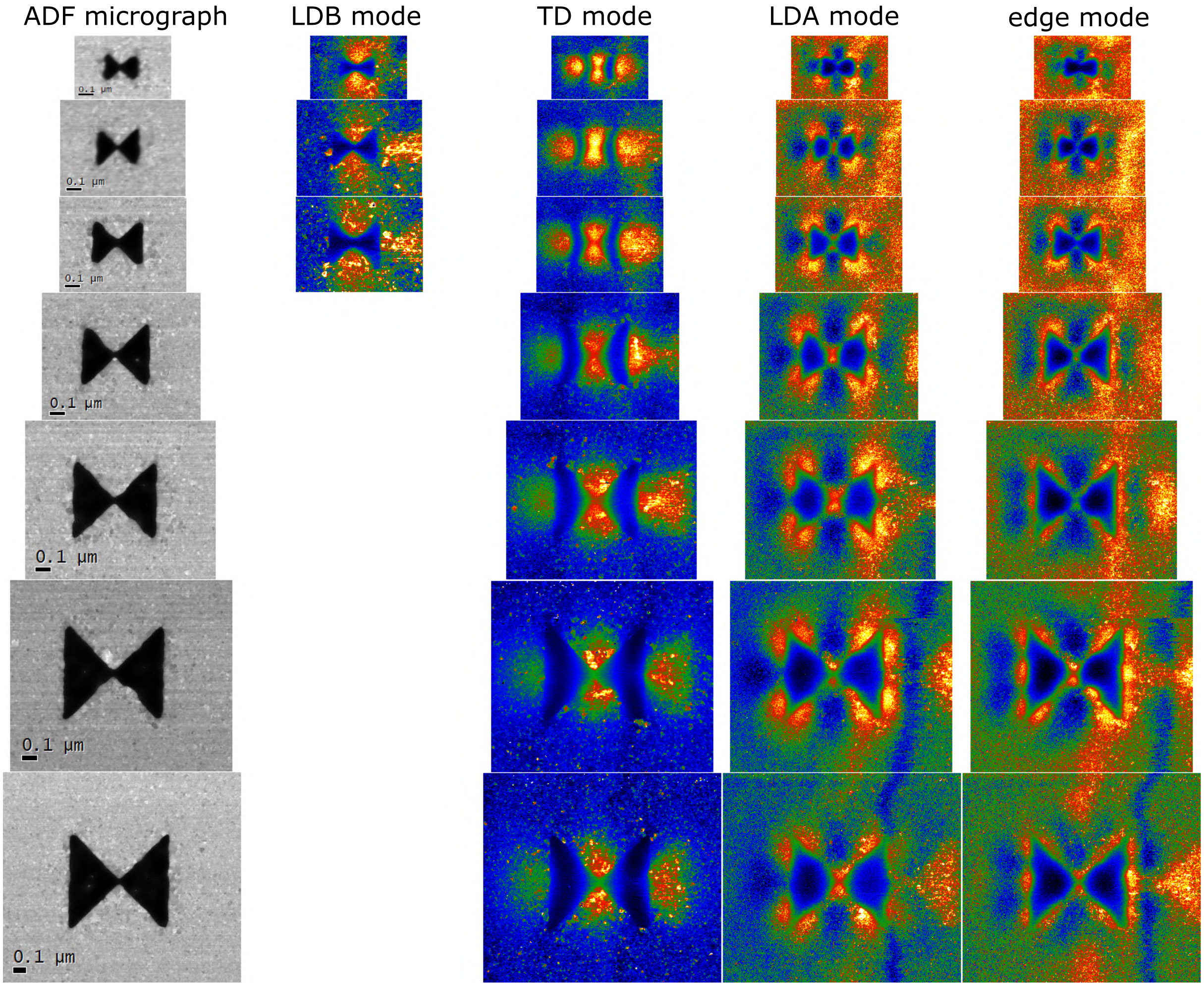

Figure 8.9: Annular dark field STEM micrographs of a set of gold inverted diabolo antennas followed by loss probability maps at the peak energy of the longitudinal bonding dipole (LDB) mode, transverse dipole (TD) mode, longitudinal antibonding dipole (LDA) mode, and the edge mode listed in Table 8.4. As the experimental loss probability maps gives good results just at energies above 0.5 eV, the maps corresponding to the modes at lower energies are excluded..

the total length of the diabolo, whereas the effective length of the bow-tie corresponds to the half of the total length of the bow-tie. The investigation was focused on detection of the energy and spatial distribution of all four LSP modes (longitudinal bonding dipole mode, transverse dipole mode, longitudinal antibonding dipole mode, and edge mode) introduced in Figure 8.7. The energies of these modes are summarized in Table 8.3 for the diabolo antennas and in Table 8.4 for the inverted diabolo antennas. The energies of the individual modes in both the diabolo and inverted diabolo antennas of the same size are rather similar (for graphical visualization, see Figure 8.11). For the considered range of dimensions, the energy of the longitudinal bonding dipole mode is tunable from 0.3 eV to 1.0 eV, the transverse dipole mode is tunable from 0.6 eV to 1.5 eV, and the longitudinal antibonding dipole mode is tunable from 1.0 eV to 2.0 eV. Consequently, all the three modes are easily tunable through the near-infrared spectral region while the longitudinal antibonding dipole mode is tunable in the visible red spectral region, too.

Spatial distribution of all the four LSP modes is shown in Figure 8.8 for diabolo antennas and in Figure 8.9 for inverted diabolo antennas. Loss probability maps corresponding to the modes at energies below 0.5 eV are excluded. In the case of diabolo antennas, the spatial distribution of the modes is the same for all structures. However, in the larger structures the edge maps are influenced by a spectral overlap with the longitudinal dipole antibonding mode. In the case of inverted diabolo antennas, the spatial distribution of the modes is similar for all structures. The longitudinal dipole antibonding mode and edge mode are not well distinguishable from each other in smaller apertures as they are close to each other in energy and the edge mode has lower loss probability (see the height of the third and the fourth peak in Figure 8.6). In larger apertures, the spatial maps are different as the edge mode has maxima in the middle of outer edges of apertures whereas the longitudinal dipole mode has minima there.

8.4 Comparison of all four types of the antennas

Figure 8.10 compares the spatial maps of the loss probability for all detected LSP modes. The size of the antennas is identical with respect to the fabrication uncertainty: the total length varies between 280 nm and 300 nm. The duality between bow-tie and diabolo antennas is clearly observed. The modes that do not involve charge transfer through the bridge of the antenna (transverse dipole, longitudinal dipole antibonding or longitudinal dipole, and edge) have identical spatial distribution of the loss probability in both direct and inverted structures. They also have similar mode energies. The only difference is the longitudinal dipole bonding mode that includes charge transfer through the conductive bridge of diabolo antennas. Note that the diabolo antenna has the longitudinal dipole bonding mode well separated from the longitudinal dipole antibonding mode, whereas in the case of a bow-tie antenna these two modes are overlapping with each other. The same duality holds for the direct antennas as well as for the inverted antennas: the inverted bow-tie and inverted diabolo pair.

Babinet's complementarity, which was already discussed in the previous Sections, is clearly visible in Figure 8.10, too. Figure 8.11 compares the energy of all detected LSP modes in all the four types of the antennas in the form of dispersion relations, where the plasmon energy is plotted as a function of the reciprocal total length of the antenna. This easily allows to compare the plasmon energy of modes in the antennas of a different total length. It can be seen, that the corresponding modes in all the four types of the antennas have the same energy. The best agreement is observed for the transverse dipole mode.

To sum up, the corresponding modes in the direct and inverted antennas, despite having identical energy, strongly differ in the spatial distribution of measured loss probability or the out-of-plane electric near fields.

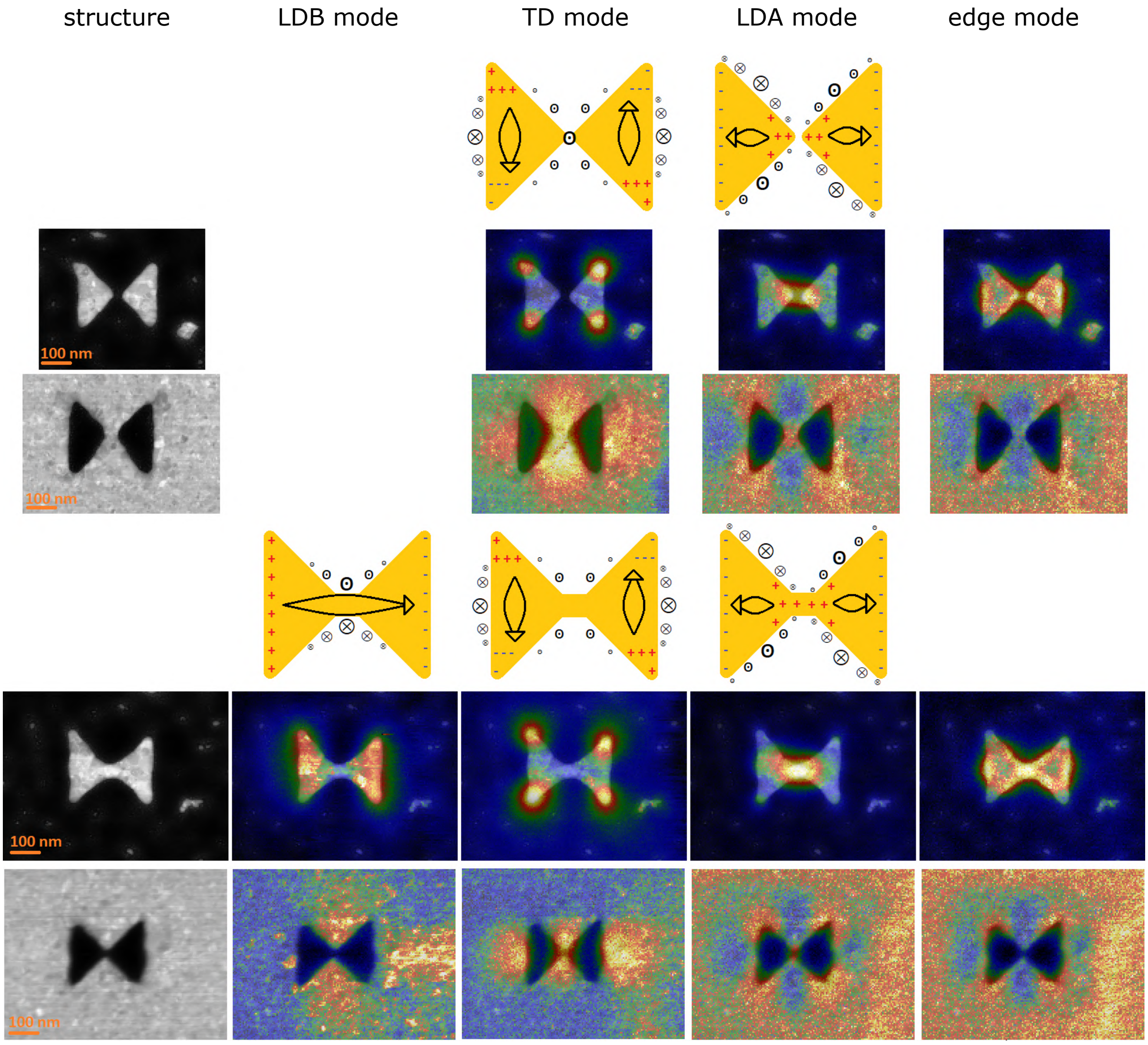

Figure 8.10: ADF STEM micrographs of structures with the schematic representation and EEL intensity maps of all discussed plasmon modes (longitudinal dipole bonding, transverse dipole, longitudinal dipole antibonding or longitudinal dipole, and edge) in all presented plasmonic antennas (bow-tie, inverted bow-tie, diabolo, and inverted diabolo) extracted from Figures 8.3 and 8.7. From the Gauss law it follows that the strongest out-of-plane electric field occurs just near the areas of the accumulated charge. Note that in the case of the particle antennas, the measured spatial distribution of the loss probability corresponds to the out-of-plane electric field distribution of the particle antenna, which is close to the accumulated charge distribution in the particle antenna. In the case of the inverted aperture antennas, it corresponds to the out-of-plane electric field distribution, which is close to the out-of-plane magnetic field distribution of the particle antenna.

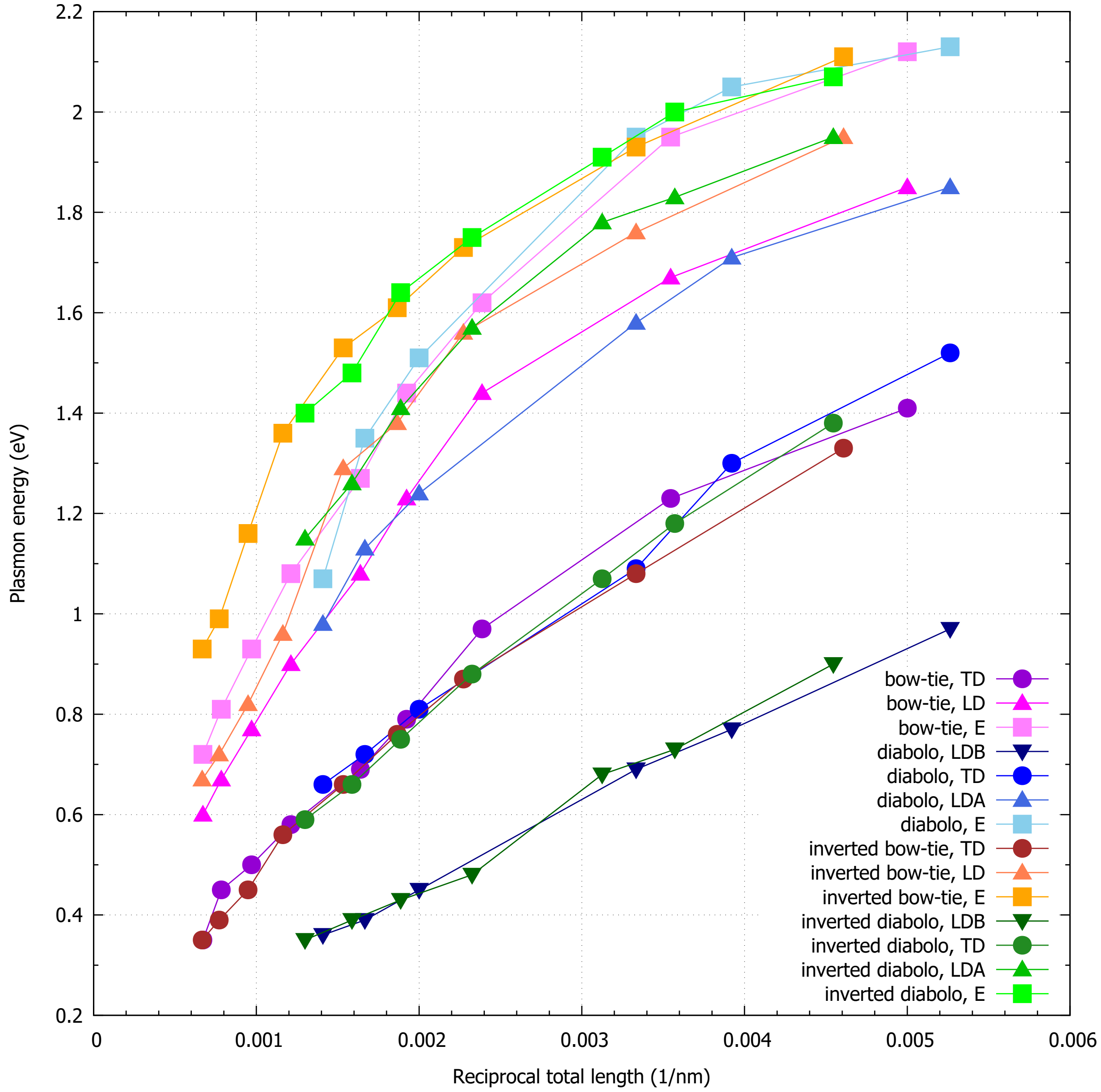

Figure 8.11: Dispersion relations showing the energies of plasmon modes as functions of the reciprocal total length of the antenna for all discussed plasmon modes (longitudinal dipole bonding – LDB, transverse dipole – TD, longitudinal dipole antibonding – LDA or longitudinal dipole – LD, and edge – E) in all presented plasmonic antennas (bow-tie – values from Table 8.1, diabolo – values from Table 8.3, inverted bow-tie – values from Table 8.2, and inverted diabolo – values from Table 8.4).

8.5 Comparison of EELS and CL measurements

After the EELS measurements a complementary CL measurement of the same antennas was performed. Our experimental CL setup is restricted to the detection range from 1.24 eV to 2.25 eV, so the possibilities of this complementary measurement are rather limited. The lower limit corresponds to a restriction by a significant absorption of the light in the near-infrared spectral region in the optical fibers as the CL spectrometer is designed mostly for the visible spectral range. Therefore, the comparison must be done for the smallest structures. Even in that case the longitudinal dipole bonding mode of

(a) bow-tie antenna, total length 200 nm

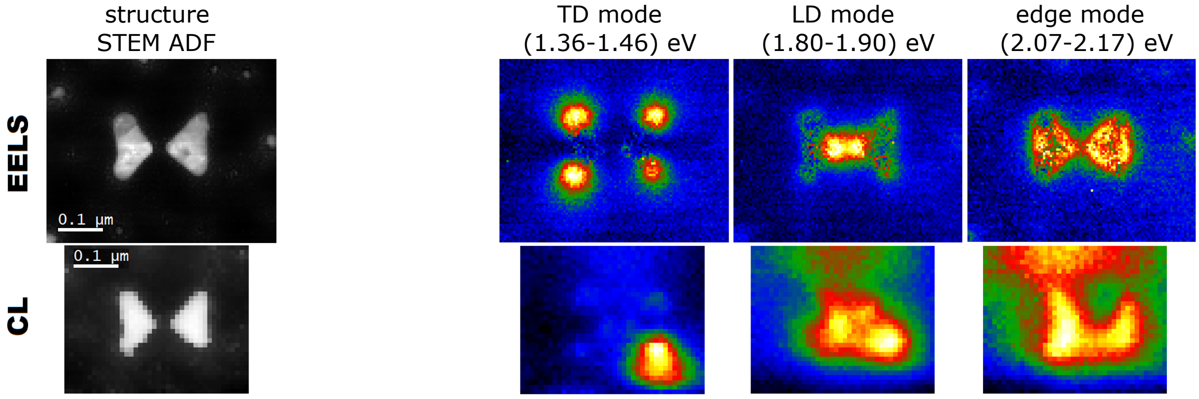

(b) diabolo antenna, total length 190 nm

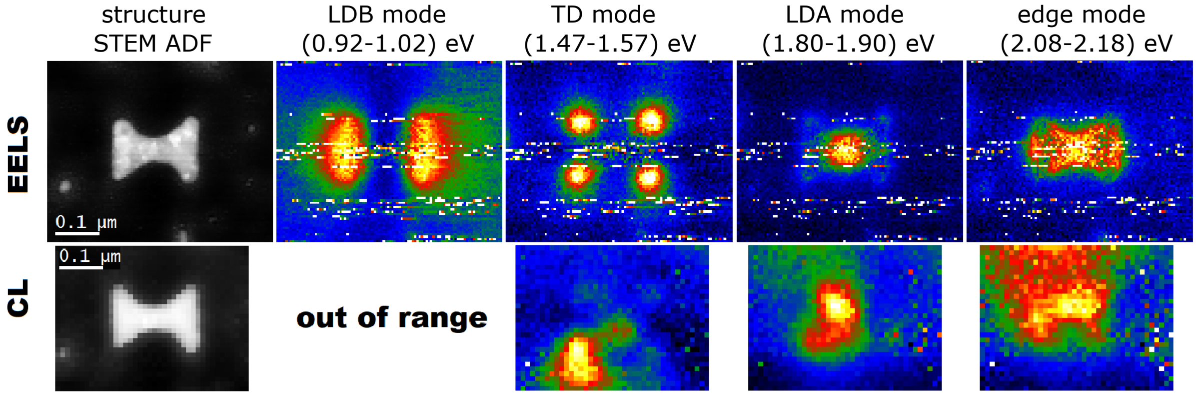

Figure 8.12: Comparison of the loss probability maps measured by EELS and the CL intensity maps: Annular dark field STEM micrographs of the bow-tie (a) and the diabolo (b) antenna followed by the loss probability maps and the CL intensity maps at the peak energy of the longitudinal dipole bonding (LDB) mode, the transverse dipole (TD) mode, the longitudinal dipole antibonding (LDA) mode or the longitudinal dipole (LD) mode, and the edge mode.

the smallest diabolo antenna and the smallest inverted diabolo antenna is out of the detectable energy range.

Figure 8.12 shows the comparison of loss probability maps measured by EELS and CL intensity maps at the same energy for direct antennas. As the sample was prepared by focused ion beam lithography and the EELS measurement was done prior the CL measurement on the same structure, the developed hydrocarbon contamination plays a non-negligible role [75]. If the carbon contamination layer is thick enough, it can absorb the light emitted from the antenna and one detects just the light emitted from the carbon contamination layer. In the case of CL measurement the spectrum image in Figure 8.12 was recorded from bottom to top. Especially the intensity on the top of the CL image of the edge mode is strongly affected by the developed hydrocarbon contamination. Despite that some agreement between the EELS and CL measurements is visible. The signal corresponding to the transverse dipole mode is affected by a strong luminescence in one corner of the antenna, but the local maxima of detected CL intensity are slightly visible in all four corners of the antenna in the respect CL maps, similarly as in the EELS maps. The signal corresponding to the longitudinal dipole (antibonding) mode has its clear maximum in the gap or in the bridge of the antenna, which is in a reasonable agreement with EELS. Finally, the CL map corrsponding to the edge mode is, except the signal related to developed hydrocarbon contamination, rather similar to the EELS map.

Figure 8.13 shows the comparison of loss probability maps measured by EELS and CL

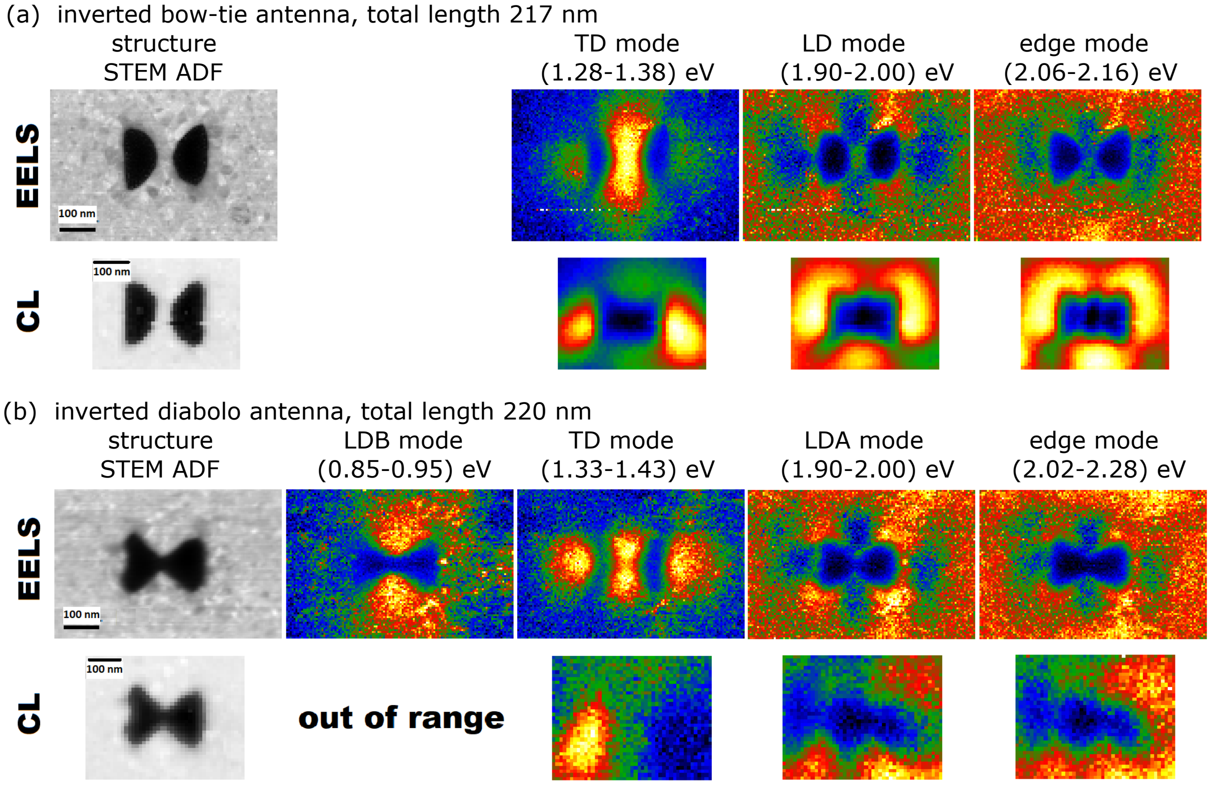

Figure 8.13: Comparison of loss probability maps measured by EELS and CL intensity maps: Annular dark field STEM micrographs of the inverted bow-tie (a) and the inverted diabolo (b) antenna followed by the loss probability maps and the CL intensity maps at the peak energy of the longitudinal dipole bonding (LDB) mode, the transverse dipole (TD) mode, the longitudinal dipole antibonding (LDA) mode or the longitudinal dipole (LD) mode, and the edge mode.

intensity maps at the same energy for inverted antennas. The correspondence between EELS and CL maps is generally worse than in the case of direct structures. The main difference is the gap or the bridge of the inverted antennas. In this position, the EELS maps reveals maximum of the loss probability for the transverse dipole mode, whereas CL detects a minimum there indicating that the tranversal dipole excited by an electron beam positioned in the gap or on the bridge of the antenna is nonradiative. The correspondence is rather good in the case of the longitudinal dipole (antibonding) and the edge mode. However, in the case of the inverted bow-tie antenna one can observe the highest CL intensity on the outer edges of the antenna and the longitudinal dipole and edge modes are modulated by a three-fold symmetry pattern. The origin of this feature is unclear. It can be caused, for example, by the asymmetry of parabolic mirrors collecting the emitted light. It should be noticed that such a three-fold symmetry pattern was observed in all CL maps recorded on inverted bow-tie antennas.

8.6 Conclusion

To conclude, I have summarized the independent engineering of individual LSP modes in composite plasmonic antennas based on varying the coupling between the components via the insulating gap or the conductive bridge. LSP modes in bow-tie and diabolo antennas and apertures were identified and their properties such as the origin of transverse and longitudinal dipole modes, the spatial distribution of the modes, their tunability through the near-infrared and visible red spectral region, and Babinet's complementarity between direct and inverted antennas were described. The corresponding modes in direct and inverted antennas, despite having identical energy, strongly differ in the spatial distribution of measured loss probability or the out-of-plane electric near fields. To extend the available energy range to the whole visible region it would be necessary to replace gold by another metal, for example, aluminum or silver. This would allow to explore the EELS and CL complementarity more accurately, too.

9 Silver amalgam nanoparticles

Silver amalgam is one of the most suitable solid electrode materials in electroanalysis of various reducible organic and inorganic compounds. They include heavy metals, agrochemicals, colorants, drugs, environmental pollutants, or biologically important compounds such as DNA, proteins and their constituents, and vitamins. The main advantage of silver amalgam within this context is its wide cathodic potential window, high mechanical stability, adequate sensitivity, and advantageous strong interaction with biopolymers (e.g. DNA and proteins) [222]. Nanostructuring the amalgam promises improved electrochemical performance and brings along the prospect of plasmonic activity. However, currently there is a lack of knowledge about the optical properties of nanostructured or even bulk silver amalgam which prevents its using in spectroelectrochemical and photochemical studies. In this chapter, a study of optical properties of silver amalgam and the plasmonic nature of its nanoparticles by analytical electron microscopy is presented.

9.1 Methods

Silver amalgam nanoparticles were prepared by chemical synthesis on indium-tin-oxide (ITO) substrates [222]. To prepare the sample for transmission electron microscopy, the silver amalgam nanoparticles were washed off the ITO into demineralized water in an ultrasonic bath. A few microliters of this suspension was dropped onto a silicon nitride membrane and dried. We used a standard 30 nm thick silicon nitride membrane for TEM with the window size of $250 \times 250\,\mu\text{m}^2$ and frame thickness of 200 µm by Agar Scientific.

TEM measurements were performed with the TEM FEI Titan equipped with the GIF Quantum spectrometer for electron energy loss spectroscopy (EELS) and the Super-X spectrometer for Energy dispersive X-ray spectroscopy (EDS) operated at 300 kV. For the spectroscopy measurements, a monochromated scanning regime was used, the beam current was set to 0.4 nA, and the FWHM of the ZLP was around 0.13 eV. In the case of EELS, we set convergence angle to 10 mrad, collection angle to 6.6 mrad, and dispersion of the GIF to 0.01 eV/pixel. We recorded EELS spectrum images with the pixel size of 3 nm. At every pixel, 10 cross-correlated EEL spectra with the acquisition time of 0.4 ms per spectrum were taken. The EEL spectra presented in this chapter were obtained by integrating the recorded signal over several pixels in the region of interest, ZLP and background subtracted, and divided by the integral intensity of the whole spectrum to transform measured counts to a quantity proportional to the loss probability. EEL maps show the EEL intensity at the plasmon peak energy integrated over the energy window of 0.2 eV. In the case of EDS, we integrated approximately 100 EDS spectrum images with the acquisition time of 10 µs per pixel. Spectrum images were post processed in the Velox software. The EDS quantification in weight percents was performed in this software using a parabolic background model and Brown-Powell ionization cross-section model.

Numerical simulations of EELS spectra were performed using the MNPBEM toolbox

[151, 152] based on the boundary element method (BEM). The dielectric function of the thick silver amalgam film was measured using spectroscopic ellipsometry [79] and the dielectric function of the silicon nitride membrane was set to 4 [179]. For the calculations of spectra and surface charge distribution, the electron beam was positioned 20 nm from the outer side of the antenna. The obtained loss probability density was recalculated to the loss probability at 0.01 eV energy intervals (corresponding to the dispersion of the spectrometer in the experiment).

9.2 Results

The chemical composition of a silver amalgam nanoparticle measured by STEM EDS is shown in Figure 9.1. The composition is rather homogeneous and reads in weight percents $(54 \pm 4)\,\%$ of Ag and $(46 \pm 6)\,\%$ of Hg. Next to the silver amalgam nanoparticle some small silver nanoparticles are located with the composition in weight percents reading $(89 \pm 4)\,\%$ of Ag and $(11 \pm 4)\,\%$ of Hg. Elemental maps of Si and N are homogenous and correspond to the signal generated by the silicon nitride membrane.

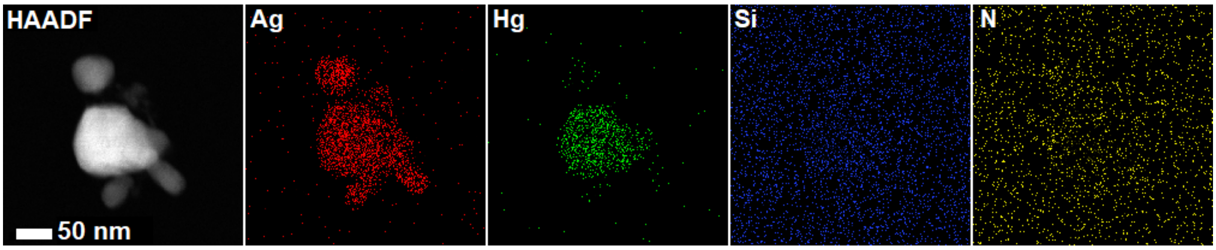

Figure 9.1: STEM HAADF micrograph of the silver amalgam nanoparticle with small silver nanoparticles around followed by the elemental maps showing the composition in weight percents of Ag and Hg constituting the nanoparticles together with Si and N from the membrane.

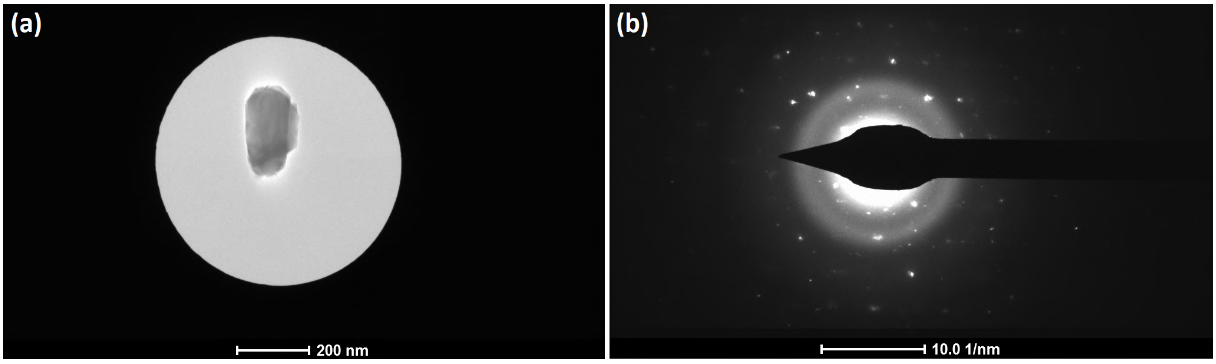

Figure 9.2: TEM micrograph (a) of a silver amalgam nanoparticle on an amorphous silicon nitride membrane and the diffraction pattern (b) from the imaged area proving the polycrystallinity of silver amalgam nanoparticles.

Figure 9.2 shows the TEM micrograph of a typical silver amalgam nanoparticle on an amorphous silicon nitride membrane. Its selected area diffraction pattern consists of two overlapping parts, the rings corresponding to the amorphous silicon nitride membrane and the points proving the polycrystallinity of the silver amalgam nanoparticle. Diffraction patterns of another silver amalgam nanoparticles are similar. Therefore, the particles are crystalline and usually consist of more grains.

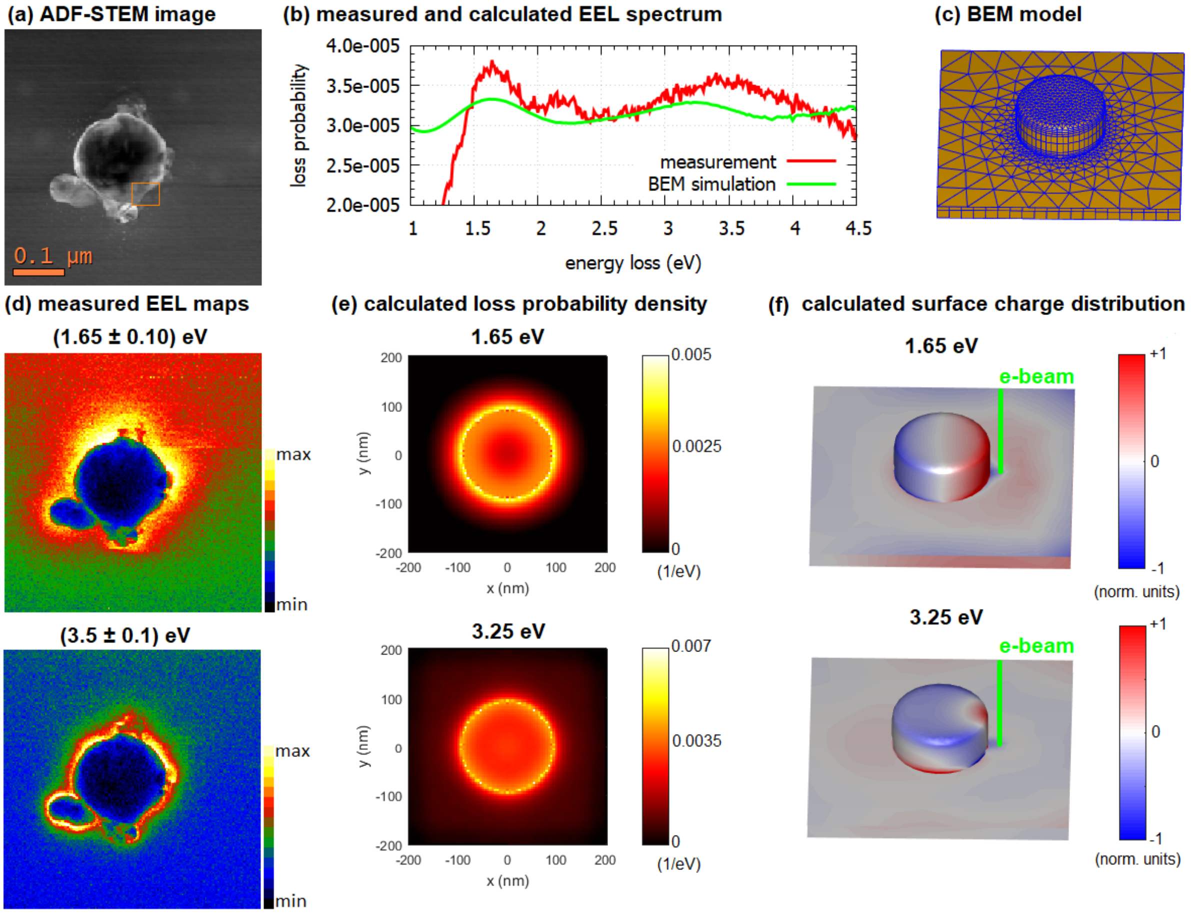

Figure 9.3: Silver amalgam nanoparticle approximated by a disc with the diameter of 175 nm and the thickness of 80 nm: (a) STEM ADF micrograph, (b) ZLP and background subtracted EEL spectrum integrated over the orange square in (a) complemented by numerical simulation, (c) simulation model of the disc with the mesh of boundary elements, (d) measured EEL maps at the energy of the peaks in (b), (e) calculated EEL maps at the energy of the peaks in (b), and (f) calculated surface charge distribution at the energy of the peaks in (b) clearly showing that the first peak corresponds to the dipole mode.

The simplest shape of an silver amalgam nanoparticle found on the sample was approximated by a disc with the diameter of 175 nm and the thickness of 80 nm. This particle was studied by EELS complemented by numerical simulations to describe the LSP resonances (Figure 9.3). The silver amalgam disc-shaped nanoparticle exhibits two peaks in the EEL spectrum. The first peak at 1.65 eV corresponds to the dipole LSP mode in the structure and the agreement between the experiment and the theory represented by the BEM simulation is excellent. The second peak at 3.5 eV in the experiment and at 3.25 eV in the theory represented by the BEM simulation show good agreement between the experiment and the theory. The difference between the experiment and the theory can be attributed to dielectric functions of silver amalgam and silicon nitride used in simulations as well as to the difference between the real shape of the particle and its idealized disc model. However, the simulation of the surface charge distribution (Figure 9.3f) does not provide much inside into the character of the mode. For better understanding to this mode a new simulation of a free standing silver amalgam disc, where the membrane was neglected, was performed. The results summarized in Figure 9.4 are much clearer. The first peak shifts from 1.65 eV to 2.1 eV and the surface charge distribution evidently corresponds to the dipole LSP mode. The second peak shifts from 3.25 eV to 3.65 eV and the surface charge distribution in this case clearly corresponds to the quadrupole mode. Therefore, I conclude that the second mode in Figure 9.3 is the quadrupole mode which is affected by the substrate represented by the silicon nitride membrane. Additionally, the quadrupole mode can be affected by the absorption in silver amalgam itself as the imaginary part of its dielectric function reaches rather high values in this spectral region. Note that the energy of the quadrupole mode in Figure 9.3 is approximately two times the energy of the dipole mode.

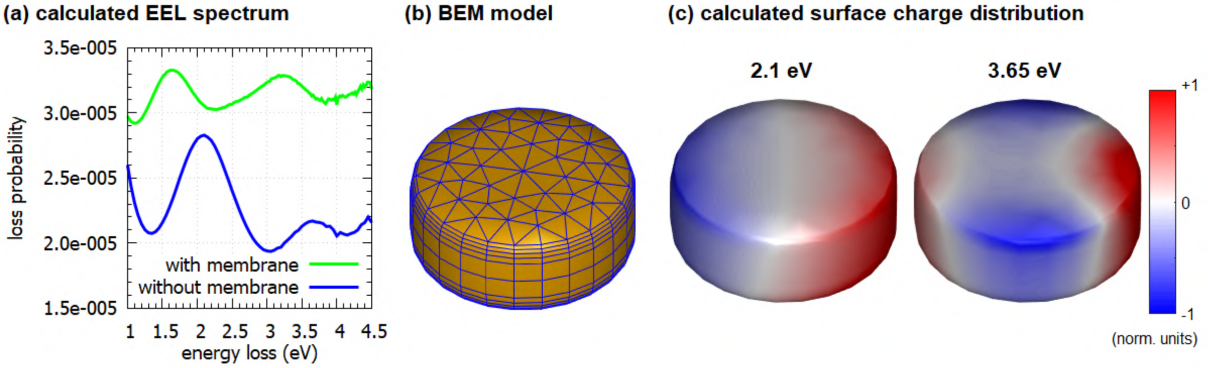

Figure 9.4: Supplementary simulations of a free standing (i.e. with the membrane neglected) silver amalgam disc with the diameter of 175 nm and the thickness of 80 nm: (a) calculated EEL spectrum, (b) simulation model of the disc, (c) calculated surface charge distribution at the energy of the peaks in (a) clearly showing that the first peak corresponds to the dipole mode and the second peak corresponds to the quadrupole mode. The 300 keV electron beam with FWHM of 0.1 eV was located 20 nm next to the disc on the right-hand side and only surface losses were considered.

A lot of silver amalgam nanoparticles have a shape of a rod. Their length ranges from 50 nm to 500 nm. A typical rod with the length of 170 nm and the width of 120 nm is shown in Figure 9.5. The chemical composition of this silver amalgam nanoparticle measured by STEM EDS is again homogeneous and reads in weight percents $(55 \pm 4)\%$ of Ag and $(45 \pm 6)\%$ of Hg. The small nanoparticle located next to the corner of the silver amalgam nanoparticle contains silver only. Elemental maps of Si and N are again homogeneous and correspond to the signal generated by the silicon nitride membrane. This particle underwent the study by EELS complemented by numerical simulations to describe the LSP resonances, too. The particle exhibits three different modes which are presented in detail in Figure 9.5. The first peak at 1.77 eV in the experiment (1.6 eV in BEM simulation) corresponds to the longitudinal dipole mode with the loss probability maxima in the middle of the short edge of the particle. The agreement between the experiment and the theory represented by the BEM simulation is very good. The second peak around 2.8 eV in the experiment (2.84 eV in BEM simulation) indicates a transverse dipole mode with the loss probability maxima in the middle of the long edge of the particle. However, the calculated surface charge distribution is not as clear as in the case of the longitudinal dipole mode and we observe this mode affected by the substrate represented by the silicon nitride membrane. The third peak around 3.2 eV in the experiment (3.15 eV in BEM simulation) corresponds to a higher-order (possibly quadrupole) mode. The calculated surface charge distribution is affected by the substrate, too. Note that the length of this rod (Figure 9.5) is close to the diameter of previously discussed disc (Figure 9.3) and the energy of the longitudinal dipole mode in the rod is similar to the energy of the dipole mode in the disc.

(a) STEM HAADF micrograph and elemental maps measured by EDS

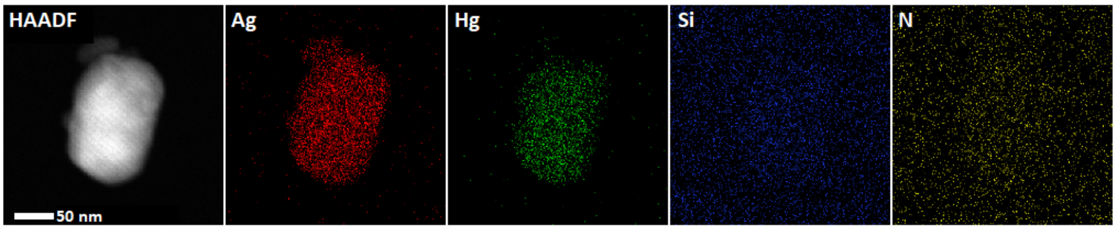

(b) measured and calculated EELS spectra

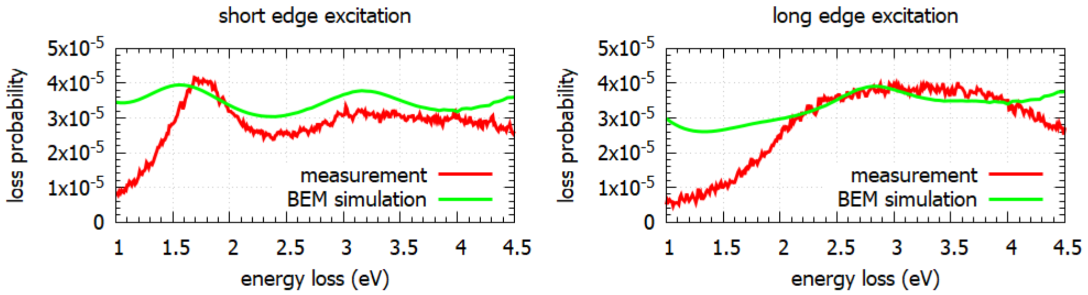

(c) STEM ADF micrograph and EEL maps at the peak energies

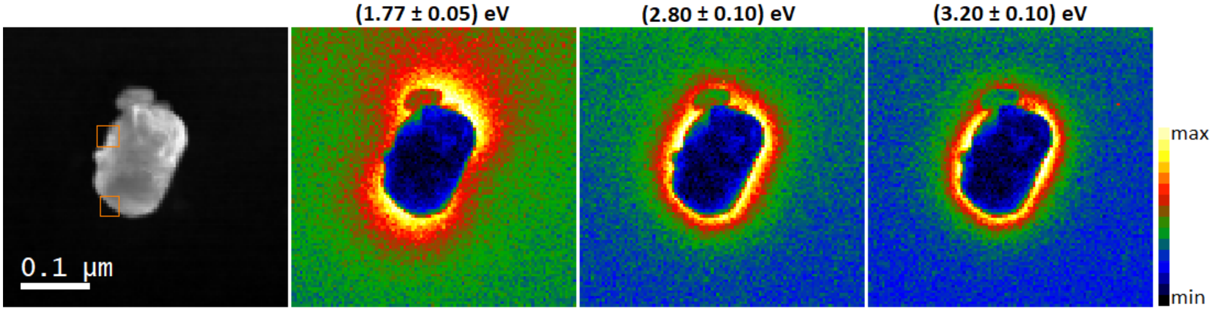

(d) BEM simulation model, simulated loss probability density and surface charge distribution

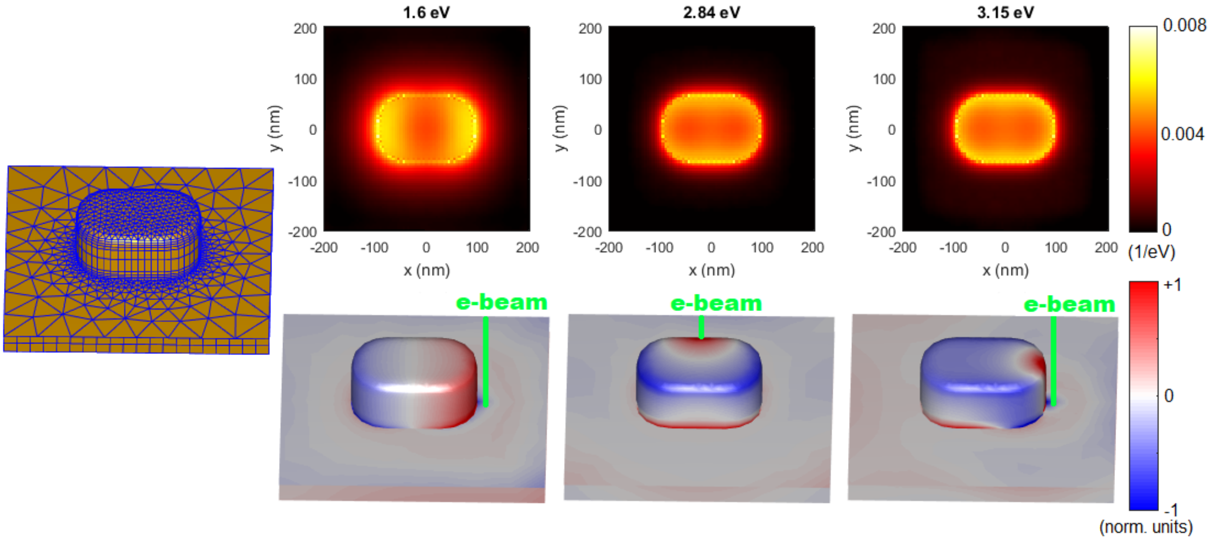

Figure 9.5: Silver amalgam nanoparticle approximated by a rod with the length of 170 nm, the width of 120 nm, and the thickness of 80 nm: (a) STEM HAADF micrograph and chemical composition mapped by EDS, (b) ZLP and background subtracted EEL spectra integrated over the orange squares in (c) complemented by numerical simulation corresponding to the excitation in the middle of the short edge and in the middle of the long edge of the particle, (c) STEM ADF micrograph and measured EEL maps at the energy of the peaks in (b), (d) simulation model of the disc followed by calculated EEL maps and calculated surface charge distribution at the energy of the peaks in (b) clearly showing that the first peak corresponds to the longitudinal dipole mode.

(a) measured and calculated energy of the dipole mode

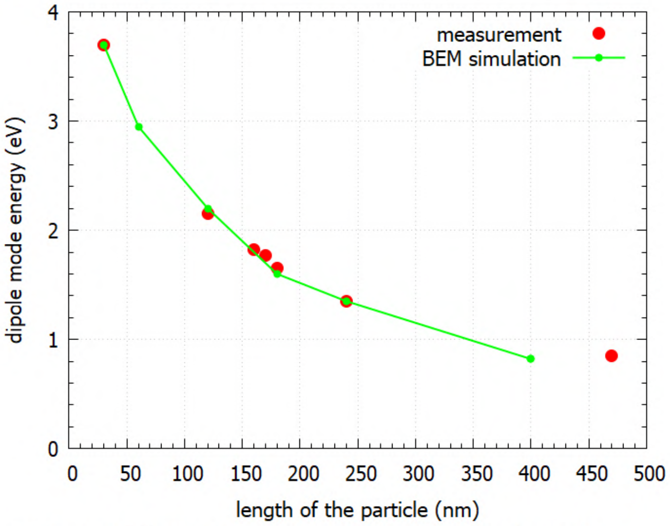

(b) STEM HAADF micrographs and EEL maps corresponding to the dipole mode

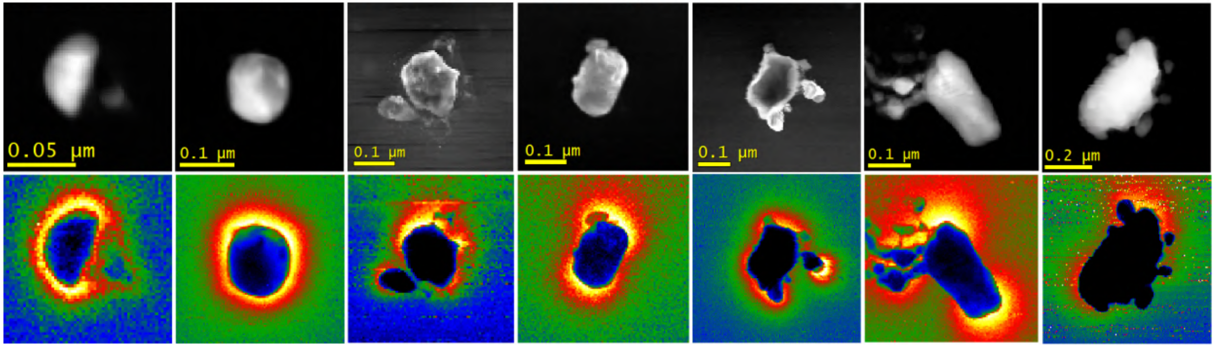

Figure 9.6: Silver amalgam nanoparticles of different sizes: (a) measured and calculated energy corresponding to the dipole mode, (b) STEM HAADF micrographs of silver amalgam nanoparticles with their characteristic size from 30 nm to 470 nm and measured EEL maps at the energy corresponding to their dipole mode.

An important thing for potential application is the spectral range which can be covered by these silver amalgam nanoparticles. Figure 9.6 shows the dependency of the energy corresponding to the dipole LSP mode as a function of the particle size. First, the theoretical model represented by BEM simulation of a series of silver amalgam nanoparticles on a 30 nm thick silicon nitride membrane was performed. In total, six simulations were performed to cover the whole range of sizes and shapes close to the nanoparticles measured by EELS. The energy of the dipole LSP mode covers the whole visible range from 0.84 eV for the largest (400 nm) structure, which is already in the near-infrared region, to 3.7 eV for the smallest (30 nm) structure, which is already in the ultraviolet region. Larger structures then support LSP resonances in the mid-infrared range. Second, this range was proved experimentally. A set of silver amalgam nanoparticles of a disc-like and a rod-like shape with their characteristic size ranging from 30 nm to 470 nm was measured by EELS (Figure 9.6b). In the case of the smallest rod like particle, the longitudinal dipole mode was not detected, but the transverse dipole mode at the energy of 3.7 eV corresponding to a characteristic size of 30 nm was measured. The disc with the diameter of 120 nm supports the dipole mode at 2.15 eV. The rod like particles with a length of 160 nm, 170 nm, 180 nm, 240 nm, and 470 nm support their longitudinal dipole mode at 1.82 eV, 1.77 eV, 1.65 eV, 1.35 eV, and 0.85 eV. Therefore, the measured dipole LSP resonances covered the whole visible range with an overlap to ultraviolet and near-infrared region. It should be noticed, that larger structures, which are not optimal for EELS measurements with our TEM microscope, have their resonances in the mid-infrared region [79]. The agreement between the simulation and the experiment is reasonably good.

9.3 Conclusion

To conclude, silver amalgam is a novel and very promising plasmonic material. By changing the size of nanostructures the dipole LSP resonance can be tuned from ultraviolet through the whole visible to infrared region. A minor disadvantage is the absorption in the silver amalgam itself as the imaginary part of its dielectric function reaches rather high values in the visible region. The main advantage is that silver amalgam is well investigated in the field of electrochemistry so the silver amalgam nanoparticles opens a possibility to combine plasmonics and electrochemistry together.

10 Conclusion

To summarize, this thesis was focused on electron and ion beam techniques for fabrication and characterization of plasmonic nanostructures. Analytical electron microscopy was discussed focusing on applications in the field of plasmonics. The emphasis was given to electron energy loss spectroscopy (EELS) and cathodoluminescence. Fabrication of plasmonic samples for transmission electron microscopy was introduced while the focus was given to focused ion beam lithography and to sample preparation using chemically synthesized particles in water solution. This thesis had four main research results.

The first result is a comparative study of plasmonic antennas fabricated by electron beam and focused ion beam lithography. While both techniques are suitable for the fabrication of plasmonic antennas, electron beam lithography shall be prioritized over focused ion beam lithography due to better quality of the resulting antennas and considerably stronger plasmonic response in EELS. Antennas fabricated by focused ion beam lithography have slightly dull edges, exhibit pronounced thickness fluctuation, and they are also strongly contaminated not only by organic contaminants, but also by residues of FIB milling including implanted milling ions and atoms of the titanium adhesion layer.

The second result is a study of Babinet's principle of complementarity for gold disc-shaped plasmonic antennas. The emphasis was given on experimental study using spatially-resolved EELS and cathodoluminescence to investigate the electromagnetic response of elementary plasmonic antennas: gold discs and complementary disc-shaped apertures in a gold layer prepared by focused ion beam lithoghraphy. I have experimentally verified that solid and hollow disc-shaped plasmonic antennas exhibit Babinet's complementarity. The complementarity was confirmed for fundamental plasmon properties such as resonance energies, but differences rising from the limited validity of Babinet's principle were found, for example, for the spatial distribution of the near-field of plasmon polaritons. Observed differences were from the practical point of view rather minor. The validity of Babinet's principle is relevant also for numerous applications. Babinet's complementarity allows to toggle between the magnetic and electric response, or between the reflection and transmission mode. While particles have to be supported by the substrate, substrate-less apertures self-supported by their frame can be fabricated. Apertures also offer better heat and charge management as the thin metallic film surrounding the apertures is usually a better conductor than the substrate supporting the particles.

The third result is the independent engineering of individual localized surface plasmon modes in composite plasmonic antennas based on varying the coupling between the components via insulating gap or conductive bridge together with Babinet's principle of complementarity. I have studied bow-tie and diabolo plasmonic antennas, both in the form of particles and in the form of apertures, which exhibit particularly strong local field enhancement. I have identified several modes of localized surface plasmons in these antennas and characterize their properties including mode energy, near field electric and magnetic field distribution, and the qualitative distribution of charge nodes and current associated with electron gas oscillations. I have studied mode energy tunability in near infrared and visible spectral regions and Babinet's complementarity between direct and inverted antennas. The corresponding modes in direct and inverted antennas, despite having identical energy, strongly differ in the spatial distribution of measured loss probability or the out-of-plane electric near fields, respectively. From the Gauss law it follows that the strongest out-of-plane electric field occurs just near the areas of the accumulated charge. Note that the measured spatial distribution of the loss probability corresponds, in the case of a particle antenna, to the out-of-plane electric field distribution in this antenna, which is close to the accumulated charge distribution of the particle antenna. In the case of an inverted aperture antenna, it corresponds to the out-of-plane electric field distribution of the aperture antenna, which is close to the out-of-plane magnetic field distribution of the particle antenna.

The fourth result is the characterization of a novel plasmonic material – silver amalgam. I have studied nanparticles made of silver amalgam. I have experimentally proved that by changing the size of nanostructures the dipole localized surface plasmon resonance can be tuned through the whole visible and infrared region. A minor disadvantage is the absorption in the silver amalgam itself as the imaginary part of its dielectric function reaches rather high values in the visible region. The main advantage is that silver amalgam is well investigated in the field of electrochemistry so the silver amalgam nanoparticles opens a possibility to combine plasmonics and electrochemistry together.

To conclude, in this Thesis I have introduced the application of analytical electron microscopy in the field of plasmonics covering both the fabrication and characterization processes. I have fully covered all five main aims: (i) to introduce analytical electron microscopy and its prospective for plasmonics and to give a brief overview of fabrication of plasmonic antennas for electron beam spectroscopy investigations focused on focused ion beam lithoghraphy, (ii) to investigate elementary gold plasmonic antennas with focus on Babinet's principle of complementarity, (iii) to study nanostructures with functional properties related to the local enhancement of electric and magnetic field, (iv) to explore the possibility of fabrication of plasmonic antennas using based on a frequently used material, and (v) to study coupled structures. Finally, my work have contributed to the publication of several manuscripts, and paved the way for a wide use of presented techniques at CEITEC BUT in the future.

Further research in this field may deal, for example, with the following topics. Gold can be replaced by another metal, for example, aluminum or silver to extend the available energy range to the whole visible region. This would be necessary to explore the EELS and CL complementarity more accurately. Second, the strong coupling phenomena with the substrate is observed in the infrared range, which was not accessible by available analytical transmission electron microscopes as it requires either an ultra high energy resolution EELS, or CL spectrometer designed for the respect infrared spectral region. However, it is not impossible to measure it in the near future in a laboratory with a suitable microscope. Another possibility is to use phase shaped electron beams for EELS or cathodoluminescence. To summarize, analytical electron microscopy in plasmonics will deal with many interesting topics in the future.

References

[1] Novotny, L., Hecht, B.: *Principles of Nano-Optics*. Cambridge Press New York, 2006, 539 p. ISBN 978-0-521-83224-3.

[2] Ritchie, R. H.: Plasma losses by fast electrons in thin films. *Physical Review*, vol. 106, 1957, p. 874.

[3] Powell, C. J., Swan, J. B.: Effect of oxidation on the characteristic loss spectra of aluminum and magnesium. *Physical Review*, vol. 118, 1960, p. 640.

[4] Otto, A.: Theory of plasmon excitation in thin films by electrons. *Physica status solidi*, vol. 22, 1967, p. 401.

[5] Lucas, A. A., Šunjič, M.: Fast-electron spectroscopy of surface excitations. *Physical Review Letters*, vol. 26, 1971, p. 229.

[6] Kröger, E.: Berechnung der Energieverluste schneller Elektronen in dünnen Schichten mit Retardierung. *Zeitschrift für Physik*, vol. 216, 1968, p. 115.

[7] Kröger, E.: Transition radiation, Cerenkov radiation and energy losses of relativistic charged particles traversing thin foils at oblique incidence. *Zeitschrift für Physik*, vol. 235, 1970, p. 403.

[8] Maier, S. A.: *Plasmonics: Fundamentals and Applications*. Springer Science+Business Media LLC New York, 2007. ISBN 978-0387-33150-8.

[9] Mie, G.: Beiträge zur Optik trüber Medien, speziell kolloidaler Metallösungen. *Annalen der Physik*, vol. 25, 1908, p. 377.

[10] Batson, P. E.: Surface plasmon coupling in clusters of small spheres. *Physical Review Letters*, vol. 49, 1982, p. 1682.

[11] Schuller, J. A., *et al.*: Plasmonics for extreme light concentration and manipulation. *Nature Materials*, vol. 9, 2010, p. 193.

[12] Kelly, K. L., *et al.*: The optical properties of metal nanoparticles: The influence of size, shape, and dielectric environment. *Journal of Physical Chemistry B*, vol. 107, 2003, p. 668.

[13] Stockman, M. I.: Nanoplasmonics: The physics behind the applications. *Physics Today*, vol. 64, 2011, p. 39.

[14] Stockman, M. I., *et al.*: Roadmap on plasmonics. *Journal of Optics*, vol. 20, 2018, p. 043001.

[15] Salerno, M., *et al.*: Plasmon polaritons in metal nanostructures: The optoelectronic route to nanotechnology. *Opto-Electronics Review*, vol. 10, 2002, p. 217.

[16] Mattiucci, N., D'Aguanno, G., Bloemer, M. J.: Long range plasmon assisted all-optical switching at telecommunication wavelengths. *Optics Letters*, vol. 37, 2012, p.121.

[17] Knight, M. W., *et al.*: Photodetection with active optical antennas. *Science*, vol. 332, 2011, p. 702.

[18] Smolyaninov, I. I., *et al.*: Far-field optical microscopy with a nanometer-scale resolution based on the in-plane image magnification by surface plasmon polaritons. *Physical Review Letters*, vol. 94, 2005, p. 057401.

[19] Willets, K. A., Van Duyne, R. P.: Localized surface plasmon resonance spectroscopy and sensing. *Annual Review of Physical Chemistry*, vol. 58, 2007, p. 267.

[20] Boriskina, S. V., Ghasemi, H., Chen, G.: Plasmonic materials for energy: From physics to applications. *Materials Today*, vol. 16, 2013, p. 375.

[21] Aćimović, S. S., *et al.*: LSPR chip for parallel, rapid, and sensitive detection of cancer markers in serum. *Nano Letters*, vol. 14, 2014, p. 2636.

[22] Baffou, G., Quidant, R.: Thermo-plasmonics: Using metallic nanostructures as nanosources of heat. *Laser & Photonic Review*, vol. 7, 2013, p. 171.

[23] Sheldon, M. T., *et al.*: Plasmoelectric potentials in metal nanostructures. *Science* vol. 346, 2014, p. 828.

[24] Zheludev, N. I., *et al.*: Lasing spaser. *Nature Photonics*, vol. 2, 2008, p. 351.

[25] Yu, N., *et al.*: Light propagation with phase discontinuities: generalized laws of reflection and refraction. *Science* vol. 334, 2011, p. 333.

[26] Cardano, F., Marrucci, L.: Spin–orbit photonics. *Nature Photonics*, vol. 9, 2015, p. 776.

[27] Valev, V. K., *et al.*: Chirality and chiroptical effects in plasmonic nanostructures: fundamentals, recent progress, and outlook. *Advanced Materials*, vol. 25, 2013, p. 2517.

[28] Falcone, F., *et al.*: Babinet principle applied to the design of metasurfaces and metamaterials. *Physical Review Letters*, vol. 93, 2004, p. 197401.

[29] Zentgraf, T., *et al.*: Babinet's principle for optical frequency metamaterials and nanoantennas *Physical Review B*, vol. 76, 2007, p. 033407.

[30] Ferrando, R., Jellinek, J., Johnston, R. L.: Nanoalloys: From theory to applications of alloy clusters and nanoparticles. *Chemical Reviews*, vol. 108, 2008, p. 845.

[31] Kunkemöller, G., *et al.*: Extreme ultraviolet proximity lithography for fast, flexible and parallel fabrication of infrared antennas. *Optics Express*, vol. 23, 2015, p. 25487.

[32] Vieu, C., *et al.*: Electron beam lithography: resolution limits and applications. *Applied Surface Science*, vol. 164, 2000, p. 111.

[33] Taylor, A. B., *et al.*: Electron-beam lithography of plasmonic nanorod arrays for multilayered optical storage. *Optics Express*, vol. 22, 2014, p. 13234.

[34] Joshi-Imre, A., Bauerdick, S.: Direct-write ion beam lithography. *Journal of Nanotechnology*, vol. 2014, 2014, p. 170415.

[35] Kollmann, H., *et al.*: Toward plasmonics with nanometer precision: nonlinear optics of helium-ion milled gold nanoantennas. *Nano Letters*, vol. 14, 2014, p. 4778.

[36] Winkler, R., *et al.*: Direct-write 3D nanoprinting of plasmonic structures. *ACS Applied Materials & Interfaces*, vol. 9, 2017, p. 8233.

[37] Winkler, R., *et al.*: High-fidelity 3D-nanoprinting via focused electron beams: growth fundamentals. *ACS Appllied Nano Materials*, vol. 1, 2018, p. 1014.

[38] Knight, M. W., *et al.*: Aluminum for Plasmonics. *ACS Nano*, vol. 8, 2014, p. 834.

[39] King, N. S., *et al.*: Fano resonant aluminum nanoclusters for plasmonic colorimetric sensing. *ACS Nano*, vol. 9, 2015, p. 10628.

[40] Cheng, F., *et al.*: Aluminum plasmonic metamaterials for structural color printing. *Optics Express*, vol. 23, 2015, p. 14552.

[41] Madsen, S. J., *et al.*: Observing plasmon damping due to adhesion layers in gold nanostructures using electron energy loss spectroscopy. *ACS Photonics*, vol. 4, 2017, p. 268.

[42] Habteyes, T. G., *et al.*: Metallic adhesion layer induced plasmon damping and molecular linker as a nondamping alternative. *ACS Nano*, vol. 6, 2012, p. 5702.

[43] Tinguely, J. C., *et al.*: Gold nanoparticles for plasmonic biosensing: the role of metal crystallinity and nanoscale roughness. *BioNanoScience*, vol. 1, 2011, p. 128.

[44] Bosman, M., *et al.*: Encapsulated annealing: enhancing the plasmon quality factor in lithographically-defined nanostructures. *Scientific Reports*, vol. 4, 2014, p. 5537.

[45] Rodríguez-Fernández, J., *et al.*: The effect of surface roughness on the plasmonic response of individual sub-micron gold spheres. *Physical Chemistry Chemical Physics*, vol. 11, 2009, p. 5909.

[46] Trügler, A., *et al.*: Influence of surface roughness on the optical properties of plasmonic nanoparticles. *Physical Review B*, vol. 83, 2011, p. 081412.

[47] Hu, M., *et al.*: Dark-field microscopy studies of single metal nanoparticles: understanding the factors that influence the linewidth of the localized surface plasmon resonance. *Journal of materials chemistry*, vol. 18, 2008, p. 1949.

[48] Cao, W., *et al.*: Localized surface plasmon resonance of single silver nanoparticles studied by dark-field optical microscopy and spectroscopy. *Journal of Applied Physics*, vol. 109, 2011, p. 034310.

[49] Ashino, M., Ohtsu, M.: Fabrication and evaluation of a localized plasmon resonance probe for near-field optical microscopy/spectroscopy. *Applied Physics Letters*, vol. 72, 1998, p. 1299.

[50] Vasconcelos, T. L., *et al.*: Tuning Localized Surface Plasmon Resonance in Scanning Near-Field Optical Microscopy Probes. *ACS Nano*, vol. 9, 2015, p. 6297.

[51] García de Abajo, F. J.: Optical excitations in electron microscopy. *Reviews of modern physics*, vol. 82, 2010, p. 209.

[52] Losquin, A., Lummen, T. T. A.: Electron microscopy methods for space-, energy-, and time-resolved plasmonics. *Frontiers of Physics*, vol. 12, 2017, p. 127301.

[53] Nelayah, J., *et al.*: Mapping surface plasmons on a single metallic nanoparticle. *Nature Physics*, vol. 3, 2007, p. 348.

[54] Colliex, C., Kociak, M., Stéphan, O.: Electron energy loss spectrometry imaging of surface plasmons at the nanometer scale. *Ultramicroscopy*, vol. 162, 2016, p. A1.

[55] Wu, Y., Li, G., Camden, J. P.: Probing nanoparticle plasmon with electron energy loss spectroscopy. *Chemical Reviews*, vol. 118, 2018, p. 2994.

[56] Nelayah, J., *et al.*: Direct imaging of surface plasmon resonances on single triangular silver nanoprisms at optical wavelength using low-loss EFTEM imaging. *Optics Letters*, vol. 34, 2009, p. 1003.

[57] Yamamoto, N., Araya, K., García de Abajo, F. J.: Photon emission from silver particles induced by a high-energy electron beam. *Physical Review B*, vol. 64, 2001, p. 205419.

[58] Yamamoto, N.: Development of high-resolution cathodoluminescence system for STEM and application to plasmonic nanostructures. *Microscopy*, vol. 65, 2016, p. 282.

[59] Sun, Q., *et al.*: Direct imaging of the near field and dynamics of surface plasmon resonance on gold nanostructures using photoemission electron microscopy. *Light: Science & Applications*, vol. 2, 2013, p. e118.

[60] Park, S. T., Lin, M., Zewail1, A. H.: Photon-induced near-field electron microscopy (PINEM): theoretical and experimental. *New Journal of Physics*, vol. 12, 2010, p. 123028.

[61] Asenjo-Garcia, A., García de Abajo, F. J.: Plasmon electron energy-gain spectroscopy. *New Journal of Physics*, vol. 15, 2013, p. 103021.

[62] Tizei, L.H.G., *et al.*: Monolayer and thin h-BN as substrates for electron spectro-microscopy analysis of plasmonic nanoparticles. *Applied Physics Letters*, vol. 113, 2018, p. 231108.

[63] Department of Solid State Physics and Surfaces, Brno University of Technology: *Plasmonics & Nanophotonics.* <http://surfaces.fme.vutbr.cz/research/plasmonics/>

[64] Babocký, J., *et al.*: Quantitative 3D phase imaging of plasmonic metasurfaces. *ACS Photonics*, vol. 4, 2017, p. 1389.

[65] Ligmajer, F., *et al.*: Epitaxial VO2 nanostructures: a route to large-scale, switchable dielectric metasurfaces. *ACS Photonics*, vol. 5, 2018, p. 2561.

[66] Dvořák, P., *et al.*: Control and near-field detection of surface plasmon interference patterns. *Nano Letters*, vol. 13, 2013, p. 2558.

[67] Dvořák, P., *et al.*: Imaging of near-field interference patterns by aperture-type SNOM – influence of illumination wavelength and polarization state. *Optics Express*, vol. 25, 2017, p. 16560.

[68] Dvořák, P., *et al.*: Near-field digital holography: a tool for plasmon phase imaging. *Nanoscale*, vol. 10, 2018, p. 21363.

[69] Bouchal, P., *et al.*: High-resolution quantitative phase imaging of plasmonic metasurfaces with sensitivity down to a single nanoantenna. *Nano Letters*, vol. 19, 2019, p. 1242.

[70] Křápek, V., *et al.*: Spatially resolved electron energy loss spectroscopy of crescent-shaped plasmonic antennas. *Optics Express*, vol. 23, 2015, p. 11855.

[71] Horák, M., *et al.*: Limits of Babinet's principle for solid and hollow plasmonic antennas. *Scientific Reports*, vol. 9, 2019, p. 4004.

[72] Babocký, J.: *Fabrication and characterization of nanostructures with functional properties in the field of plasmonics I.* Brno: Vysoké učení technické v Brně, Středoevropský technologický institut, 2019. Dizertační práce, vedoucí práce prof. RNDr. Tomáš Šikola, CSc.

[73] Babocký, J., *et al.*: Patterning large area plasmonic nanostructures on nonconductive substrates using variable pressure electron beam lithography. *Journal of Vacuum Science & Technology B*, vol. 34, 2016, p. 06K801.

[74] Šamořil, T.: *Aplikace fokusovaného iontového a elektronového svazku v nanotechnologiích.* Brno: Vysoké učení technické v Brně, Fakulta strojního inženýrství, 2015. 126 s. Dizertační práce, vedoucí práce prof. RNDr. Tomáš Šikola, CSc.

[75] Horák, M., *et al.*: Comparative study of plasmonic antennas fabricated by electron beam and focused ion beam lithography. *Scientific Reports*, vol. 8, 2018, p. 9640.

[76] Hrtoň, M., Křápek, V., Šikola, T.: Boundary element method for 2D materials and thin films. *Optics Express*, vol. 25, 2017, p. 23709.

[77] Břínek, L.: *Aplikace plazmonových polaritonů v nanofotonice.* Brno: Vysoké učení technické v Brně, Fakulta strojního inženýrství, 2015. 75 s. Dizertační práce, vedoucí práce Prof. RNDr. Petr Dub, CSc.

[78] Horák, M., Křápek, V., Šikola, T.: Plazmonové rezonance ve zlatých nanočásticích zkoumané s využitím elektronové mikroskopie. *Jemná Mechanika a Optika*, vol. 62, 2017, p. 303.

[79] Ligmajer, F., *et al.*: Silver amalgam nanoparticles: a novel plasmonic platform for spectro-electrochemistry. *Journal of Physical Chemistry C*, vol. 123, 2019, p. 16957.

[80] Křápek, V., *et al.*: Independent engineering of individual plasmon modes in plasmonic dimers with conductive and capacitive coupling. *Arxiv preprint*, arxiv:1905.09210.

[81] Horák, M.: *Příprava a charakterizace nanostruktur s funkčními vlastnostmi v oblasti plazmoniky.* Brno: Vysoké učení technické v Brně, Středoevropský technologický institut VUT, 2017. 41 s. Vedoucí pojednání prof. RNDr. Tomáš Šikola, CSc.

[82] Hrtoň, M., *et al.*: Plasmonic antennas with electric, magnetic, and electromagnetic hot spots based on Babinet's principle. *Arxiv preprint*, arxiv:1904.01397.

[83] Koh, A. L., *et al.*: Electron energy-loss spectroscopy (EELS) of surface plasmons in single silver nanoparticles and dimers: Influence of beam damage and mapping of dark modes. *ACS Nano*, vol. 3, 2009, p. 3015.

[84] Flauraud, V., *et al*: Mode coupling in plasmonic heterodimers probed with electron energy loss spectroscopy. *ACS Nano*, vol. 11, 2017, p. 3485.

[85] Zengin, G., *et al.* Approaching the strong coupling limit in single plasmonic nanorods interacting with J-aggregates. *Scientific Reports*, vol. 3, 2013, p. 3074.

[86] Konečná, A., *et al.* Surface-enhanced molecular electron energy loss spectroscopy. *ACS Nano*, vol. 12, 2018, p. 4775.

[87] Wei, J., *et al.*: Strong coupling between ZnO excitons and localized surface plasmons of silver nanoparticles studied by STEM-EELS. *Nano Letters*, vol. 15, 2015, p. 5926.

[88] Bitton, O., *et al.* Vacuum Rabi splitting of a dark plasmonic cavity mode revealed by fast electrons. *Arxiv preprint*, arxiv:1907.10299.

[89] Tizei, L. H. G., *et al.* Tailored nanoscale plasmon-enhanced vibrational electron spectroscopy. *Arxiv preprint*, arxiv:1905.12503.

[90] Yankovich, A. B., *et al.* Visualizing plasmon-exciton polaritons at the nanoscale using electron microscopy. *Arxiv preprint*, arxiv:1905.04067.

[91] Břínek, L., *et al.*: Plasmon resonances of mid-IR antennas on absorbing substrate: optimization of localized plasmon-enhanced absorption upon strong coupling effect. *ACS Photonics*, vol. 5, 2018, p. 4378.

[92] Horák, M., Zlámal, J.: Accurate interpolation of 3D fields close to the optical axis. *Microscopy and Microanalysis*, vol. 21, 2015, p. 242.

[93] Horák, M., Zlámal, J.: Accurate interpolation of 3D fields in charged particle optics. *Ultramicroscopy*, vol. 189, 2018, p. 95.

[94] Ferreira, I., *et al.*: Design of the charged particle diverters for the ATHENA mission. *Proceedings of SPIE - The International Society for Optical Engineering*, vol. 10699, 2018, p. 106994A.

[95] Horák, M., Stöger-Pollach, M.: The Čerenkov limit of Si, GaAs and GaP in electron energy loss spectrometry. *Ultramicroscopy*, vol. 157, 2015, p. 73.

[96] Zdražil, L., *et al.*: Preparation of graphene quantum dots through liquid phase exfoliation method. *Journal of Luminescence*, vol. 204, 2018, p. 203.

[97] Stöger-Pollach, M., *et al.*: Fundamentals of cathodoluminescence in a STEM: The impact of sample geometry and electron beam energy on light emission of semiconductors. *Ultramicroscopy*, vol. 200, 2019, p. 111.

[98] Řiháček, T., *et al.*: Creation of electron vortex beams using the holographic reconstruction method in a scanning electron microscope. In: *Recent Trends in Charged Particle Optics and Surface Physics Instrumentation. Proceedings of the 16th International Seminar.* Brno: Institute of Scientific Instruments The Czech Academy of Sciences, 2018, p. 66. ISBN 978-80-87441-23-7.

[99] Williams, D. B., Carter, C. B.: *Transmission Electron Microscopy.* Springer Science + Business Media New York, 2009. ISBN 978-0-387-76502-0.

[100] Egerton, R. F.: *Electron Energy-Loss Spectroscopy in the Electron Microscope.* Springer, 2011. ISBN 978-1-4419-9582-7.

[101] Leithäuser, G.: Über den Geschwindigkeitsverlust, welchen die Kathodenstrahlen beim Durchgang durch dünne Metallschichten erleiden. *Annalen der Physik*, vol. 15, 1904, p. 283.

[102] Hillier, J., Baker, R. F.: Microanalysis by means of electrons. *Journal of Applied Physics*, vol. 15, 1944, p. 663.

[103] Sunaoshi, T., *et al.*: STEM/SEM, chemical analysis, atomic resolution and surface imaging at $\leq$ 30 kV with no aberration correction for nanomaterials on graphene support. *Microscopy and Microanalysis* vol. 22(S3), 2016, p. 604.

[104] Brodusch, N., *et al.*: Electron energy-loss spectroscopy (EELS) with a cold-field emission scanning electron microscope at low accelerating voltage in transmission mode. *Ultramicroscopy*, 2019.

[105] Stöger-Pollach, M.: Optical properties and bandgaps from low loss EELS: Pitfalls and solutions. *Micron*, vol. 39, 2008, p. 1092.

[106] Iakoubovskii, K., *et al.*: Thickness measurements with electron energy loss spectroscopy. *Microscopy Research and Technique*, vol. 71, 2008, p. 626.

[107] Boniface, M., *et al.*: Nanoscale chemical evolution of silicon negative electrodes characterized by low-loss STEM-EELS.

[108] Stöger-Pollach, M., Laister, A., Schattschneider, P.: Treating retardation effects in valence EELS spectra for Kramers–Kronig analysis. *Ultramicroscopy*, vol. 108, 2008, p. 439.

[109] Losquin, A., Kociak, M.: Link between cathodoluminescence and electron energy loss spectroscopy and the radiative and full electromagnetic local density of states. *ACS Photonics*, vol. 2, 2015, p. 1619.

[110] Kothleitner, G.: EELS & EFTEM imaging: Instrumentation, applications and artifacts. *Microscopy and Microanalysis*, vol. 16 (S2), 2010, p. 1946.

[111] Valadares, L. F., *et al.*: Low-energy-loss EFTEM imaging of thick particles and aggregates. *Journal of Colloid and Interface Science*, vol. 309, 2007, p. 140.

[112] Schaffer, B., *et al.*: Comparison of EFTEM and STEM EELS plasmon imaging of gold nanoparticles in a monochromated TEM. *Ultramicroscopy*, vol. 110, 2010, p. 1087.

[113] Krivanek, O. L., Gubbens, A. J., Dellby, N.: Developments in EELS instrumentation for spectroscopy and imaging. *Microscopy Microanalysis Microstructures*, vol. 2, 1991, p. 315.

[114] Krivanek, O. L., *et al.*: Design and first applications of a post-column imaging filter. *Microscopy Microanalysis Microstructures*, vol. 3, 1992, p. 187.

[115] Krivanek, O. L., *et al.*: Monochromated STEM with a 30 meV-wide, atom-sized electron probe. *Microscopy*, vol. 62, 2013, p. 3.

[116] Krivanek, O. L., *et al.*: Progress in ultrahigh energy resolution EELS *Ultramicroscopy*, vol. ??, 2019?, p. ??.

[117] Krivanek, O. L., *et al.*: Vibrational spectroscopy in the electron microscope. *Nature*, vol. 514, 2014, p. 209.

[118] Krivanek, O. L., *et al.*: Atom-by-atom structural and chemical analysis by annular dark-field electron microscopy. *Nature*, vol. 464, 2010, p. 571.

[119] Egerton, R. F.: Scattering delocalization and radiation damage in STEM-EELS. *Ultramicroscopy*, vol. 180, 2017, p. 115.

[120] Crozier, P. A.: Vibrational and valence aloof beam EELS: A potential tool for nondestructive characterization of nanoparticle surfaces. *Ultramicroscopy*, vol. 180, 2017, p. 104.

[121] Tsuno, K.: Monochromators in electron microscopy. *Nuclear Instruments and Methods in Physics Research A*, vol. 645, 2011, p. 12.

[122] Gubbens, A., *et al.*: The GIF Quantum, a next generation post-column imaging energy filter. *Ultramicroscopy*, vol. 110, 2010, p. 962.

[123] Marfunin, A. S.: *Spectroscopy, luminescence and radiation centers in minerals.* Springer-Verlag Berlin Heidelberg, 1979. ISBN 978-3-642-67114-2.

[124] Thomson, J. J.: Cathode rays. *Philosophical Magazine Series 5*, vol. 44, 1897, p. 293.

[125] Yacobi, B. G., Holt, D. B.: *Cathodoluminescence microscopy of inorganic solids.* Springer Science+Business Media New York, 1990. ISBN 978-1-4757-9595-0.

[126] Guscik, A.: *Cathodoluminescence and its application in the planetary sciences.* Springer-Verlag Berlin Heidelberg, 2009. ISBN 978-3-540-87528-4.

[127] Boggs, S., Krinsley, D.: *Application of cathodoluminescence imaging to the study of sedimentary rocks.* Cambridge University Press, 2006. ISBN 978-0-521-85878-6.

[128] Yamamoto, N., Toda, A., Araya, K.: Imaging of transition radiation from thin films on a silicon substrate using a light detection system combined with TEM. *Journal of Electron Microscopy*, vol. 45, 1996, p. 64.

[129] Narváez, A. C., *et al.*: Cathodoluminescence microscopy of nanostructures on glass substrates. *Optics Express*, vol. 21, 2013, p. 29968.

[130] Glenn, D. R., *et al.*: Correlative light and electron microscopy using cathodoluminescence from nanoparticles with distinguishable colours. *Scientific Reports*, vol. 2, 2012, p. 865.

[131] Yamamoto, N., *et al.*: Light emission from surfaces, thin films and particles induced by high-energy electron beam. *Surface and Interface Analysis*, vol. 31, 2001, p. 79.

[132] Stöger-Pollach, M., *et al.*: Transition radiation in EELS and cathodoluminescence, *Ultramicroscopy*, vol. 173, 2017, p. 31.

[133] Yamamoto, N., García de Abajo, F. J., Myroshnychenko, V.: Interference of surface plasmons and Smith-Purcell emission probed by angle-resolved cathodoluminescence spectroscopy. *Physical Review B*, vol. 91, 2015, p. 125144.

[134] Vesseur, E. J. R. *et al.*: Direct observation of plasmonic modes in Au nanowires using high-resolution cathodoluminescence spectroscopy. *Nano Letters*, vol. 7, 2007, p. 2843.

[135] Chaturvedi, P., *et al.*: Imaging of plasmonic modes of silver nanoparticles using high-resolution cathodoluminescence spectroscopy. *ACS Nano*, vol. 3, 2009, p. 2965.

[136] Ter-Mikaelian, M.L.: *High-Energy Electromagnetic Processes in Condensed Media.* Wiley-Interscience, New York, 1972.

[137] James, C. W., *et al.*: General description of electromagnetic radiation processes based on instantaneous charge acceleration in 'endpoints'. *Physical Review A*, vol. 84, 2011, p. 056602.

[138] Khlyap, H., *et al.*: *Effect of native oxide on the electric field-induced characteristics of device-quality silicon at room temperature.* In: Basu, S.: *Crystalline silicon – properties and uses.* IntechOpen, 2011. ISBN: 978-953-307-587-7.

[139] Gatan, Inc.: *Cathodoluminescence Microscopy* <http://www.gatan.com/cathodoluminescence-insulators-metals-and-plasmonics>

[140] Ligmajer, F.: *Advanced plsmonic materials for metasurfaces and photochemistry.* Brno: Vysoké učení technické v Brně, Středoevropský technologický institut, 2018. 185 s. Dizertační práce, vedoucí práce prof. RNDr. Tomáš Šikola, CSc.

[141] Reather, H. *Surface Plasmons on Smooth and Rough Surfaces and on Gratings.* Springer-Verlag Berlin Heidelberg, 1988. ISBN 978-3-540-17363-3.

[142] Fang, Y., Tian, X. Resonant surface plasmons of a metal nanosphere can be considered in the way of propagating surface plasmons. *arXiv:1412.2664*, 2014.

[143] Ogale, S. B., Bhoraskar, V. N., Panat, P. V. Surface plasmon dispersion relation for spherical metal particles. *Pramana - Journal of Physics*, vol. 11, 1978, p. 135.

[144] Bohren, C. F., Huffman, D. R.: *Absorbtion and Scattering of Light by Small Particles.* Wiley-VCH, 1998, 544 p. ISBN 0-471-29340-7.

[145] Boudarham, G., Kociak, M.: Modal decompositions of the local electromagnetic density of states and spatially resolved electron energy loss probability in terms of geometric modes. *Physical Review B*, vol. 85, 2012, p. 245447.

[146] Myroshnychenko, V., *et al.*: Modelling the optical response of gold nanoparticles. *Chemical Society Reviews*, vol. 37, 2008, p. 1792.

[147] Cao, Y., *et al.*: Electron energy-loss spectroscopy calculation in finite-difference time-domain package. *ACS Photonics*, vol. 2, 2015, p. 369.

[148] Geuquet, N., Henrard, L.: EELS and optical response of a noblemetal nanoparticle in the frame of a discrete dipole approximation. *Ultramicroscopy*, vol. 110, 2010, p. 1075.

[149] COMSOL, Inc.: *COMSOL Multiphysics Modeling Software.* <https://www.comsol.com/>

[150] Hohenester, U., Trügler, A.: *MNPBEM toolbox.* <http://physik.uni-graz.at/mnpbem/>

[151] Hohenester, U.: Simulating EELS with the MNPBEM toolbox. *Computer Physics Communications*, vol. 185, 2014, p. 1177.

[152] Waxenegger, J., Trügler, A., Hohenester, U.: Plasmonics simulations with the MNPBEM toolbox: Consideration of substrates and layer structures. *Computer Physics Communications*, vol. 193, 2015, p. 138

[153] Lumerical Computational Solutions, Inc.: *High-Performance Nanophotonic Simulation Software - Lumerical* <https://www.lumerical.com/>

[154] Garcia de Abajo, F. J., Howie, A.: Retarded field calculation of electron energy loss in inhomogeneous dielectrics. *Physical Review B*, vol. 65, 2002, p. 115418.

[155] Yee, K. S.: Numerical solution of initial boundary value problems involving Maxwell's equations in isotropic media. *IEEE Transactions on Antennas and Propagation*, vol. 14, 1966, p. 302.

[156] Lumerical Computational Solutions, Inc.: *Electron Beam Spectroscopy, Lumerical Knowledge Base.* <https://kb.lumerical.com/en/nanophotonic_applications_electron_beam_spectroscopy.html>

[157] Kociak, M., *et al.*: Seeing and measuring in colours: Electron microscopy and spectroscopies applied to nano-optics. *Comptes Rendus Physique*, vol. 15, 2014, p. 158.

[158] Diaz-Egea, C., *et al.*: High spatial resolution mapping of surface plasmon resonance modes in single and aggregated gold nanoparticles assembled on DNA strands. *Nanoscale Research Letters*, vol. 8, 2013, p. 337.

[159] Raza, S., *et al.*: Blueshift of the surface plasmon resonance in silver nanoparticles studied with EELS. *Nanophotonics*, vol. 2, 2013, p. 131.

[160] Raza, S., *et al.*: Multipole plasmons and their disappearance in few-nanometre silver nanoparticles. *Nature Communications*, vol. 6, 2015, p. 8788.

[161] Scholl, J. A., *et al.*: Observation of quantum tunneling between two plasmonic nanoparticles. *Nano Letters*, vol. 13, 2013, p. 564.

[162] Scholl, J. A., *et al.*: Evolution of plasmonic metamolecule modes in the quantum tunneling regime. *ACS Nano*, vol. 10, 2016, p. 1346.

[163] Yamamoto, N., Ohtani, S., García de Abajo, F. J.: Gap and Mie plasmons in individual silver nanospheres near a silver surface. *Nano Letters*, vol. 11, 2011, p. 91.

[164] Thollar, Z., *et al.*: Three-dimensional multipole rotation in spherical silver nanoparticles observed by cathodoluminescence. *ACS Photonics*, vol. 5, 2018, p. 2555.

[165] Campos, A., *et al.*: Plasmonic quantum size effects in silver nanoparticles are dominated by interfaces and local environments. *Nature Physics*, 2018.

[166] Nicoletti, O., *et al.*: Surface plasmon modes of a single silver nanorod: an electron energy loss study. *Optics Express*, vol. 19, 2011, p. 15371.

[167] Zhou, X., *et al.*: Effect of multipole excitations in electron energy-loss spectroscopy of surface plasmon modes in silver nanowires. *Journal of Applied Physics*, vol. 116, 2014, p. 223101.

[168] Gómez-Medina, R., *et al.*: Mapping plasmons in nanoantennas via cathodoluminescence. *New Journal of Physics*, vol. 10, 2008, p. 105009.

[169] Bryant, G. W., García de Abajo, F. J., Aizpurua J.: Mapping the plasmon resonances of metallic nanoantennas. *Nano Letters*, vol. 8, 2008, p. 631.

[170] Bosman, M., *et al.*: Surface plasmon damping quantified with an electron nanoprobe. *Scientific Reports*, vol. 3, 2013, p. 1312.

[171] Gómez, D. E., *et al.*: The dark side of plasmonics. *Nano Letters*, vol. 13, 2013, p. 3722.

[172] Das, P., *et al.*: Nanocross: a highly tunable plasmonic system. *Journal of Physical Chemistry C*, vol. 121, 2017, p. 16521.

[173] Martin, J., *et al.*: High-resolution imaging and spectroscopy of multipolar plasmonic resonances in aluminum nanoantennas. *Nano Letters*, vol. 14, 2014, p. 5517.

[174] Kumar, A., Fung, K. H., Fang, N. X.: Mapping of surface plasmon polaritons on nanostructured thin film disks using cathodoluminescence imaging. *SPIE Proceedings*, vol. 7946, 2011.

[175] Schmidt, F. P., *et al.*: Dark plasmonic breathing modes in silver nanodisks. *Nano Letters*, vol. 12, 2012, p. 5780.

[176] Matsukata, T., *et al.*: Selected mode mixing and interference visualized within a single optical nanoantenna. *ACS Photonics*, vol. 5, 2018, p. 4986.

[177] Schmidt, F. P., *et al.*: How dark are radial breathing modes in plasmonic nanodisks? *ACS Photonics*, vol. 5, 2018, p. 861.

[178] Coenen, T., Polman, A.: Optical properties of single plasmonic holes probed with local electron beam excitation. *ACS Nano*, vol. 8, 2014, p. 7350.

[179] Schmidt, F. P., *et al.*: Morphing a plasmonic nanodisk into a nanotriangle. *Nano Letters*, vol. 14, 2014, p. 4810.

[180] Das, P., Chini, T. K., Pond, J.: Probing higher order surface plasmon modes on individual truncated tetrahedral gold nanoparticle using cathodoluminescence imaging and spectroscopy combined with FDTD simulations. *Journal of Physical Chemistry C*, vol. 116, 2012, p. 15610.

[181] Kawasaki, N., *et al.*: Extinction and scattering properties of high-order surface plasmon modes in silver nanoparticles probed by combined spatially resolved electron energy loss spectroscopy and cathodoluminescence. *ACS Photonics*, vol. 3, 2016, p. 1654.

[182] Campos, A., *et al.*: Plasmonic breathing and edge modes in aluminum nanotriangles. *ACS Photonics*, vol. 4, 2017, p. 1257.

[183] Koh, A. L., *et al.*: High-resolution mapping of electron-beam-excited plasmon modes in lithographically-defined gold nanostructures. *Nano Letters*, vol. 11, 2011, p. 1323.

[184] Myroshnychenko, V., *et al.*: Plasmon spectroscopy and imaging of individual gold nanodecahedra: A combined optical microscopy, cathodoluminescence, and electron energy-loss spectroscopy study. *Nano Letters*, vol. 12, 2012, p. 4172.

[185] Boudarham, G., *et al.* Spectral imaging of individual split-ring resonators. *Physical Review Letters*, vol. 105, 2010, p. 255501.

[186] Flauraud, V., *et al.*: Mode coupling in plasmonic heterodimers probed with electron energy loss spectroscopy. *ACS Nano*, vol. 11, 2017, p. 3485.

[187] Atre, A. C., *et al.*: Nanoscale optical tomography with cathodoluminescence spectroscopy. *Nature Nanotechnology*, vol. 10, 2015, p. 429.

[188] Hörl, A., Trügler, A., Hohenester, U.: Tomography of particle plasmon fields from electron energy loss spectroscopy. *Physical Review Letters*, vol. 111, 2013, p. 076801.

[189] Hörl, A., *et al.*: Tomographic imaging of the photonic environment of plasmonic nanoparticles. *Nature Communications*, vol. 8, 2017, p. 37.

[190] Haberfehlner, G., *et al.*: Correlated 3D nanoscale mapping and simulation of coupled plasmonic nanoparticles. *Nano Letters*, vol. 15, 2015, p. 7726.

[191] Nicoletti, O., *et al.*: Three-dimensional imaging of localized surface plasmon resonances of metal nanoparticles. *Nature*, vol. 502, 2013, p. 80.

[192] Edwards, P. R., *et al.*: Mapping localized surface plasmons within silver nanocubes using cathodoluminescence hyperspectral imaging. *Journal of Physical Chemistry C*, vol. 115, 2011, p. 14031.

[193] Lourenco-Martins, H., *et al.*: Probing plasmon-NV^0 coupling at the nanometer scale with photons and fast electrons. *ACS Photonics*, vol. 5, 2018, p. 324.

[194] Guzzianti, G., *et al.*: Probing the symmetry of the potential of localized surface plasmon resonances with phase-shaped electron beams. *Nature Communications*, vol. 8, 2017, p. 14999.

[195] Huang, J. S., *et al.*: Atomically flat single-crystalline gold nanostructures for plasmonic nanocircuitry. *Nature Communication*, vol. 1, 2010, p. 150.

[196] Wang, X., *et al.*: Vapor-phase preparation of single-crystalline thin gold microplates using $HAuCl_4$ as the precursor for plasmonic applications. *RSC Advances*, vol. 6, 2016, p. 74937.

[197] Xu, X., Gölzhäuser, A.: *Helium Ion Microscopy.* Springer, 2016. ISBN 978-3-319-41988-6.

[198] Aoki, T., Garvie, L. A. J., Rez, P.: Observation of color center peaks in calcium fluoride. *Ultramicroscopy*, vol. 153, 2015, p. 40.

[199] Williams, R. T., *et al.*: Time-resolved spectroscopy of self-trapped excitons in fluorite crystals. *Physical Review B*, vol. 14, 1976, p. 725.

[200] Šimšíková, M., *et al.*: Green approach for preparation of reduced graphene oxide decorated with gold nanoparticles and its optical and catalytic properties. *Materials Chemistry and Physics*, vol. 177, 2016, p. 339.

[201] Šimšíková, M., *et al.*: Decolorization of organic dyes by gold nanoflowers prepared on reduced graphene oxide by tea polyphenols. *Catalysis Science & Technology*, vol. 6, 2016, p. 3008.

[202] CEITEC Nano research infrastructure: *Mapping of localised surface plasmons in gold disc nanoparticle (diameter 380 nm) by Monochromated-STEM Electron Energy Loss Spectroscopy.* <https://www.facebook.com/ceitecnano/photos/a.526524060819003/716518975152843>

[203] McPeak, K. M., *et al.*: Plasmonic films can easily be better: Rules and recipes. *ACS Photonics*, vol. 2, 2015, p. 326.

[204] Palik, E. D., Ghosh, G.: *Handbook of optical constants of solids*. Academic Press New York, 1997. ISBN 978-0-1254-4415-6.

[205] Rakić, A. D.: Algorithm for the determination of intrinsic optical constants of metal films: application to aluminum. *Applied Optics*, vol. 34, 1995, p. 4755.

[206] Johnson, P. B., Christy, R. W.: Optical constants of the noble metals. *Physical Review B*, vol. 6, 1972, p. 4370.

[207] Werner, W. S. M., Glantschnig, K., Ambrosch-Draxl, C.: Optical constants and inelastic electron-scattering data for 17 elemental metals. *Journal of Physical and Chemical Reference Data*, vol. 38, 2009, p. 1013.

[208] Olmon, R. L., *et al.*: Optical dielectric function of gold. *Physical Review B*, vol. 86, 2012, p. 235147.

[209] McIntosh, K. R., *et al.*: Quantifying the optical losses in back-contact solar cells. *40th IEEE Photovoltaic Specialists Conference*, Denver, 2014, p. 115.

[210] Novotny, L., van Hulst, N.: Antennas for light. *Nature Photonics*, vol. 5, 2011, p. 83.

[211] Grosjean, T., *et al.*: Diabolo nanoantenna for enhancing and confining the magnetic optical field. *Nano Letters*, vol. 11, 2011, p. 1009.

[212] Duan, H., *et al.*: Metrology for electron-beam lithography and resist contrast at the sub-10 nm scale. *Journal of Vacuum Science & Technology B*, vol. 28, 2010, p. C6H11.

[213] Postek, M. T.: An approach to the reduction of hydrocarbon contamination in the scanning electron microscope. *Scanning*, vol. 18, 1996, p. 269.

[214] Egerton, R. F., Li, P., Malac, M.: Radiation damage in the TEM and SEM. *Micron*, vol. 35, 2004, p. 399.

[215] Walczyk, W., Schön, P. M., Schönherr, H.: The effect of PeakForce tapping mode AFM imaging on the apparent shape of surface nanobubbles. *Journal of Physics: Condensed Matter*, vol. 25, 2013, p. 1.

[216] Mitchell, D. R. G.: Determination of mean free path for energy loss and surface oxide film thickness using convergent beam electron diffraction and thickness mapping: a case study using Si and P91 steel. *Journal of Microscopy*, vol. 224, 2006, p. 187.

[217] Michael, J. R.: Focused ion beam induced microstructural alterations: texture development, grain growth, and intermetallic formation. *Microscopy and Microanalysis*, vol. 17, 2011, p. 386.

[218] Pyykkö, P., Atsumi, M.: Molecular single-bond covalent radii for elements 1–118. *Chemistry: A European Journal*, vol. 15, 2009, p. 186.

[219] Hentschel, M., *et al.*: Babinet to the half: coupling of solid and inverse plasmonic structures. *Nano Letters*, vol. 13, 2013, p. 4428.

[220] Bitzer, A., *et al.*: Terahertz near-field microscopy of complementary planar metamaterials: Babinet's principle. *Optics Express*, vol. 19, 2001, p. 2537.

[221] Yang, H. U., *et al.*: Accessing the optical magnetic near-field through Babinet's principle. *ACS Photonics*, vol. 1, 2014, p. 894.

[222] Daňhel, A., *et al.*: Electrodeposition of silver amalgam particles on ITO – Towards novel electrode material. *Journal of Electroanalytical Chemistry*, vol. 821, 2018, p. 53.

List of abbreviations

ADF	annular dark field
AES	Auger electron microscope/microscopy
AFM	atomic force microscope/microscopy
BEM	boundary element method
CCD	charge-coupled device
CL	cathodoluminescence
CRT	cathode ray tube
DDA	discrete dipole approximation
EBL	electron beam lithography
EEL	electron energy loss
EELS	electron energy loss spectroscopy
EFTEM	energy filtered transmission electron microscopy
EDS	energy dispersive X-ray spectroscopy
FDTD	finite-difference time-domain
FEM	finite element method
FIB	focused ion beam
FWHM	full-width at half-maximum
GIF	Gatan image filter
HAADF	high-angle annular dark field
IMFP	inelastic mean free path
ITO	indium-tin-oxide
KKA	Kramers-Krönig analysis
LD	longitudinal dipole
LDA	longitudinal antibonding dipole
LDB	longitudinal bonding dipole
LSP	localized surface plasmons
PMT	photomultiplier tube
Q	quadrupole
SEM	scanning electron microscope/microscopy
SPP	surface plasmon polaritons
STEM	scanning transmission electron microscope/microscopy
TD	transverse dipole
TEM	transmission electron microscope/microscopy
ZLP	zero-loss peak

A Additional equations

A.1 Low-loss EELS

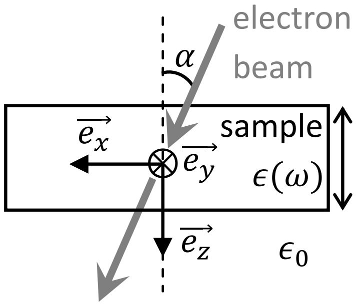

Figure A.1: Schematic sketch of the sample geometry. The electron beam goes through the sample with the thickness t and the dielectric function ϵ located in vacuum inclined at the angle α to the z axis perpendicular to the sample.

The differential energy loss probability assuming the electron beam with the momentum p_0 inclined at the angle α to the z axis perpendicular to the sample with the thickness t and the dielectric function ϵ located in vacuum (see Figure A.1) is expressed by Equation (A.1) [6, 7, 105].

$$
\begin{aligned}
\frac{\partial^3 P(\vec{k_\perp},\omega)}{\partial E \partial \Omega} = {} & \frac{p_0^2}{\hbar^2} \frac{e^2}{\pi^2 \hbar^2 v^2 \cos\alpha} \Im \left\{ \frac{1-\epsilon\left(\frac{v}{c}\right)^2}{\epsilon \phi^2} t - \right. \\
& -2 \frac{(\epsilon-\epsilon_0)^2}{\phi_0^4 \phi^2} \left\{ \left(\frac{\sin^2 \frac{\kappa t}{2v_z}}{L^+} + \frac{\cos^2 \frac{\kappa t}{2v_z}}{L^-} \right) \frac{B^2}{\epsilon \epsilon_0} - \right. \\
& - \left(\frac{\cos^2 \frac{\kappa t}{2v_z} \tanh \frac{\lambda t}{2}}{L^+} + \frac{\sin^2 \frac{\kappa t}{2v_z} \coth \frac{\lambda t}{2}}{L^-} \right) A^2 \lambda \lambda_0 + \\
& + \left(\frac{1}{L^+} - \frac{1}{L^-} \right) \frac{\lambda_0}{\epsilon_0} AB \sin \frac{\kappa t}{v_z} + \\
& + \left(\frac{\omega}{v}\right)^4 \left(\frac{v}{c}\right)^6 \sin^2\alpha \sin^2\phi \left[\left(\frac{\kappa}{v_z}\right)^2 \left(\frac{\sin^2 \frac{\kappa t}{2v_z}}{M^+} + \frac{\cos^2 \frac{\kappa t}{2v_z}}{M^-} \right) - \right. \\
& - \left(\frac{\cos^2 \frac{\kappa t}{2v_z} \tanh \frac{\lambda t}{2}}{M^+} + \frac{\sin^2 \frac{\kappa t}{2v_z} \coth \frac{\lambda t}{2}}{M^-} \right) \lambda \lambda_0 - \\
& \left. \left. \left. - \left(\frac{1}{M^+} - \frac{1}{M^-} \right) \lambda_0 \frac{\kappa}{v_z} \sin \frac{\kappa t}{v_z} \right] \right\} \right\},
\end{aligned}
\tag{A.1}
$$

where the following abbreviations are used:

$$
\begin{aligned}
\vec{k_\perp} &= (k_x, k_y, 0), \\
k_\perp &= \sqrt{k_x^2 + k_y^2}, \\
\kappa &= \omega + k_x v_x, \\
\lambda &= \sqrt{k_\perp^2 - \frac{\epsilon\omega^2}{c^2}}, \\
\lambda_0 &= \sqrt{k_\perp^2 - \frac{\epsilon_0\omega^2}{c^2}}, \\
L^+ &= \lambda_0\epsilon + \lambda\epsilon_0 \tanh\frac{\lambda t}{2}, \\
L^- &= \lambda_0\epsilon + \lambda\epsilon_0 \coth\frac{\lambda t}{2}, \\
M^+ &= \lambda_0 + \lambda \tanh\frac{\lambda t}{2}, \\
M^- &= \lambda_0 + \lambda \coth\frac{\lambda t}{2}, \\
\phi^2 &= k_\perp^2 + \frac{\kappa^2}{v_z^2} - \epsilon\frac{\omega^2}{c^2}, \\
\phi_0^2 &= k_\perp^2 + \frac{\kappa^2}{v_z^2} - \epsilon_0\frac{\omega^2}{c^2}, \\
\phi_{01}^2 &= k_\perp^2 + \frac{\kappa^2}{v_z^2} - (\epsilon + \epsilon_0)\frac{\omega^2}{c^2}, \\
A &= \left(k_\perp - \frac{\kappa}{v_z}\tanh\alpha\cos\phi\right)\frac{\omega}{v}\left(\frac{v}{c}\right)^2\cos\alpha, \\
B &= k_\perp\phi_{01}^2 + \epsilon\epsilon_0\left(\frac{\omega}{v}\right)^3\left(\frac{v}{c}\right)^4\sin\alpha\cos\phi.
\end{aligned}
\tag{A.2}
$$

The first row in Equation (A.1) corresponds to volume losses and all the other rows correspond to surface losses such as surface plasmon and light guiding modes. In the case of normal incidence $\alpha \approx 0$, the last three rows in Equation (A.1) equal to zero.

A.2 Coherent cathodoluminescence

The photon flux of transition radiation in forward direction is [97, 131]

$$\frac{\partial^3 N}{\partial\lambda\partial\Omega} = \frac{\alpha\left(\frac{v}{c}\right)^2}{4\pi\lambda} n_2 \sin^2\theta_2 \left|A(\epsilon_1, \epsilon_2, \theta_2, \frac{v}{c})\right|^2, \tag{A.3}$$

where

$$A(\epsilon_1, \epsilon_2, \theta_2, \frac{v}{c}) = \frac{(\epsilon_1 - \epsilon_2)(1 - \left(\frac{v}{c}\right)^2\epsilon_2 - \frac{v}{c}\sqrt{\epsilon_1 - \epsilon_2\sin^2\theta_2})}{(1 - \left(\frac{v}{c}\right)^2\epsilon_2\cos^2\theta_2)(1 - \frac{v}{c}\sqrt{\epsilon_1 - \epsilon_2\sin^2\theta_2})(\epsilon_1\cos\theta_2 + \sqrt{\epsilon_1\epsilon_2 - \epsilon_2^2\sin^2\theta_2})} \tag{A.4}$$

$\alpha = 1/137$ is the fine structure constant, ϵ_1 and ϵ_2 are the dielectric functions of media 1 and 2, n_2 is the refractive index of medium 2 and θ_2 is the emission angle measured from the boundary normal in the direction $\vec{v}$.

The transition radiation at two boundaries, where the medium 1 and 3 is the vacuum, which corresponds to a standard TEM sample, is described by the formula for forward emission [97, 131]

$$\frac{\partial^3 N}{\partial\lambda\partial\Omega} = \frac{\alpha\left(\frac{v}{c}\right)^2}{4\pi^2\lambda}\sin^2\theta_3\left|B_1 + B_2\exp(2i\delta) + B_3\exp\left[i(\delta-\eta)\right]\right|^2, \tag{A.5}$$

with

$$\begin{aligned}
B_1 &= A\left(\epsilon_2, 1, \theta_3, \frac{v}{c}\right), \\
B_2 &= -\frac{1}{n_2} r_{21} f_{32} D(d) A\left(1, \epsilon_2, \theta_2, -\frac{v}{c}\right), \\
B_3 &= \frac{1}{n_2} f_{32} D(d) A\left(1, \epsilon_2, \theta_2, \frac{v}{c}\right), \\
D(d) &= \left[1 - r_{21}^2\exp(2i\delta)\right]^{-1}, \\
\delta &= \frac{2\pi d n_2\cos\theta_2}{\lambda}, \\
\eta &= \frac{2\pi d}{\lambda\frac{v}{c}}, \\
f_{ik} &= \frac{2n_i\cos\theta_i}{n_k\cos\theta_i + n_i\cos\theta_k}, \\
r_{ik} &= \frac{n_k\cos\theta_i - n_i\cos\theta_k}{n_k\cos\theta_i + n_i\cos\theta_k},
\end{aligned} \tag{A.6}$$

where the angles are connected by the Snell law $\sin\theta_1 = n_2\sin\theta_2 = \sin\theta_3$, d is the thickness of medium 2 and function $A(\epsilon_1, \epsilon_2, \theta_2, v/c)$ is defined in Equation (A.4).

Čerenkov radiation is included in term B_2 [97]. To obtain the formula for backward emission, Equation (A.5) must be modified by replacing the indices 1, 2, 3 by 3, 2, 1 and changing v/c to $-v/c$. The angles θ are then measured from the direction $-\vec{v}$. For normal incidence, the light is p-polarized.

B List of author's scientific achievements

B.1 Author's scientific identifiers

Researcher ID:	R-2546-2017
ORCID ID:	0000-0001-6503-8294
SCOPUS ID:	57200608539

B.2 Publications in impact journals

1. M. Horák, M. Stöger-Pollach: The Čerenkov limit of Si, GaAs and GaP in electron energy loss spectrometry. *Ultramicroscopy*, vol. 157, 2015, p. 73.
   doi: 10.1016/j.ultramic.2015.06.005

   ISSN 0304-3991. Impact factor (2015): 2.874.

   My contribution: all experimental work with GaAs and GaP including the analysis and interpretation of the results, partially writing the manuscript

2. M. Horák, J. Zlámal: Accurate interpolation of 3D fields close to the optical axis. *Microscopy and Microanalysis*, vol. 21, no. S4, 2015, p. 242.
   doi: 10.1017/S1431927615013446

   ISSN 1435-8115. Impact factor (2015): 1.37.

   My contribution: development of the interpolation method, numerical calculations, analysis and interpretation of the results, writing the manuscript

3. M. Horák, V. Badin, J. Zlámal: Accurate interpolation of 3D fields in charged particle optics. *Ultramicroscopy*, vol. 189, 2018, p. 95.
   doi: 10.1016/j.ultramic.2018.03.023

   ISSN 0304-3991. Impact factor (2018): 2.644.

   My contribution: development of the interpolation method, numerical calculations of magnetic lenses, analysis and interpretation of the results, writing the manuscript, coordination of the team

4. M. Horák, K. Bukvišová, V. Švarc, J. Jaskowiec, V. Křápek, T. Šikola: Comparative study of plasmonic antennas fabricated by electron beam and focused ion beam lithography. *Scientific Reports*, vol. 8, 2018, p. 9640.
   doi: 10.1038/s41598-018-28037-1

   ISSN 2045-2322. Impact factor (2018): 4.011.

   My contribution: design of the experiment, FIB fabrication, all characterization in TEM including EELS and EDS, analysis and interpretation of the results, writing the manuscript, coordination of the team

5. L. Zdražil, R. Zahradníček, R. Mohan, P. Sedláček, L. Nejdl, V. Schmiedová, J. Pospíšil, M. Horák, M. Weiter, O. Zmeškal, J. Hubálek: Preparation of graphene quantum dots through liquid phase exfoliation method. *Journal of Luminescence*, vol. 204, 2018, p. 203.
   doi: 10.1016/j.jlumin.2018.08.017

   ISSN: 0022-2313. Impact factor (2018): 2.961.

   My contribution: TEM and EELS measurement including interpretation of the results

6. M. Stöger-Pollach, K. Bukvišová, S. Schwarz, M. Kvapil, T. Šamořil, M. Horák: Fundamentals of cathodoluminescence in a STEM: The impact of sample geometry and electron beam energy on light emission of semiconductors. *Ultramicroscopy*, vol. 200, 2019, p. 111.
   doi: 10.1016/j.ultramic.2019.03.001

   ISSN 0304-3991. Impact factor (2018): 2.644.

   My contribution: part of sample preparation by FIB, part of CL measurements, partially coordination of the team

7. M. Horák, V. Křápek, M. Hrtoň, A. Konečná, F. Ligmajer, M. Stöger-Pollach, T. Šamořil, A. Paták, Z. Édes, O. Metelka, J. Babocký, T. Šikola: Limits of Babinet's principle for solid and hollow plasmonic antennas. *Scientific Reports*, vol. 9, 2019, p. 4004.
   doi: 10.1038/s41598-019-40500-1

   ISSN 2045-2322. Impact factor (2018): 4.011.

   My contribution: FIB fabrication, all TEM measurements including EELS and CL, analysis and interpretation of the results, partially writing the manuscript

8. F. Ligmajer, M. Horák, T. Šikola, M. Fojta, A. Daňhel: Silver amalgam nanoparticles: a novel plasmonic platform for spectro-electrochemistry. *Journal of Physical Chemistry C*, vol. 123, 2019, p. 16957.
   doi: 10.1021/acs.jpcc.9b04124.

   ISSN: 1932-7455. Impact factor (2018): 4.484.

My contribution: all TEM measurements including EELS and EDS, analysis and interpretation of the results

B.3 Manuscripts in publication process (preprints)

1. M. Hrtoň, A. Konečná, M. Horák, T. Šikola, V. Křápek: Plasmonic antennas with electric, magnetic, and electromagnetic hot spots based on Babinet's principle.
   Arxiv preprint, arxiv:1904.01397.

   My contribution: partially analysis and interpretation of the results

2. V. Křápek, A. Konečná, M. Horák, F. Ligmajer, M. Stöger-Pollach, M. Hrtoň, J. Babocký, T. Šikola: Independent engineering of individual plasmon modes in plasmonic dimers with conductive and capacitive coupling.
   Arxiv preprint, arxiv:1905.09210.

   My contribution: FIB fabrication of the antennas, all TEM measurements including EELS, analysis and interpretation of the results

B.4 Contributions to conference proceedings indexed in WoS or Scopus

1. I. Ferreira, M. Ayre, M. Bavdaz, M. Guainazzi, A. Stefanescu, M. Komárek, T. Valenta, R. Hynek, M. Závodník, P. Sobotka, T. Pejchal, V. Badin, R. Kalousek, J. Bačovský, M. Horák, L. Flajšman, O. Wojewoda, J. Zlámal: Design of the charged particle diverter for the ATHENA mission. *Proceedings Volume 10699, Space Telescopes and Instrumentation 2018: Ultraviolet to Gamma Ray*, 2018, p. 106994A.
   doi: 10.1117/12.2312226

   My contribution: part of magnetic fields simulation including analysis and interpretation of the results

2. T. Řiháček, M. Horák, T. Schachinger, M. Matějka, F. Mika, I. Mullerova: Creation of electron vortex beams using the holographic reconstruction method in a scanning electron microscope. *Recent Trends in Charged Particle Optics and Surface Physics Instrumentation*, 2018, p. 66. ISBN 978-80-87441-23-7.
   Available online: http://trends.isibrno.cz/

   My contribution: fabrication of holographic masks by FIB

B.5 Publications in peer-reviewed journals

1. M. Horák, V. Křápek, T. Šikola: Plazmonové rezonance ve zlatých nanočásticích zkoumané s využitím elektronové mikroskopie. *Jemná mechanika a optika*, vol. 62, no. 11–12, 2017, p. 303. ISSN 0447-6441.

My contribution: sample preparation, all measurements including EELS and CL, analysis and interpretation of the results, partially writing the manuscript

B.6 Active conference and meeting contributions

1. IMC 18 – 18th International Microscopy Congress
   7th–12th September 2014, Prague, Czech Republic.
   - ○ M. Horák, M. Stöger-Pollach: *Experimental detection of the Čerenkov limit in Si, GaAs and GaP.* Poster presentation.
2. Výroční konference Československé mikroskopické společnosti Mikroskopie 2016
   3rd–4th May 2016, Lednice na Moravě, Czech Republic.
   - ○ M. Horák, V. Křápek, A. L. Koh, L. Břínek, M. Hrtoň, R. Kalousek, T. Šikola: *Mapping of plasmonic modes in gold nanoparticles by electron beam spectroscopy.* Poster presentation.
3. 1st CEITEC Nano User Meeting
   1st December 2016, Brno, Czech Republic.
   - ○ M. Horák, M. Stöger-Pollach, A. Paták, T. Šikola: *Electron beam spectroscopy in plasmonics.* Poster presentation.
4. 7th ASEM workshop of the Austrian Society of Electron Microscopy
   20th–21st April 2017, Vienna, Austria.
   - • M. Horák, V. Křápek, M. Hrtoň, M. Stöger-Pollach, T. Šamořil, F. Ligmajer, T. Šikola: *Babinet principle for plasmonic antennas: complementarity and differences.* Oral presentation.
5. Výroční konference Československé mikroskopické společnosti Mikroskopie 2017
   9th–10th May 2017, Bratislava, Slovakia.
   - • M. Horák, V. Křápek, O. Metelka, T. Šamořil, M. Stöger-Pollach, A. Paták, T. Šikola: *Electron beam spectroscopy of localized plasmon resonances in gold nanoparticles, gold disc antennas, and complementary apertures.* Oral presentation.
6. 16th IUVSTA International Summer School on Physics at Nanoscale
   12th–17th June 2017, Hotel Devět Skal, Milovy, Czech Republic.
   - ○ M. Horák, M. Stöger-Pollach, A. Paták, T. Šikola: *Plasmon resonances in gold nanoparticles.* Poster presentation.
7. MCM 2017 – 13th Multinational Congress on Microscopy
   24th–29th September 2017, Rovinj, Croatia.
   - ○ M. Horák, V. Křápek, M. Hrtoň, O. Metelka, T. Šamořil, M. Stöger-Pollach, A. Paták, T. Šikola: *Babinet principle for plasmonic antennas: complementarity and differences.* Poster presentation.

8. EBSN 2017 – 2nd International Workshop on Electron Beam Spectroscopy for Nanophotonics
   25th–27th October 2017, Hotel Calipolis, Sitges, Barcelona, Spain.
   - ○ M. Horák, V. Křápek, M. Hrtoň, O. Metelka, T. Šamořil, M. Stöger-Pollach, A. Paták, T. Šikola: *Babinet principle for plasmonic antennas: complementarity and differences.* Poster presentation.
9. 2nd CEITEC Nano User Meeting
   30th November 2017, Brno, Czech Republic.
   - ○ M. Horák, V. Křápek, M. Hrtoň, T. Šamořil, M. Stöger-Pollach, O. Metelka, A. Paták, T. Šikola: *Babinet principle for plasmonic antennas: complementarity and differences.* Poster presentation.
10. Meeting on Transmission Electron Microscopy (TEM) in Materials Sciences
    24th–25th April 2018, Brno, Czech Republic.
    - ● M. Horák: *Transmission electron microscopy in Plasmonics.* Oral presentation.
    - ○ M. Horák, V. Křápek, M. Hrtoň, T. Šamořil, M. Stöger-Pollach, O. Metelka, A. Paták, T. Šikola: *Babinet principle for plasmonic antennas: complementarity and differences.* Poster presentation.
11. 8th ASEM workshop of the Austrian Society of Electron Microscopy
    26th–27th April 2018, Vienna, Austria.
    - ● M. Horák, K. Bukvišová, V. Švarc, J. Jaskowiec, V. Křápek, M. Stöger-Pollach, T. Šikola: *Comparative study of plasmonic antennas: EBL vs. FIB fabrication.* Oral presentation.
12. Výroční konference Československé mikroskopické společnosti Mikroskopie 2018
    14th–16th May 2018, Lednice na Moravě, Czech Republic.
    - ● M. Horák, K. Bukvišová, V. Švarc, J. Jaskowiec, V. Křápek, M. Stöger-Pollach, T. Šikola: *Comparative study of plasmonic antennas: EBL vs. FIB fabrication.* Oral presentation.
13. ICN+T 2018 – International Conference on Nanoscience + Technology
    22nd–27th July 2018, Brno, Czech Republic.
    - ● M. Horák, M. Stöger-Pollach, A. Paták, M. Hrtoň, V. Křápek, T. Šikola: *Electron beam spectroscopy in plasmonics.* Oral presentation.
    - ○ M. Horák, K. Bukvišová, V. Švarc, J. Jaskowiec, V. Křápek, M. Stöger-Pollach, T. Šikola: *Comparative study of plasmonic antennas: EBL vs. FIB fabrication.* Poster presentation.
14. NFO 15 – 15th international conference on Near-field Optics and Nanophotonics
    26th–31st August 2018, Troyes, France.
    - ○ M. Horák, K. Bukvišová, V. Švarc, J. Jaskowiec, V. Křápek, M. Stöger-Pollach, T. Šikola: *Comparative study of plasmonic antennas: EBL vs. FIB fabrication.* Poster presentation.

15. IMC 19 – 19th International Microscopy Congress
    9th–14th September 2018, Sydney, Australia
    - ○ M. Horák, K. Bukvišová, V. Švarc, J. Jaskowiec, V. Křápek, M. Stöger-Pollach, T. Šikola: *Comparative study of plasmonic antennas: EBL vs. FIB fabrication.* Digital poster presentation.
    - ○ M. Horák, V. Křápek, M. Hrtoň, T. Šamořil, M. Stöger-Pollach, O. Metelka, A. Paták, T. Šikola: *Babinet principle for plasmonic antennas: complementarity and differences.* Digital poster presentation.
    - ○ M. Horák, J. Babocký, A. Křížová, L. Štrbková, L. Kejík, F. Ligmajer, M. Hrtoň, P. Dvořák, M. Týč, J. Čolláková, V. Křápek, R. Kalousek, R. Chmelík, T. Šikola: *Quantitative 3D phase imaging of plasmonic metasurfaces.* Digital poster presentation.
16. PETER Summer School 2018
    3rd–5th October 2018, Brno, Czech Republic.
    - ● M. Horák, K. Bukvišová, V. Švarc, J. Jaskowiec, V. Křápek, M. Stöger-Pollach, T. Šikola: *Comparative study of plasmonic antennas: EBL vs. FIB fabrication.* Oral presentation.
17. 3rd CEITEC Nano User Meeting
    29th November 2018, Brno, Czech Republic.
    - ○ M. Horák, K. Bukvišová, V. Švarc, J. Jaskowiec, V. Křápek, M. Stöger-Pollach, T. Šikola: *Comparative study of plasmonic antennas: EBL vs. FIB fabrication.* Poster presentation.
18. 9th ASEM workshop of the Austrian Society of Electron Microscopy
    25th–26th April 2019, Graz, Austria.
    - ○ M. Horák, V. Křápek, M. Hrtoň, A. Konečná, F. Ligmajer, M. Stöger-Pollach, T. Šikola: *Babinet's principle for solid and hollow plasmonic antennas.* Poster presentation.
19. Výroční konference Československé mikroskopické společnosti Mikroskopie 2019
    13th–15th May 2019, Lednice na Moravě, Czech Republic.
    - ● M. Horák, F. Ligmajer, T. Šikola, M. Fojta, A. Daňhel: *Plasmonic properties of silver amalgam nanoparticles studied by analytical transmission electron microscopy.* Oral presentation.
    - ○ M. Horák, V. Křápek, M. Hrtoň, A. Konečná, F. Ligmajer, M. Stöger-Pollach, T. Šikola: *Babinet's principle for solid and hollow plasmonic antennas.* Poster presentation.
20. Joint Retreat 2019
    25th–26th June 2019, Hotel Luna, Kouty, Czech Republic.
    - ○ M. Horák, V. Křápek, M. Hrtoň, A. Konečná, F. Ligmajer, M. Stöger-Pollach, T. Šikola: *Babinet's principle for solid and hollow plasmonic antennas.* Poster presentation.

21. META 2019, the 10th International Conference on Metamaterials, Photonic Crystals and Plasmonics
    23th–26th July 2019, Lisbon, Portugal.
    - M. Horák, V. Křápek, M. Hrtoň, A. Konečná, F. Ligmajer, M. Stöger-Pollach, T. Šikola: *Babinet's principle for solid and hollow plasmonic antennas.* Oral presentation.
    - P. Dvořák, M. Kvapil, P. Bouchal, Z. Édes, T. Šamořil, M. Horák, M. Hrtoň, F. Ligmajer, V. Křápek, T. Šikola: *Near-field phase imaging using phase-shifting digital holography.* Oral presentation.
22. MC 2019 – Microscopy Conference 2019
    1st–5th September 2019, Berlin, Germany.
    - ○ M. Horák, F. Ligmajer, T. Šikola, M. Fojta, A. Daňhel: *Plasmonic properties of silver amalgam nanoparticles studied by analytical transmission electron microscopy.* Poster presentation.
23. EBSN 2019 – 3rd International Workshop on Electron Beam Spectroscopy for Nanophotonics
    16th–18th September 2019, Orsay, France.
    - ○ M. Horák, V. Křápek, M. Hrtoň, A. Konečná, F. Ligmajer, M. Stöger-Pollach, T. Šikola: *Babinet's principle for solid and hollow plasmonic antennas.* Poster presentation.
    - ○ M. Horák, F. Ligmajer, T. Šikola, M. Fojta, A. Daňhel: *Plasmonic properties of silver amalgam nanoparticles studied by analytical transmission electron microscopy.* Poster presentation.